Volume 18
Number 13
2 April 2026
Pages 6633-7258

# Nanoscale

rsc.li/nanoscale

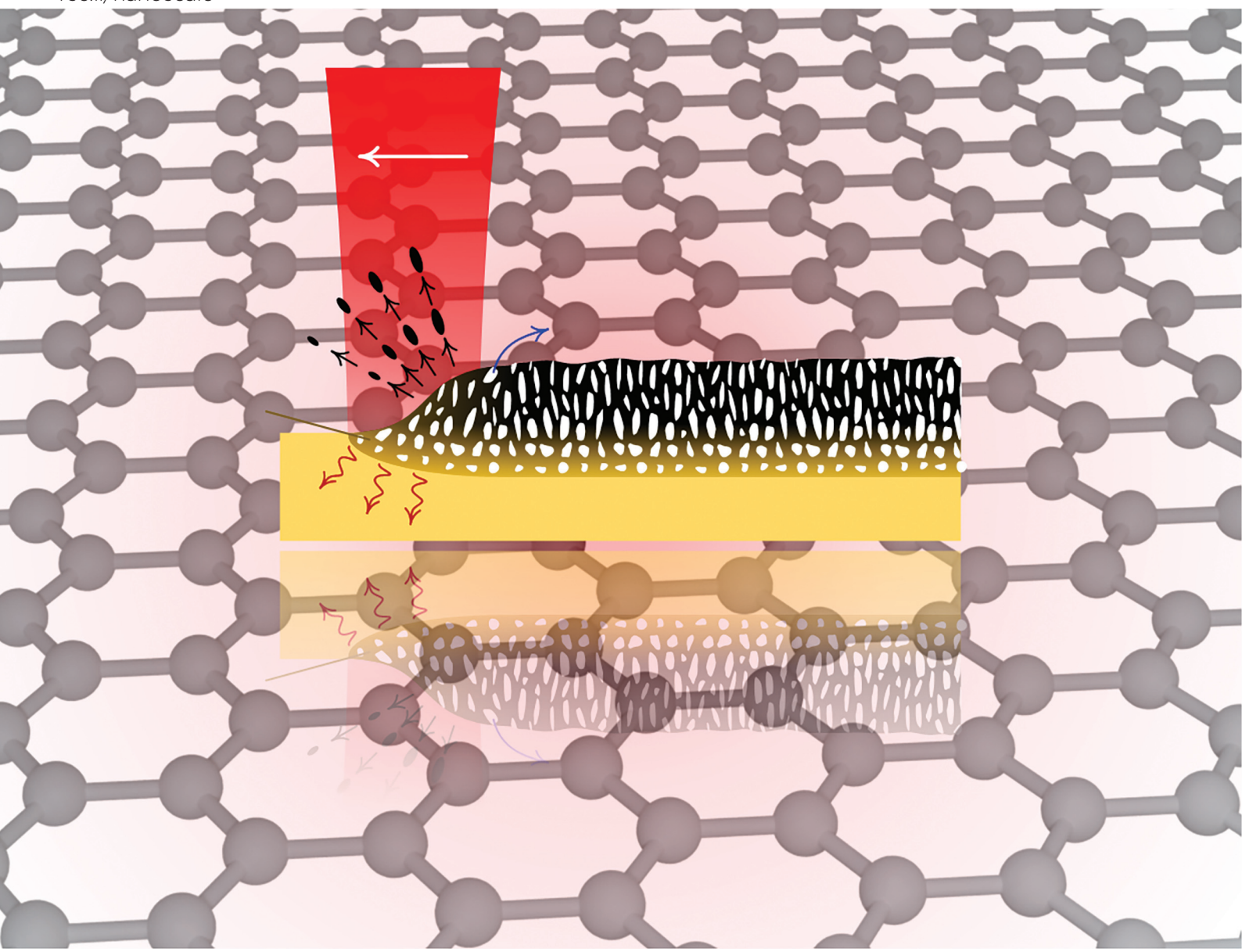

ISSN 2040-3372

ROYAL SOCIETY OF CHEMISTRY

**REVIEW ARTICLE**
Mostafa Bedewy *et al.*
Laser-induced graphene: from precursor chemistry to process control and throughput–resolution–performance trade-offs

NCNST

Nanoscale

REVIEW

View Article Online
View Journal | View Issue

Check for updates

Cite this: *Nanoscale*, 2026, **18**, 6647

# Laser-induced graphene: from precursor chemistry to process control and throughput–resolution–performance trade-offs

Zhenhao Wu,[a] Mirza Sahaluddin,[a] Diala Bani Mustafa,[a] Soumalya Ghosh[a] and Mostafa Bedewy *[a,b,c]

Laser-induced graphene (LIG) has matured from a laboratory curiosity into a versatile platform for fabricating porous, conductive carbon architectures directly on flexible polymers and bio-derived substrates. While prior reviews have catalogued devices and applications, a unifying framework connecting the precursor molecular structure, laser process parameters, resulting LIG morphology, and measured properties has been missing. This review fills that gap by advancing a process–structure–property perspective that explicitly links precursor chemical conversion, laser energy delivery, and post-processing to graphitization pathways, scalability, and device-level performance. We first organize the carbon precursors by function into single-layered (synthetic and natural/fossil derivatives) and multilayered (stacked and coated). We then distill how the molecular architecture, inherent heteroatoms, and composite design steer bond scission, outgassing, and $sp^2$-bond formation. We then map laser fluence and kinetics to morphology transitions (from isotropic porous to anisotropic cellular and woolly fibers) and show how these regimes co-evolve with defect density and $sp^2$ fraction, thereby governing sheet resistance, capacitance, wettability, and catalytic activity. Building on this, we review different process control approaches, including laser-assisted transfer, 3D-printing inspired assembly, and multi-pass laser scribing for *in situ* engineering of the resulting LIG, including for property enhancement, doping and nanophase formation. These methods highlight how engineered sequential or hybrid irradiation decouples feature definition from graphitization and enables chemistry and morphology control at scale. A quantitative scalability map is introduced to reveal trade-offs among printing speed, resolution, and sheet resistance, identifying an underexplored window where sub-20 μm features coexist with <100 Ω $sq^{-1}$ conductivity. To ground sustainability claims, we propose a multi-stage energy and emissions framework (from precursor production to laser process control and post-processing) that enables like-for-like comparisons across polyimides, lignin-rich papers, and fossil-based feedstock. Finally, we end with an outlook articulating three key research priorities: (i) systematic precursor libraries that relate monomer chemistry and heteroatom speciation to graphitization kinetics; (ii) *in situ* diagnostics (time-resolved Raman/GC-MS/thermography) to capture transient intermediates; and (iii) manufacturing strategies that combine multiple wavelengths to access uncovered performance windows. By centering chemistry–morphology control within a manufacturing and process-control context, this review offers actionable design rules to translate LIG from benchtop demonstrations to robust, high-throughput devices.

Received 13th October 2025,
Accepted 31st January 2026

DOI: 10.1039/d5nr04319k

rsc.li/nanoscale

Open Access Article. Published on 09 February 2026. Downloaded on 5/23/2026 3:06:13 AM.
This article is licensed under a Creative Commons Attribution 3.0 Unported Licence.

## 1. Introduction

Graphene, a two-dimensional material composed of a single layer of carbon atoms arranged in a hexagonal lattice, possesses exceptional properties, including high electrical and thermal conductivity, optical transparency, specific surface area, and mechanical strength.[1–4] In recent years, graphene-based materials have attracted considerable attention due to their potential applications in various fields, such as electronics, energy storage, and biomedical devices. From a manufacturing perspective, direct laser writing (DLW) has recently emerged as a versatile technique for micro/nanometer-scale patterning across various fields, including being applied in industry and medical science. Using a focused laser beam, DLW induces precise photothermal or photochemical reactions in localized areas, offering exceptional spatial resolution.

[a]*Department of Mechanical Engineering and Materials Science, University of Pittsburgh, 3700 O'Hara Street, Pittsburgh, PA 15261, USA.*
*E-mail: mbedewy@pitt.edu*
[b]*Department of Industrial Engineering, University of Pittsburgh, 3700 O'Hara Street, Pittsburgh, PA 15261, USA*
[c]*Department of Chemical and Petroleum Engineering, University of Pittsburgh, 3700 O'Hara Street, Pittsburgh, PA 15261, USA*

Open Access Article. Published on 09 February 2026. Downloaded on 5/23/2026 3:06:13 AM.
This article is licensed under a Creative Commons Attribution 3.0 Unported Licence.

Unlike traditional methods requiring masks or toxic chemicals, DLW is mask-free, eco-friendly, and efficient, minimizing material waste and substrate damage. Its advantages include high precision, noncontact processing, 3D compatibility, and cost-effectiveness, making it a sustainable and flexible tool for fabricating intricate patterns and structures.[5–8]

Laser-induced graphene (LIG), also referred to as laser-engraved graphene (LEG), laser-scribed graphene (LSG), or laser-induced nanocarbon (LINC), is an innovative graphene-like material synthesized by subjecting specific substrates (solid carbon precursor) to high-intensity laser irradiation.[9] This process involves the photothermal transformation of the substrate material into a highly porous, electrically conductive, and 3D graphene-like structure.[9] LIG was first discovered when J. Lin was trying to lase GO dispersed upon a polyimide (PI) film but accidently missed the target and lased PI instead. The black material on the PI film later proved to be graphene through characterization.[10]

Over the past decade, LIG has significantly expanded the scope of graphene fabrication by enabling direct-write patterning, rapid graphitic conversion in air, compatibility with a wide range of precursors (not limited to PI), and highly customizable laser-enabled manufacturing. These attributes address the complexity and cost of conventional routes for patterned graphene-based composites and devices, avoiding catalyst preparation typical of chemical vapor deposition (CVD) and eliminating the inks required for liquid-assembly and printing approaches commonly used in flexible device manufacturing.[11] LIG has been used in the direct fabrication of high performance as-synthesized functional electrodes on polymers without the need for complex transfer methods (when compared to CVD-synthesized graphene). When compared to printing methods, the lack of multiple printing or annealing steps (either optical or thermal), which are essential for printed graphene electronics, sets LIG apart as a highly promising technology. With tunable properties in the production of various networked and porous 'unprintable' structures that adhere well to the polymer substrate, LIG has been used to create functional thin films, fibrous morphologies, and other surface patterns.[12–14] These demonstrations have become essential building blocks in the development of innovative devices and applications.[12,15–19]

**Current challenges in LIG.** Despite its promising advantages, the fabrication methods and applications of LIG face several challenges that hinder its broader adoption and scalability; these include:

a. *Process science challenges*: achieving consistent and precise control over the morphology and chemical composition of LIG remains a significant challenge in materials science. Variations in carbon precursor properties, laser parameters, and environmental conditions, *etc*. during synthesis can lead to inconsistencies in the quality and performance of the resulting graphene structures. A complete understanding of how thermodynamics and kinetics of the process control the atomic pathways that dictate the LIG structure and properties is yet to be documented, when compared to other routes of graphene synthesis. This is particularly challenging for LIG owing to the rapid nature of the process and the propensity to produce non-equilibrium structures.

b. *Manufacturing precision, scalability, and sustainability*: while LIG demonstrates potential for scalable production, several factors must be addressed for its effective transition to industrial applications. For example, miniaturization requires precise spatial control at the micro-, and sometimes the nano-,

**Zhenhao Wu**

*Zhenhao Wu is a Ph.D. candidate in the Department of Mechanical Engineering and Materials Science at the University of Pittsburgh, working in the NanoProduct Lab under the supervision of Dr. Mostafa Bedewy. His research centers on polymer engineering for laser pyrolysis and direct laser writing, with a focus on designing and synthesizing polymer precursors (particularly polyimide-based systems and nanocomposites) to control laser-polymer interactions and tailor the resulting laser-induced graphene (LIG) structure and properties. In parallel, he develops silk fibroin-based materials by tuning protein secondary structure to enable biocompatible, aqueous-processed platforms for bioapplications. His broader interests include functional polymers and nanocarbon materials for flexible devices, sensors, and related microelectronic technologies.*

**Mirza Sahaluddin**

*Mirza Sahaluddin is a PhD candidate in Mechanical Engineering at the University of Pittsburgh. His research broadly focuses on advanced manufacturing of functional materials, combining hands-on process development with multiphysics modeling and experimental validation. He has extensive experience in laser materials processing (IR, NIR, visible, and UV platforms), thermal and thermo-mechanical simulation (COMSOL, ANSYS), and materials/electrical characterization. More specifically, his current work investigates laser-induced graphene and laser-polymer interactions to establish process-structure-property relationships for scalable devices, including patterned heaters, microfluidics, and thermochromic displays, miniaturized electrodes, and transparent, flexible electronics.*


This journal is © The Royal Society of Chemistry 2026

Open Access Article. Published on 09 February 2026. Downloaded on 5/23/2026 3:06:13 AM.
This article is licensed under a Creative Commons Attribution 3.0 Unported Licence.

scale but laser-based techniques may have inherent limitations in achieving the required resolution. Furthermore, large-scale production must ensure high consistency, batch-to-batch reproducibility, and uniformity across extensive areas, which remains a challenge. This is an inherent problem owing to the nonlinear nature of the laser–matter interactions and their sensitivity to small uncontrolled/unmeasurable variations in the process parameters. From a sustainability perspective, optimizing energy consumption and gaseous emissions, minimizing waste, and exploring eco-friendly precursor materials are critical for ensuring that LIG fabrication remains an environmentally responsible technology that truly excels when compared to traditional energy-intensive synthesis routes like CVD.

c. *Post-processing requirements and fragile adhesion*: LIG-based devices sometimes require additional post-processing steps to optimize their properties or facilitate integration with other materials. These steps can introduce complexities, increase costs, and impact the overall sustainability of the process. Additionally, the adhesion of LIG to its substrate can sometimes be weak if ablation results in removal of loose "flakes" from the surface. Hence, for durable electrodes, measures need to be taken toward measuring and preventing such removal when loaded under external forces with standardization of characterization and quantification. This limits its long-term stability and usability in practical applications. Addressing these challenges requires innovative approaches for not only enhancing substrate binding, but also ensuring toxicity questions are answered for potential biomedical applications, wherein the shedding of any nanocarbon is highly undesirable for any implantable or wearable device.

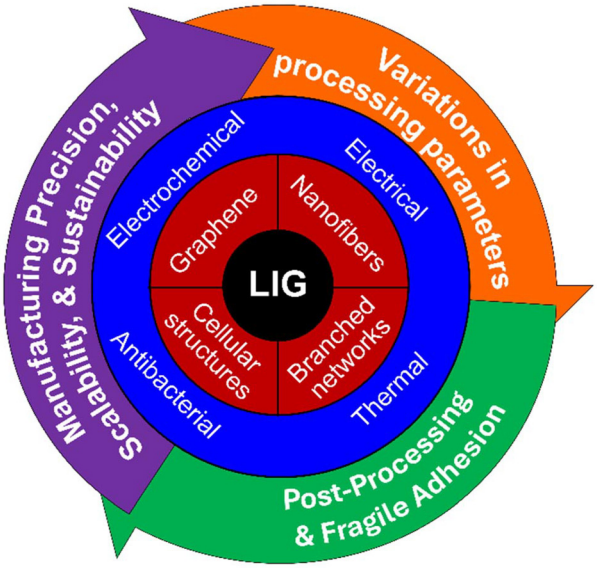


**Fig. 1** Potential of multifunctional LIG (inner circle) and current process and manufacturing challenges (outer circle).

As illustrated in Fig. 1, the key challenges in LIG fabrication (such as control over morphology, scalability, and adhesion) are visually mapped to highlight their central role in current research efforts. The figure emphasizes the ongoing tension between technical limitations and the broader vision for practical implementation, setting the stage for the targeted strategies explored throughout this paper.

**Diala Bani Mustafa**

*Diala Bani Mustafa is a PhD student in Materials Science and Engineering at the University of Pittsburgh. Her research focuses on laser-based surface engineering of polymers, with emphasis on Laser-Induced Nanocarbon Synthesis and Transfer to create conformal graphene-like nanocarbon coatings on various substrates, including surgical meshes. Her work integrates laser processing with materials characterization and interfacial property measurements to establish processing-structure-property relationships for functional surfaces.*

**Soumalya Ghosh**

*Soumalya Ghosh is a PhD candidate in Mechanical Engineering and Materials Science at the University of Pittsburgh, working in the NanoProduct Lab under the supervision of Dr. Mostafa Bedewy. His research focuses on laser-matter interaction and the controlled transformation of polymers into functional nanocarbon materials. He develops laser-based microfabrication strategies to engineer conductive carbon architectures on flexible and multilayer substrates, with an emphasis on understanding process-structure-property relationships. His work integrates pulsed laser processing, microfabrication, and advanced characterization techniques to achieve depth-selective carbonization, tunable electrical transport, and sub-50 μm pattern fidelity. His broader interests include nanomaterials synthesis, carbon science, and flexible electronic systems for sensing and energy applications.*

Open Access Article. Published on 09 February 2026. Downloaded on 5/23/2026 3:06:13 AM. This article is licensed under a Creative Commons Attribution 3.0 Unported Licence.

**Scope and uniqueness of this review**. Accordingly, this review focuses on the process science of LIG and offers a unified framework for understanding how processing dictates structure and, ultimately, performance. A central contribution is our systematic classification of LIG precursors, which organizes the rapidly expanding materials space in a way that clarifies what is fundamentally being converted during lasing and why different feedstocks yield distinct outcomes. Building on this foundation, we synthesize the current understanding of LIG formation mechanisms across laser modalities and parameter spaces, emphasizing how changes in wavelength, fluence, and scan speed/dwell time (and pulse characteristics where relevant) reshape carbonization and graphitization pathways and drive reproducible shifts in morphology: from porous and largely isotropic carbons to anisotropic cellular networks and, at higher energy input, fibrous or ablation-dominated regimes. Rather than treating these results as isolated demonstrations, we explicitly connect process to chemical structure/morphology and measurable properties, highlighting how $sp^2$ reconstruction, defect density, heteroatom retention, porosity/anisotropy, and interfacial adhesion together govern electrical transport and device-relevant performance, while also contextualizing how post-processing and integration strategies (*e.g.*, transfer routes, 3D printing-enabled architectures, and multi-pass laser scribing) can extend functionality and stability. Finally, because practical adoption depends on manufacturability, we critically examine scalability through the throughput–resolution–performance trade-offs, consolidating results reported in the literature (laser wavelength, power, scanning speed, feature size, and sheet resistance) to benchmark manufacturing limits and identify promising operating windows for high-throughput yet high-resolution LIG fabrication of high-performance microelectrodes.

The remainder of the paper is organized to lead the reader from fundamental mechanisms to advanced manufacturing and sustainability considerations. Section 2 focuses on precursor conversion to LIG, beginning with the mechanisms of formation and morphology control, followed by a molecular-level classification of precursors. It first examines single-layer systems (including commercial and engineered polymers, natural derivatives, and fossil-based materials), and then extends to multilayer configurations such as stacked architectures and coated substrates, concluding with a discussion of sustainability aspects. Section 3 explores modified laser processes that expand the functionality of LIG, covering transfer techniques, 3D-printing-inspired fabrication, and multi-pass or secondary laser scribing for *in situ* doping and morphology refinement. Section 4 transitions from laboratory-scale investigations to scalable manufacturing and miniaturization, analyzing throughput–resolution trade-offs, considering laser wavelength, speed, resolution, and conductivity. Finally, Section 5 provides the conclusion and outlook, summarizing key insights, identifying remaining limitations, and outlining future research directions aimed at translating LIG from experimental studies to practical, high-throughput technologies.

**Mostafa Bedewy**

*Dr Mostafa Bedewy is an Associate Professor and Director of Graduate Studies for Materials Science and Engineering, Department of Mechanical Engineering & Materials Science, Department of Chemical & Petroleum Engineering (secondary appt.), and Department of Industrial Engineering (secondary appt.) at the University of Pittsburgh (Pitt), where he leads the NanoProduct Lab. Before Pitt, he was a postdoc at MIT. In 2013, he completed his PhD at the University of Michigan – Ann Arbor. Dr Bedewy received the CAREER award from NSF in 2023, the Frontiers of Materials Award from TMS in 2022, the Outstanding Young Investigator Award from IISE M&D division in 2020, the Outstanding Young Manufacturing Engineer Award from SME in 2018, the Ralph E. Powe Junior Faculty Enhancement Award from Oak Ridge Associated Universities (ORAU) in 2017, the Robert A. Meyer Award from the American Carbon Society in 2016, the Richard and Eleanor Towner Prize for Distinguished Academic Achievement from University of Michigan in 2014, and the Silver Award from MRS in 2013. His interests include nanomaterials, carbon science, biomaterials, laser processing, and flexible electronics.*

## 2. Precursor conversion to LIG

### 2.1. Mechanism of LIG formation and morphology control

The formation of LIG from polymers is predominantly photothermal, driven by the extreme temperatures and rapid heating rates generated during laser irradiation. High-intensity lasers create highly localized thermal and mechanical transients that can reach temperatures above 2400 K and pressures up to several gigapascals, enabling the conversion of $sp^3$-hybridized carbon in polymer backbones into $sp^2$-rich graphitic domains.[20,21] In polyimide (PI), this transformation begins with bond scission and de-functionalization within the moving heat-affected zone (Fig. 2): spectroscopic studies of laser-irradiated Kapton report the depletion of heteroatom-containing functionalities (imide/ether-related vibrations) consistent with the cleavage of C–N/C–O linkages and release of O/N-containing volatiles.[22,23] At the same time, plume/ablation diagnostics of UV-laser-irradiated PI directly evidence backbone fragmentation and gas-phase products typical of rapid pyrolysis (*e.g.*, $CO/CO_2$, HCN, and small hydrocarbons), supporting the volatile-evolution route summarized schematically in Fig. 2b.[24] As these species leave, the remaining carbon-rich skeleton densifies into a disordered (amorphous) carbon inter-

 This journal is © The Royal Society of Chemistry 2026

Open Access Article. Published on 09 February 2026. Downloaded on 5/23/2026 3:06:13 AM.
This article is licensed under a Creative Commons Attribution 3.0 Unported Licence.

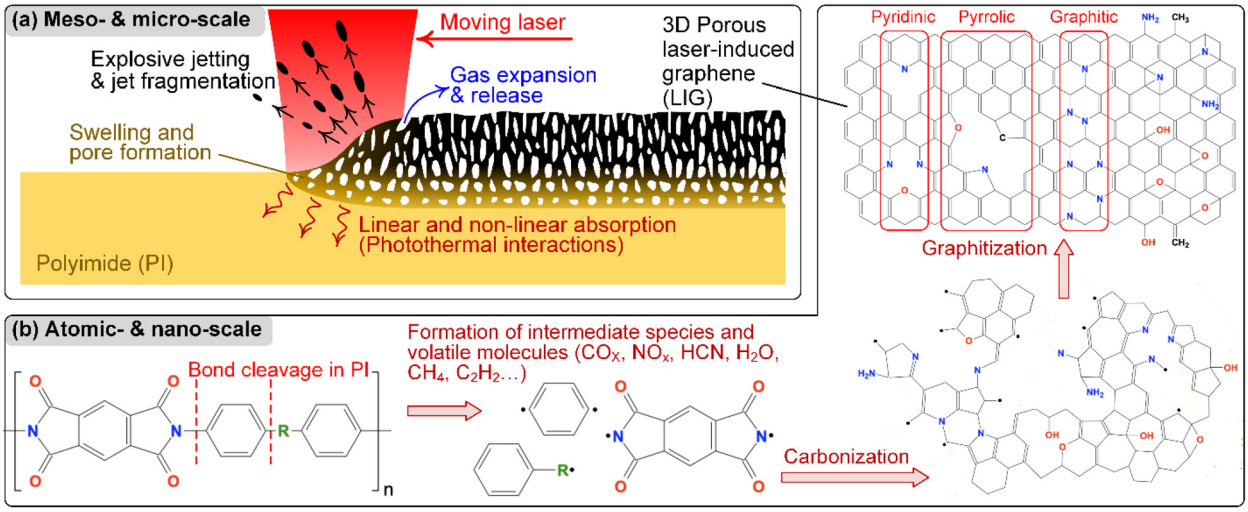


**Fig. 2** Multi-scale schematic of LIG formation from PI. (a) Meso-/micro-scale: a moving laser locally heats PI *via* photothermal absorption, driving rapid pyrolysis; volatile expansion causes swelling/pore formation and, at higher energy input, burst/ejection to yield a 3D porous LIG layer. (b) Atomic-/nano-scale: bond cleavage in PI produces radical intermediates and volatiles (*e.g.*, $CO_x$, $NO_x$/HCN, $H_2O$, light hydrocarbons), leaving a carbon-rich intermediate that carbonizes and graphitizes into an $sp^2$ network with residual N/O functionalities.

mediate; reactive MD/ReaxFF simulations further suggest that continued energy input drives aromatization, ring growth, and coalescence of graphene-like clusters from this transient amorphous phase, highlighting the kinetic nature of graphitization under ultrafast heating and cooling.[21,25] Experimentally, PI-derived LIG commonly retains a fraction of heteroatoms as pyridinic/pyrrolic/graphitic N (and oxygenated edge sites), consistent with the coupled carbonization/graphitization pathways proposed for PI under laser irradiation.[12,25] At larger length scales, the same rapid generation and expansion of volatiles inflates the softened surface to nucleate pores and, above threshold conditions, can trigger bubble bursting, plume formation, and even material ejection, 'pyrolytic jetting', providing a direct physical origin of the porous 3D architectures depicted in Fig. 2a.[23,26] Collectively, these tightly coupled chemical (bond scission to volatilization to carbonization/graphitization) and physical (swelling/foaming/jetting) processes provide the mechanistic basis for why LIG morphology is exceptionally sensitive to laser fluence, scan speed (dwell), focal conditions, and ambient atmosphere.

The resulting morphology and graphitization quality are governed by how energy is deposited and dissipated, which depends on both the precursor properties and irradiation conditions. Key variables include the polymer precursor (optical absorption and thermal transport), laser wavelength, and processing parameters such as power, scan speed, and beam defocus, as well as pulse shape, duration, and repetition frequency. For example, mid-infrared $CO_2$ lasers primarily drive photothermal conversion, whereas UV irradiation can introduce additional photochemical pathways that alter surface evolution and graphitization outcomes.[27] Because the laser-written region cools rapidly, LIG often solidifies into non-equilibrium, polycrystalline carbon featuring topological defects such as five- and seven-membered rings.[12,28] Establishing these process–structure relationships is essential for rationally optimizing LIG synthesis and tailoring properties for targeted applications.

Among processing descriptors, laser fluence (energy delivered per unit area) provides a convenient, unifying metric to rationalize morphology evolution because it directly governs the extent of carbonization, gas evolution, and carbon restructuring. For continuous-wave $CO_2$ lasers, low fluence typically yields a porous, largely isotropic carbon morphology associated with progressive carbonization, whereas intermediate fluence can drive the emergence of anisotropic cellular networks with higher $sp^2$ content and improved electrical transport. At higher fluence, a further shift toward 'woolly' nanofiber-like morphologies has been reported; despite stronger carbonization and reduced heteroatom content, conductivity along laser-written tracks can decrease due to disrupted percolation pathways.[29] In this high-fluence regime, Tour and coworkers additionally reported 'laser-induced glassy carbon nanofiber trees', explicitly positioning glassy carbon, electrochemically relevant, mostly amorphous, conductive carbons, and showing that ablation-dominated lasing conditions can produce dendritic fibrous morphologies that are visually reminiscent of woolly fibers but are not highly graphenic at the nanoscale.[30] Specifically, they used a much higher areal energy dosage ($\approx$400 J cm$^{-2}$) than that typical of LIG processing, where local ablation and rapid ejection/air-quenching are proposed to preserve a glassy (amorphous) nanostructure under transient tensile stress.[30]

To move beyond morphological analogy and quantitatively connect energetics and kinetics to these fibrous outcomes, Abdulhafez *et al.*[29] mapped fluence-dependent transitions on PI using beam modeling and correlative microscopy/spectroscopy, identifying a porous to cellular transition (T1) near $\approx$12 J cm$^{-2}$ and a cellular to woolly-fiber transition (T2) near

Open Access Article. Published on 09 February 2026. Downloaded on 5/23/2026 3:06:13 AM.
This article is licensed under a Creative Commons Attribution 3.0 Unported Licence.

≈17 J cm$^{-2}$, while also showing that cellular networks maximize conductivity (linked to lateral connectivity and higher graphitic content) and that woolly fibers can exhibit comparatively lower-quality sp$^2$ signatures than the cellular regime. As summarized in Fig. 3, SEM images, Raman signatures, and process maps collectively illustrate how increasing fluence drives the progression from porous to cellular to fibrous regimes, underscoring why fluence tuning is central to engineering LIG performance.[29] Building directly on this framework, their newer work further demonstrates how processing kinetics (scan speed/dwell) governs whether high-fluence pathways yield fibers or instead enter an ablation regime: woolly fibers disappear below ≈312 mm s$^{-1}$, and a distinct low-speed ablation threshold (T3) emerges after T1, producing cratered, hierarchically porous morphologies with improved graphitic ordering; critically, modeling links T1 and T3 primarily to tempera-

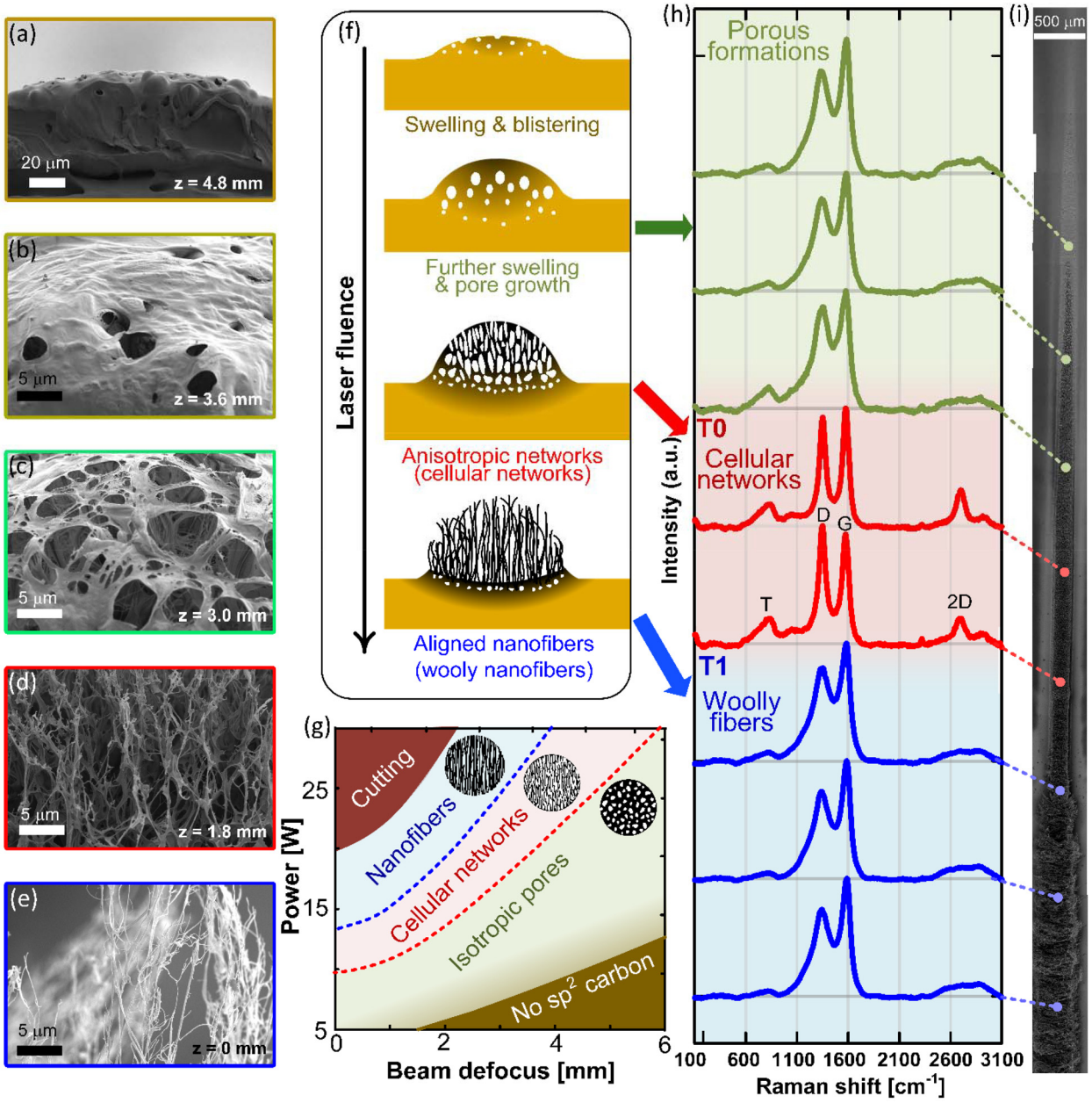


**Fig. 3** The relationship between laser fluence and resultant LIG morphology. (a) SEM image of swelling of polyimide. (b) SEM image of pore formation and growth. (c) SEM image of the increase in pore shape anisotropy. (d) SEM image of the formation of anisotropic cellular networks. (e) SEM image of the formation of wooly fibers. (f) Schematic illustration of the evolution of LIG formation with increasing fluence, showing the transitions from porous structure to cellular network to wooly fiber. (g) Morphology diagram mapping the ranges of laser parameters for creating LIG with different morphologies. (h) Raman spectra of different points along the LIG line and the corresponding location in SEM ($\gamma$ = 45°, power $P$ = 18.4 W, speed $v$ = 500 mm s$^{-1}$), showing the transition from isotropic porous LIG to cellular networks, as well as the transition to wooly fibers. (i) Stitched SEM images of lased LIG line. This figure has been adapted from ref. 29 with permission from American Chemical Society, copyright 2021.


This journal is © The Royal Society of Chemistry 2026

Open Access Article. Published on 09 February 2026. Downloaded on 5/23/2026 3:06:13 AM.
This article is licensed under a Creative Commons Attribution 3.0 Unported Licence.

ture-dominated conditions associated with PI graphitization (≈2500–3000 °C) and graphite ablation (≈3300 °C), whereas the fiber-forming T2 transition is strongly rate/speed dependent and can even be pre-empted by ablation under some conditions.[31]

Area writing is more complex than single-track lasing because an 'area' is formed by raster/hatch filling with closely spaced scan lines. As the beam steps to adjacent lines, each point undergoes repeated heating and cooling, so the peak temperature and cooling rate depend on line spacing, scan direction (unidirectional *vs.* bidirectional), and dwell/turn-around at hatch ends. Thus, 'coverage' is both geometric and kinetic: insufficient overlap can leave poorly connected inter-line boundaries that limit conductivity. Liu *et al.*[32] framed this using spot-superposition/energy-coefficient concepts, where the scan-line spacing set by image resolution (dpi) and overlap between successive spots/lines (including defocus-driven spot broadening) governed the effective carbonization dose and uniformity of LIG. Similarly, Tour's 'multiple lasing' exploits high raster density to create many overlapping exposures per location (*e.g.*, ≈37 at 1000 dpi for a 175 μm spot), with defocus further increasing overlap by enlarging the spot.[33]

Practically, overlap must be tuned because it improves electrical continuity but also increases thermal–mechanical damage during large-area writing. In kirigami-based transparent, flexible EMI shields, Sahaluddin *et al.*[34] combined multi-pass vector cutting with two-pass (defocused) raster conversion of PI and optimized the raster gap: 152 μm caused severe warping and occasional delamination, 355 μm reduced warping while maintaining overlap, and gaps >450 μm eliminated overlap, increasing sheet resistance by five orders of magnitude. This shows that the area-LIG performance is often governed by percolation across scan-line boundaries, making hatch spacing/raster gap and local heat dissipation first-order variables; importantly, the same gap-controlled overlap also programs the surface texture periodicity and pore connectivity, so wettability/adhesion can vary substantially with scan strategy. For example, Abdulhafez *et al.*[35] showed that increasing the line-to-line gap (reducing overlap) could shift LIG from wicking/low-contact-angle behavior to higher contact angles with stronger anisotropic wetting, where droplets were pinned on periodic lines and spread directionally. More recently, Nam *et al.*[36] tied line pitch (101.6–508 μm) and overlap-driven cumulative fluence to morphology/chemistry and wetting: small-pitch, highly overlapping scans yielded more uniform, less anisotropic hydrophilic textures, whereas a nonoverlapping 355.6 μm pitch produced superhydrophobic F-doped LIG ($\theta_{\perp} \approx 156°$) with pronounced anisotropy and parahydrophobic adhesion.

Beyond geometric overlap, sequential irradiation (re-lasing) can further refine the carbon network after an initial pass. Abdulhafez *et al.*[37] showed that speed-dependent sequential irradiation (an initial raster followed by a second raster over the same area) could reduce the effective resistivity (0.14 to 0.08 Ω cm), lower the sheet resistance at an optimized raster gap, and markedly decrease the electrochemical impedance in biosensors. The benefit is precursor- and stability-dependent: for photoresist-derived LIG, sequential lasing is needed to convert PR into amorphous carbon and then PR-LIG, but excessive raster passes can increase sheet resistance due to cracking/blistering.[38] Related 'stepwise' schemes (focused then defocused) can heal defects and improve crystallinity, yielding much lower sheet resistance than single-pass LIG.[39] Consistent with this non-monotonic trend, PI studies report that thickness/graphitization often peak at an intermediate pass number before declining at higher passes due to stress-related damage.[40]

These multi-pass/area-writing effects can be interpreted through the same energetics–kinetics framework as single-line morphology maps: overlap, hatch spacing, and pass count alter both the total dose and the time–temperature profile (peak temperature, dwell above key thresholds, and cooling rate). Kinetic analyses and process maps link morphology transitions to specific temperature windows and scan-speed-dependent heating rates, implying that overlap-driven thermal accumulation can push a raster fill into a different regime than an isolated line at the same nominal settings.[31] Manufacturing constraints also matter: in additively manufactured PI, scan-line disruptions and adhesion loss measurably increase sheet resistance, underscoring hatch spacing and scan strategy as first-order variables for high-conductivity, large-area LIG.[41]

### 2.2. Classification of precursors: molecular-level understanding

The investigation of carbon precursors for LIG synthesis is driven by the need to understand the fundamental mechanisms behind their suitability and to explore their potential for future applications. By analyzing different precursor types—ranging from synthetic polymers and multi-component polymer systems to natural bio-based materials and fossil-derived products—researchers aim to uncover the key factors that influence LIG formation, such as molecular structure, carbon content, and doping potential.[42,43] This understanding not only facilitates the optimization of LIG synthesis for specific applications, such as energy storage, sensing, and flexible electronics, but also informs the development of more sustainable and scalable production methods.[44,45] Ultimately, studying the diverse range of precursors provides critical insights into future directions and the industrial potential of LIG technology.

Combined with the exploration of the above-mentioned process parameter space, hypothesis-driven research is formulated to create LIG with a tailored structure/chemistry and desirable properties. At this point, a robust taxonomy is needed from a materials science perspective, in order to review the current state-of-the-art in LIG morphology and chemistry control. In Fig. 4, carbon precursors are systematically categorized into distinct groups to facilitate a comprehensive understanding of the rationale behind investigating various precursors.

Equally important to precursor classification is the role of laser fluence in shaping LIG morphology for each precursor.

Open Access Article. Published on 09 February 2026. Downloaded on 5/23/2026 3:06:13 AM.
This article is licensed under a Creative Commons Attribution 3.0 Unported Licence.

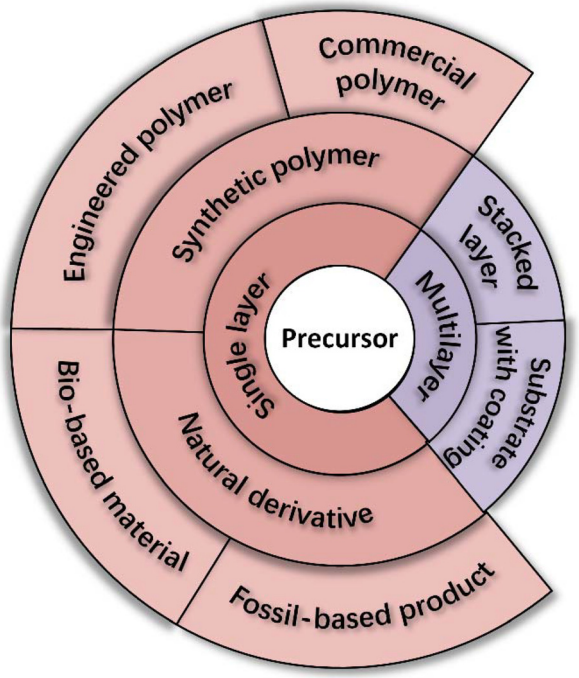


Fig. 4 The classification of different LIG precursors, according the section titles in this review.

The combination of precursor structure/chemistry and laser parameters controls the underlying physicochemical processes in unison, driving structural evolution during carbonization and graphitization.[29] Morphological transitions arise from the interplay between competing effects, such as localized heating, carbonization kinetics, outgassing dynamics, and phase transformations. Adjusting the fluence and kinetics for each precursor enables precise control over graphitization, defect formation, and anisotropy, leading to distinct structural outcomes ranging from isotropic porous networks to highly anisotropic graphitic domains. Hence, establishing the relationship between each precursor and the fluence-dependent morphology enables researchers to refine predictive models of LIG formation, offering deeper insights into laser–material interactions in nonequilibrium environments.[29] This knowledge is crucial for systematically tailoring LIG at the nanoscale, enhancing its properties for various applications.

### 2.3. Single layer

A single-layer carbon precursor refers to a material where the intrinsic properties of the bulk precursor alone determine its value and functionality. It does not rely on additional coatings, layers, or modifications to enhance performance, as its inherent characteristics, such as structure and composition, are sufficient for its intended use. These materials are valued for their simplicity, purity, and ability to perform without external enhancements. Single-layer carbon precursors can be classified as synthetic polymers and natural derivatives.

**2.3.1. Synthetic polymers.** Synthetic polymers are man-made macromolecules that serve as widely used and generally reproducible feedstocks for LIG studies. In this review, we classify synthetic polymer precursors by formulation transparency, separating commercial polymers from engineered polymers: commercial polymers are off-the-shelf, industrially manufactured products, the practical performance of which often comes from a formulated matrix that may include proprietary crosslinkers, stabilizers, fillers, pigments, or thermally conductive additives, so the full chemical recipe is not always disclosed and can vary across products. Engineered polymers, in contrast, are synthesized from clearly identified monomers/precursors under controlled conditions, with compositions that are known (aside from minor impurities) and typically free of undisclosed additives, enabling laser-induced carbonization/graphitization trends to be interpreted directly in terms of polymer chemistry. This distinction helps explain why LIG outcomes can be difficult to compare across commercial products even when the nominal backbone is similar, whereas engineered systems support cleaner process–structure–property comparisons.

I. Commercial polymer

The use of commercial polymers such as Kapton, pyromellitic dianhydride–pyromellitic dianhydride (PMDA-ODA: $(C_{22}H_{10}N_2O_5)_n$), polyethylenimine (PEI: $(C_2H_5N)_n$), and polyether ether ketone (PEEK: $(C_{19}H_{12}O_3)_n$), for synthesizing laser-induced graphene (LIG) has gained significant attention due to their availability, cost-effectiveness, and exceptional material properties.[46] These polymers are particularly suited for LIG synthesis as they contain aromatic rings and $sp^2$-hybridized carbon atoms, which facilitate the photothermal conversion process during laser irradiation.[47] Their aromatic structures offer a high carbon content for efficient graphitization under localized high temperatures, while their thermal stability and chemical robustness enable them to withstand intense laser energy without significant ablation, ensuring consistent, high-quality graphene formation.[48] Furthermore, their compatibility with scalable laser-based methods, such as direct laser writing, and their tunable properties make them ideal for a range of applications, including energy storage, sensing, and flexible electronics.[49] These attributes have positioned these polymers as promising candidates for cost-effective and sustainable graphene production at industrial scales.

**What makes a precursor suitable for graphitization**. In carbon-precursor science, the distinction between graphitizing and non-graphitizing carbons is typically traced to how readily a precursor can evolve into larger, more planar polyaromatic nanodomains that can stack and anneal toward graphene-like order.[50,51] Aromatic backbones (benzene/heteroaromatic rings are embedded along the main chain) start from ring-rich, relatively low H/C motifs that can rapidly fuse and expand under laser heating, whereas aliphatic backbones dominated by saturated C–C/C–H σ-bonds preferentially undergo chain scission and volatilization before extensive aromatization, yielding low char and more disordered 'hard carbon' unless additional stabilization is introduced.[50–52] Accordingly, a precursor's graphitizability is governed not only by carbon yield but also by whether early three-dimensional crosslinking locks in curva-

 This journal is © The Royal Society of Chemistry 2026

Open Access Article. Published on 09 February 2026. Downloaded on 5/23/2026 3:06:13 AM. This article is licensed under a Creative Commons Attribution 3.0 Unported Licence.

ture/defects (favoring non-graphitizing carbon) or whether rearrangement/mass transport remains possible during the brief high-temperature window of lasing to enable nanodomain growth and stacking. From a practical LIG perspective, an ideal precursor therefore combines a high aromatic content (or rapid aromatization), high thermal stability/char yield, strong absorption at the relevant laser wavelength, and chemistry that supports controllable gas evolution/doping without runaway ablation.[51,52] For 'poor' precursors, such as polypropylene (PP), reported approaches include suppressing oxidative loss under controlled/inert atmospheres and leveraging silicone/PDMS-assisted lasing to provide a high-yield framework that retains carbon and promotes graphene-like restructuring; in parallel, PP pre-stabilization/crosslinking strategies can increase the carbon yield and make subsequent graphitization more accessible.[53–55]

**How researchers use different laser systems to grow LIG on Kapton**. Since the discovery of LIG in 2014, Kapton has been widely adopted as a model precursor because its aromatic, thermally robust backbone supports rapid photothermal carbonization and $sp^2$ reconstruction under laser irradiation.[12] A range of laser platforms ($CO_2$, Nd:$YVO_4$, Yb:KGW, and diode lasers) has therefore been used to tune the energy-deposition depth and resulting temperature–time history, which in turn governs outgassing dynamics, pore evolution, defect density, and electrical transport in the converted LIG layer.

As shown in Fig. 5a(I), 10.6 μm $CO_2$ irradiation drives efficient, predominantly photothermal conversion to a thick, highly porous LIG network; however, the relatively deep thermal interaction volume can broaden the heat-affected zone and constrain the minimum achievable feature size on Kapton.[47] Fig. 5a (II) shows that 1064 nm Nd:$YVO_4$ processing accesses a different absorption/thermal-diffusion regime, enabling more volumetric conversion and producing comparatively uniform, mechanically robust porous networks with strong areal conductivity.[56] Fig. 5a(III) highlights that 515 nm Yb:KGW femtosecond pulses confine energy delivery in time, reducing collateral heating and enabling more precise control over the microstructure and surface chemistry (*e.g.*, defect density and wettability) through pulse and scan-parameter tuning.[57] In contrast, 405 nm diode lasers provide a compact, low-cost route with a practical processing window between carbonization and ablation, yielding nanocrystalline LIG, the conductivity and disorder of which can be systematically adjusted by laser power and dwell time.[58] Finally, Fig. 5a(IV) illustrates the use of 355 nm Nd:$YVO_4$ lasers to enable the precise fabrication of thin, microporous LIG films with enhanced spatial resolution and reduced penetration depth.[48] This method transforms polyimide substrates into few-layer graphene with a foamy microstructure, improving the surface area and electrical conductivity.[48] Altogether, these properties enhance the energy storage efficiency and electromechanical sensitivity, while the approach ensures reproducibility and scalability for large-scale manufacturing, maintaining high thermal stability and conductivity.[48,49]

**Other commercial plastic that can grow LIG**. Beyond Kapton, several commercially available aromatic plastics and resin-based laminates (including phenolic paper/resins, PEI, polyethersulfone (PESU: $(C_{12}H_8O_3S)_n$), PEEK, and polycarbonate (PC: $(C_{16}H_{14}O_3)_n$)) have also been demonstrated as viable LIG feedstocks. Phenolic paper can be directly converted by $CO_2$ laser scribing into porous, graphene-like carbon tracks.[59] Commercial phenolic resins are also attractive, high-char-yield precursors for high-purity porous carbon, and direct laser writing can generate patterned porous carbon electrodes with a strong multifunctional performance: ≈5–10× higher electrochemical sensing sensitivity than glassy carbon, enhanced micro-supercapacitor capacitance with stable cycling, and robust low-voltage Joule heating.[60] In boron-modified phenolic resin (BPF), high-energy continuous-wave laser irradiation drives sustained decomposition into a porous residual char, the graphitic order of which increases with irradiation time; the resulting combination of improved char thermal stability and pore-mediated thermal insulation helps suppress damage propagation into the bulk, clarifying why these resins exhibit unusually high laser ablation resistance.[61]

For thermoplastic engineering polymers, Gerringer *et al.*[46] showed that conductive, RF-responsive graphitic surface structures could be produced on PEI, PESU, PEEK, and PC using a conventional laser cutting platform, while the RF heating response (reported up to ≈126 °C $s^{-1}$) provided an indirect but practical performance metric for comparing how laser parameters and substrate chemistry translated into electrically continuous $sp^2$ networks. PEEK has been further processed by laser direct writing to form patterned LIG interdigital electrodes on the native polymer film, illustrating that high-temperature semicrystalline matrices can tolerate both the laser-induced carbonization step and subsequent processing while retaining mechanically robust, conductive features.[46,62]

As illustrated in Fig. 5b, Teflon, polytetrafluoroethylene (PTFE: $(C_2F_4)_n$), with its fluorinated backbone, can be converted into fluorinated graphene (FG) or fluorinated nanodiamonds (FNDs) using pulsed $CO_2$ laser irradiation under an inert atmosphere.[63] Fig. 5b(I) shows the reaction scheme for this laser-induced transformation, while Fig. 5b(II) and (III) display high-resolution XPS spectra confirming the evolution from C–F bonds in pristine Teflon to $sp^2$-hybridized carbon in FG. This process highlights the critical role of laser conditions and atmospheric control in tuning the LIG composition from fluorinated polymers.[63] Poly(paraphenylene terephthalamide) (Kevlar), a highly aromatic and mechanically robust material, can also be converted into porous graphene structures with high electrical conductivity and mechanical flexibility using femtosecond or $CO_2$ lasers. For instance, laser-scribed Kevlar has been utilized to fabricate flexible strain sensors with a gauge factor of 185.2 and a fast response time of 18 ms, outperforming state-of-the-art textile-based sensors. These strain sensors are capable of monitoring human physiological signals and dynamic composite strains in real time.[64] Additionally, Janus graphene/Kevlar textiles, which maintain Kevlar's structural integrity while incorporating a graphene layer, have been developed for intelligent protective clothing, demonstrating applications in Zn–air batteries, gas sensors, and self-powered systems.[65]

Open Access Article. Published on 09 February 2026. Downloaded on 5/23/2026 3:06:13 AM.
This article is licensed under a Creative Commons Attribution 3.0 Unported Licence.

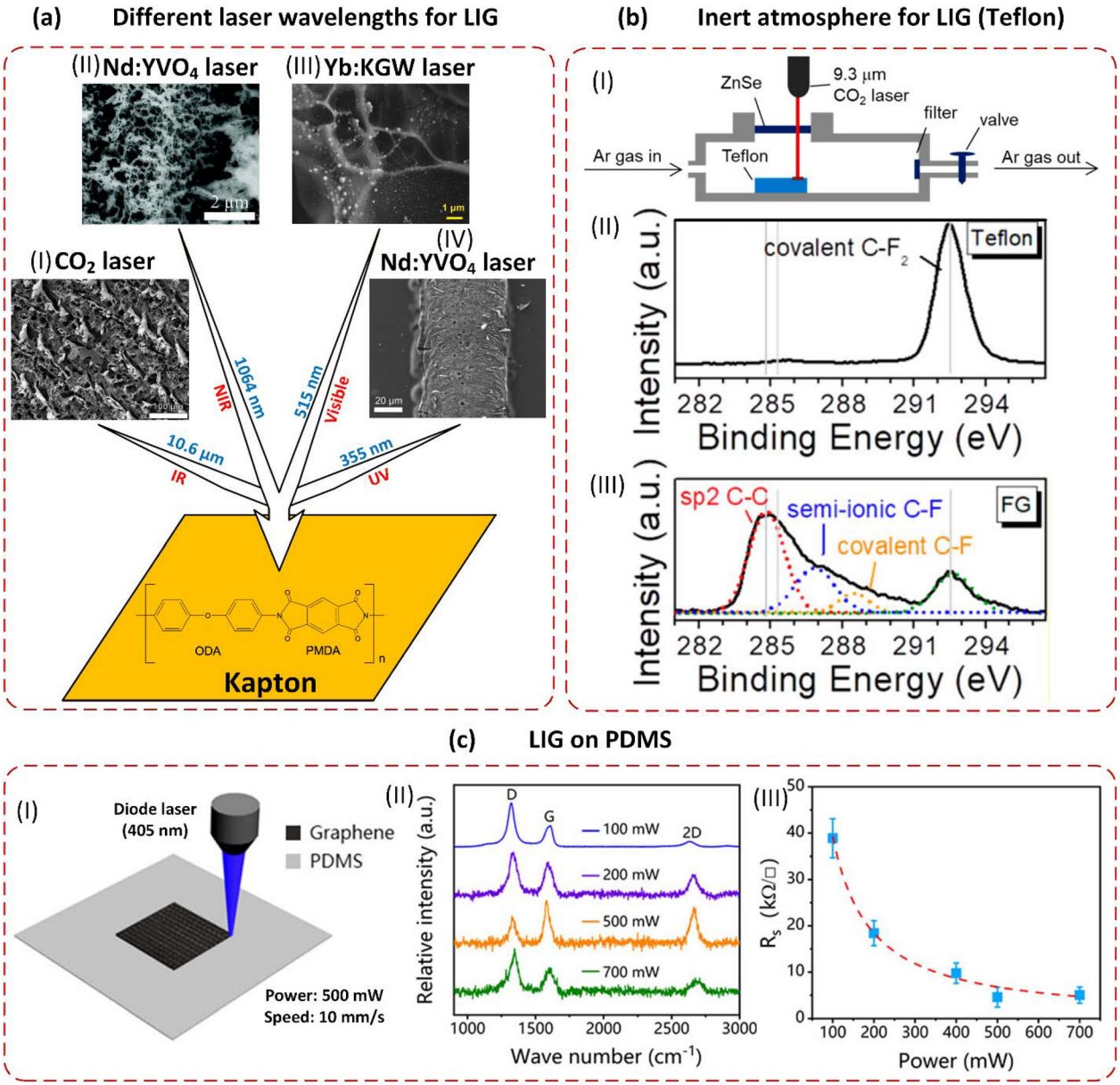


**Fig. 5** Commercial polymers for LIG. (a) Different laser sources ($CO_2$, Yb:KGW, and Nd:$YVO_4$ laser) can be used to grow LIG on Kapton. (I) The SEM image of 10.6 μm $CO_2$ laser induced graphene. This figure has been adapted from ref. 46 with permission from American Chemical Society, copyright 2019. (II) The SEM image of 1064 nm Nd:$YVO_4$ laser induced graphene. This figure has been adapted from ref. 56 with permission from Royal Society of Chemistry, copyright 2018. (III) The SEM image of 515 nm Yb:KGW laser induced graphene. This figure has been adapted from ref. 57 with permission from Elsevier, copyright 2024. (IV) The SEM image of 355 nm Nd: $YVO_4$ laser induced graphene. This figure has been adapted from ref. 48 with permission from John Wiley and Sons, copyright 2018. (b) Growing LIG on Teflon requires an inert atmosphere. (I) Reaction scheme of lasing on Teflon. (II) High-resolution C 1s XPS results for Teflon. (III) High-resolution C 1s XPS results for fluorinated graphene (FG). This figure has been adapted from ref. 63 with permission from American Chemical Society, copyright 2018. (c) Growing LIG on PDMS. (I) Schematic illustration of direct laser scribing of PDMS films and the corresponding laser parameters. (II) The Raman spectra of LIG on PDMS using different laser powers. (III) Relationship between laser power and resultant sheet resistance of the LIG film. This figure has been adapted from ref. 66 with permission from American Chemical Society, copyright 2019.

**PDMS for growing LIG.** In addition to the carbon-backbone commercial plastics discussed above, we separately highlight polydimethylsiloxane (PDMS: $CH_3[Si(CH_3)_2O]_nSi(CH_3)_3$), a synthetic elastomer with a silicone-based backbone rather than a carbon backbone. Within our classification scheme, PDMS is treated as a commercial polymer with a less well-defined formulation, typically supplied as a mixture of a silicone base and proprietary crosslinker(s), so its laser-induced carbonization/graphitization behavior is expected to differ from that of engineered polymers with known, purely carbon-based backbones.

 This journal is © The Royal Society of Chemistry 2026

Open Access Article. Published on 09 February 2026. Downloaded on 5/23/2026 3:06:13 AM. This article is licensed under a Creative Commons Attribution 3.0 Unported Licence.

Zhu *et al.*[66] developed a cost-effective method to directly convert PDMS into graphene films using a blue diode laser in ambient air. The resulting sensors for health monitoring demonstrated exceptional performance, including high sensitivity (≈480 $kPa^{-1}$), rapid response times (2–3 μs), and durability over 4000 cycles. Fig. 5c(I) shows a schematic illustration of this direct laser scribing setup, along with the corresponding laser parameters; Fig. 5c(II) presents the Raman spectra of LIG on PDMS under different laser powers, clearly showing the enhancement in graphitic quality with increasing power; Fig. 5c(III) further illustrates the relationship between laser power and the resulting sheet resistance, which decreases significantly with higher power, confirming the tunability of conductivity through laser control.[66] On the other hand, Zaccagnini *et al.*[67] managed to further enhance the quality of LIG produced from PDMS by incorporating triethylene glycol (TEG: $C_6H_{14}O_4$) as a carbon precursor. Adding TEG improved the graphitization process, reducing the sheet resistance of LIG by two orders of magnitude, down to 130 Ω $sq^{-1}$. The PDMS-TEG composite also exhibited high specific capacitance values of up to 287 μF $cm^{-2}$, positioning it as a promising candidate for flexible micro-supercapacitors.[67]

**Understanding the mechanism of LIG optimization**. Because laser-induced graphitization occurs on nanosecond to picosecond timescales that are difficult to probe experimentally, simulation-based studies have become essential for elucidating LIG formation mechanisms and systematically screening the effects of different precursors and laser parameters. Vashisth *et al.*[25] used ReaxFF molecular dynamics to explore LIG synthesis from polymers such as Kapton, poly(bismaleimide-*co*-divinylbenzene) (PBM: $(C_{20}H_{12}N_4)_n$), PEI, PEEK, and PC. They found that LIG formation progressed through a transition from amorphous carbon to graphitic structures at optimal temperatures (2500–3000 K), with PBM yielding the highest carbon retention, and PEEK and PEI producing LIG with superior surface areas ideal for electrocatalytic applications. Conversely, PC-derived LIG, rich in 5- and 7-membered carbon rings, exhibited reduced conductivity.[25] Chen *et al.*[68] extended this understanding by identifying key parameters for UV laser-induced LIG formation from polyimide (PI). Their study demonstrated that a heat preservation duration of 600 ps at 3000 K was crucial for producing defect-free graphene flakes, while shorter durations led to incomplete graphitization.[68] Murray *et al.*[69] further optimized laser parameters for $CO_2$ laser-induced LIG, showing that non-linear interactions between laser power and scan speed significantly impacted morphology and sheet resistance. Optimized conditions produced LIG with sheet resistances as low as 16 Ω $sq^{-1}$, highlighting the potential for scalable, high-quality graphene production.[69]

**The prospect of commercial polymers**. Looking forward, the potential of commercial polymers for LIG production lies in their compatibility with scalable processes like roll-to-roll manufacturing and direct laser writing. Advances in laser technology, such as ultrafast UV lasers for precise and localized activation, enhance LIG's functional properties, including porosity, heteroatom doping, and surface wettability.[49] The availability, cost-effectiveness, and adaptability of these polymers further position them as key materials for large-scale, sustainable graphene production, enabling applications in energy systems, environmental sensing, and flexible electronics.[38,47,63]

**Summary of the section**. Throughout the literature on LIG derived from commercial polymers, Kapton remains the dominant precursor, with a smaller set of studies extending the same laser-scribing approach to other commercially available products such as PEI, PEEK, and PC. In most cases, LIG can be produced on these commercial polymers without any pretreatment and under ambient air conditions, with PTFE (Teflon) being a notable exception that typically requires an inert atmosphere to enable successful conversion. Regarding laser sources, $CO_2$ lasers are used most frequently, although Nd:$YVO_4$, Yb:KGW, and diode lasers have also been demonstrated for commercial-polymer substrates. Reported electrical performance can be strong, with the sheet resistance reaching as low as ≈15 Ω $sq^{-1}$, while the resulting morphology is not uniform across studies and can range from relatively dense to highly porous structures. Chemically, the bonding in commercial-polymer-derived LIG is dominated by C–C, with additional contributions from functionalities such as C═C, C–N, C═N, C–O, C–O–H, and O═C–C. Overall, these commercial-polymer systems commonly yield LIG with a high $sp^2$ content and relatively high crystallinity, as reflected by 2D/G ratios up to approximately 0.65 (all the data are summarized in Table S1).

II. Engineered polymers

On the other hand, researchers are increasingly focused on developing engineered polymer precursors for LIG synthesis to overcome the limitations associated with commercial polymers and tailor material properties for specific applications. While commercial polymers like Kapton and PEI offer convenience and scalability, their fixed chemical compositions and structural features restrict the ability to fine-tune the resulting LIG properties, such as conductivity, porosity, and chemical functionality.[70] Engineered polymers, on the other hand, can be designed with precise control over their molecular structure, enabling the incorporation of heteroatoms (*e.g.*, nitrogen, boron, sulfur) or functional groups to enhance LIG performance for targeted applications, such as energy storage, catalysis, and sensing.[71,72] Additionally, these custom precursors allow researchers to optimize the yield and quality of LIG by minimizing unwanted byproducts and improving the conversion efficiency during laser processing. The ability to create tailored materials that address specific performance requirements drives the development of engineered polymers as a flexible and innovative alternative to commercial precursors for LIG synthesis. Engineered polymers can be classified as unfilled polymers and multi-component polymer systems.

A. Unfilled polymers

An unfilled engineered polymer is a material composed of a single type of polymer, without any added fillers or reinforcements, where its inherent properties determine its functionality and performance. Unfilled polymers can be classified as homopolymers and copolymers.

Open Access Article. Published on 09 February 2026. Downloaded on 5/23/2026 3:06:13 AM. This article is licensed under a Creative Commons Attribution 3.0 Unported Licence.

a. Homopolymers

A homopolymer is defined as a polymer composed of one or two types of repeating monomer units, characterized by a straightforward molecular structure.

**PMDA-ODA for LIG.** Polyimides (PIs) exhibit exceptional suitability for LIG synthesis due to their high carbon content, aromatic structures, and outstanding thermal stability. Kapton, derived from pyromellitic dianhydride (PMDA: $C_{10}H_2O_6$) and 4,4′-oxydianiline (ODA: $C_{12}H_{12}N_2O$), is among the most extensively studied PI for this application. Its robust thermal and chemical properties enable efficient graphitization under laser irradiation, making it a preferred substrate for energy storage, sensing, and flexible electronics applications.[36,70]

**Polyimides other than PMDA-ODA for LIG.** Beyond PMDA-ODA, engineered polyimides with customized molecular backbones have been developed to further optimize the properties of LIG. Fluorinated polyimides, such as 4,4′-(hexafluoroisopropylidene)diphthalic anhydride-4,4′-oxydianiline (6FDA-ODA: $(C_{31}H_{14}F_6N_2O_5)_n$) and 4,4′-(hexafluoroisopropylidene)diphthalic anhydride-2,2′-bis(trifluoromethyl)benzidine (6FDA-TFMB: $(C_{33}H_{12}F_{12}N_2O_4)_n$), incorporate trifluoromethyl groups that facilitate fluorine doping during laser processing.[36] The resulting fluorinated graphene exhibits enhanced hydrophobicity and superior electrochemical properties, making these materials highly effective for biosensors and superhydrophobic surfaces.[36,73] Sulfonated polyimides like 3,3′,4,4′-diphenylsulfonetetracarboxylic dianhydride-4,4′-oxydianiline (DSDA-ODA: $(C_{28}H_{14}N_2O_7S)_n$), containing sulfone groups, yield sulfur-doped graphene with improved conductivity and electrocatalytic activity, which are ideal for electrochemical sensing and energy storage applications.[73] Fig. 6a(I) compares the chemical structures of PMDA-ODA, 6FDA-ODA, and DSDA-ODA, highlighting how different functional groups are introduced to achieve targeted doping effects; Fig. 6a(II) and (III) show Raman spectra collected at different laser fluence values, where the 2D/G ratios of the resulting LIG indicate that doping with fluorine and sulfur significantly enhances graphitic crystallinity at both medium and high laser energies.[73] Additionally, benzimidazole-based co-polyimides, with their rigid aromatic structures, enhance graphitization efficiency, producing graphene with exceptional mechanical flexibility and high capacitance, which are key features for flexible supercapacitors.[74] The molecular architecture of these polyimides significantly influences the morphology, doping characteristics, and conductivity of the resulting graphene, while optimization of laser parameters such as power, speed, and wavelength enable scalable production tailored for specific applications.

**Other homopolymers for LIG.** In addition to polyimides, phenol-formaldehyde (phenolic) resins (PR) synthesized *via* suspension polymerization provide a clean, composition-controllable precursor that can be formed into uniform films.[75] Localized laser heating cleaves the phenol-formaldehyde network into C/H/O fragments that evolve as volatile gases, leaving behind a highly porous, graphitic carbon layer with a large surface area for electrochemical interfaces.[75,76] Adding metal species during resin preparation can further enhance conductivity and the sensing/catalytic response, but the phenolic matrix itself already serves as an efficient simple feedstock for porous LIG-like carbons.[76]

Sulfur-containing polymers provide another versatile platform because the sulfone or sulfide motifs can serve as an intrinsic dopant source during laser conversion. Polyethersulfone (PES) facilitates the simultaneous formation of LIG and metal sulfide–graphene nanocomposites, such as CdS–graphene.[77] The inherent sulfur content of PES enables doping, enhancing the electrocatalytic and photocatalytic properties.[78] This single-step synthesis is highly sensitive for photoelectrochemical detection of metal ions like $Cu^{2+}$ and offers a scalable approach for multifunctional PEC biosensors.[77] Polysulfone-class polymers, including polysulfone (PSU: $(C_{27}H_{22}O_4S)_n$), polyethersulfone (PES: $(C_{12}H_8O_3S)_n$), and polyphenylsulfone (PPSU: $(C_{24}H_{16}O_4S)_n$), also produce sulfur-doped graphene, which demonstrates enhanced electrocatalytic activity, antibacterial properties, and utility in antimicrobial membranes, hydrogen peroxide generation, and flexible electrodes for energy applications.[72] Fig. 6b(I) displays the chemical structures of these three polymers, highlighting their common sulfone backbone, which contributes sulfur during graphitization; the resulting LIG powders exhibit distinct crystallinity, as shown in the XRD patterns in Fig. 6b(II), where peak sharpness and intensity vary with polymer type; Fig. 6b (III) shows the corresponding Raman spectra, confirming successful conversion to graphitic carbon and revealing differences in defect density and $sp^2$ content across the three precursors.[78] These structural and spectral differences reflect how subtle variations in polymer composition affect LIG quality, offering tunable properties for targeted applications.[78]

In addition to these families, several other engineering polymers and resins have been converted into LIG to target specific form factors and operating environments. Polyetherimides (PEIs) have shown promise as substrates for 3D-printed structures, enabling the fabrication of LIG with a low sheet resistance and improved conductivity.[79] These properties make PEI suitable for integrating electronics into complex geometries, particularly in smart devices such as sensors and energy storage systems.[79,80] Additionally, laser-induced graphitization of polybenzimidazole (PBI: $(C_{20}H_{12}N_4)_n$) under controlled conditions produces porous 3D graphene structures with tunable surface areas and enhanced mechanical and chemical stability.[81] PBI-derived LIG membranes demonstrate exceptional performance in organic solvent nanofiltration (OSN), achieving ethanol permeance up to 12.14 LMH/bar and rejection rates exceeding 90% for dyes like Congo red, highlighting their suitability for filtration in harsh chemical environments.[81] Furthermore, polybenzoxazine (poly(Ph-ddm)), a thermosetting resin with a high char yield and chemical resistance, has been converted into graphene through laser scribing, achieving a specific surface area of 883 $m^2\ g^{-1}$ and a low sheet resistance of 35 $\Omega\ sq^{-1}$.[82] Forest-like LIG structures fabricated from poly(Ph-ddm) enhance light absorption to 99.0% across the solar spectrum and

 This journal is © The Royal Society of Chemistry 2026

Open Access Article. Published on 09 February 2026. Downloaded on 5/23/2026 3:06:13 AM.
This article is licensed under a Creative Commons Attribution 3.0 Unported Licence.

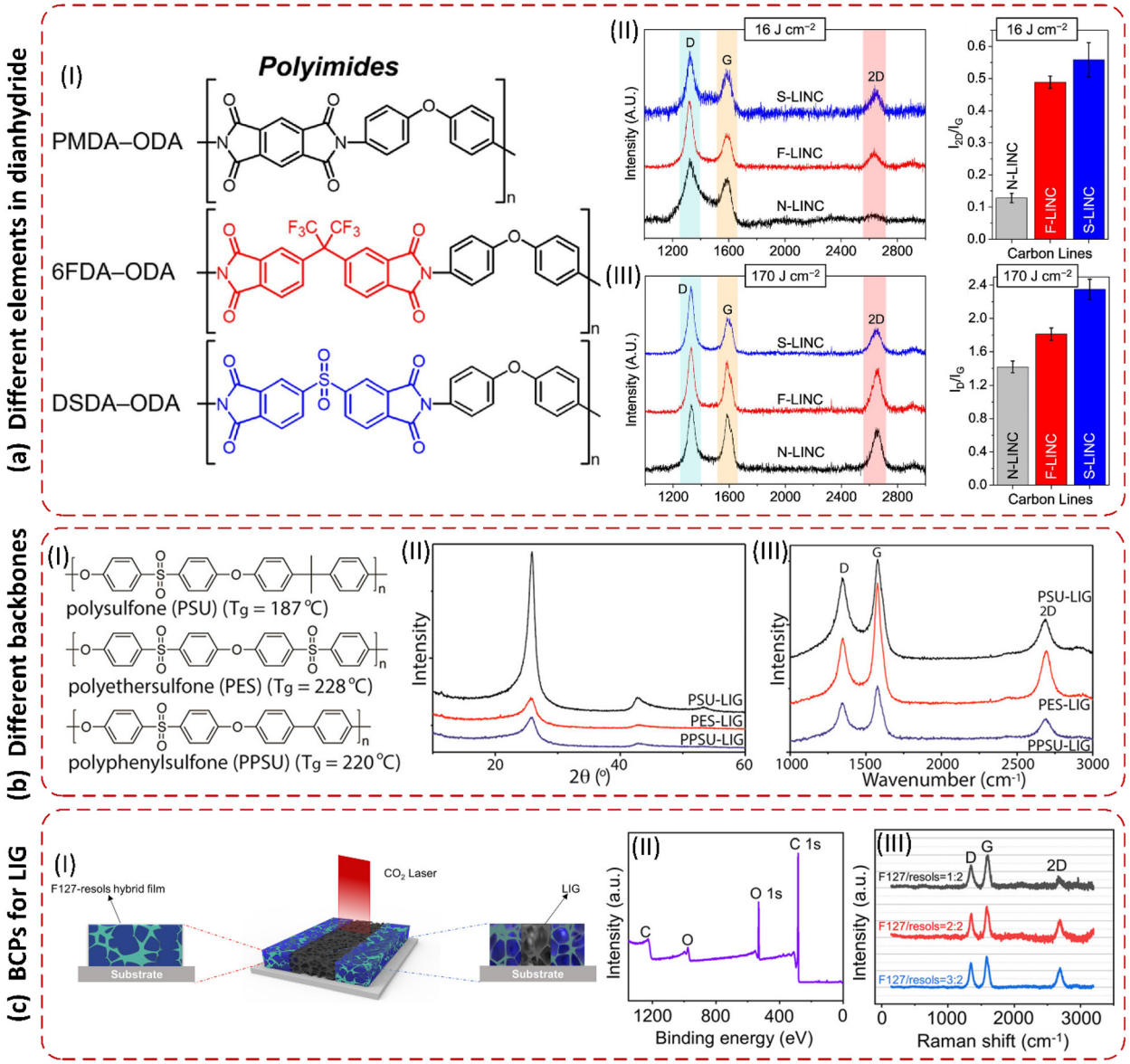


**Fig. 6** Homopolymers and copolymers for LIG. (a) PI modified through incorporating F and S elements into dianhydride. (I) The chemical structure of PMDA-ODA, 6FDA-ODA, and DSDA-ODA. (II) Raman spectra and corresponding 2D/G ratios of carbon lines obtained at a laser fluence of 16 J $cm^{-2}$. (III) Raman spectra and corresponding 2D/G ratios of carbon lines obtained at a laser fluence of 170 J $cm^{-2}$. This figure has been adapted from ref. 73 with permission from Elsevier, copyright 2022. (b) LIG on PSU, PES, and PPSU. (I) Chemical structures of PSU, PES, and PPSU. (II) XRD analysis of PSU-LIG, PES-LIG, and PPSU-LIG powders. (III) Raman spectra of PSU-LIG, PES-LIG, and PPSU-LIG. This figure has been adapted from ref. 78 with permission from American Chemical Society, copyright 2018. (c) LIG on composites of PEO-PPO-PEO BCPS and phenol-formaldehyde resins. (I) Schematic illustration of the transformation of F127/resols into porous LIG. (II) XPS spectra of the resultant LIG. (III) Raman spectra of LIG prepared with varying mass ratios of Pluronic F127 to resols. This figure has been adapted from ref. 84 with permission from American Chemical Society, copyright 2022.

achieve efficient light-to-heat conversion, reaching 90.7 °C under one sun irradiation.[83] These properties highlight the potential of poly(Ph-ddm)-derived LIG for photothermal applications such as solar energy harvesting and desalination.[82,83]

**The prospect of homopolymers.** The development of homopolymers for LIG synthesis presents exciting opportunities for scalable and sustainable graphene production. Advancements in polymer design, such as tailoring molecular structures for enhanced doping and functionality,[60,77] alongside innovations in laser processing technologies,[78] will enable precise control over LIG properties. Sulfur-doped polymers like PES and PSU offer unique advantages for electrocatalytic and antimicrobial applications,[77,78] while improved laser techniques promise highly specialized graphene structures.[79,80] Future research at the intersection of polymer chemistry and laser processing could revolutionize fields such as bioelectronics, energy storage, and environmental sensing, driving innovative solutions for global challenges.

Open Access Article. Published on 09 February 2026. Downloaded on 5/23/2026 3:06:13 AM. This article is licensed under a Creative Commons Attribution 3.0 Unported Licence.

**Summary of the section**. In the literature on LIG grown from homopolymers, various polyimides are the most frequently used precursors, while other studies have also examined materials such as PEI, PBI, and PSU. Overall, LIG growth on these polymers is commonly achieved by direct laser scribing without any pretreatment, and it can typically be performed in air without the need for an inert-gas environment. Most reports rely on a 10.6 μm $CO_2$ laser as the primary source, and the resulting films can reach sheet resistances as low as ≈13 Ω $sq^{-1}$. Similar to other precursor categories, the resulting microstructure is not uniform across studies or process windows, spanning morphologies that range from relatively dense to highly porous. Chemically, the bonding is dominated by C–C, with additional functionalities that depend on the precursor composition and heteroatom retention, including C=C, C–N, C=N, C–O, C–O–H, and O=C–C, as well as signatures associated with fluorine- and sulfur-containing systems (for example, C–F, $CF_2$, C–S, C=S, and oxidized sulfur species such as C–$SO_2$, C–$SO_3$, and C–$SO_4$). Finally, trends in Raman metrics suggest that the maximum 2D/G ratio is often achieved at intermediate laser power; F and S doping can substantially increase 2D/G (for instance, from 0.13 to 0.55), and PBI is notable for producing highly crystalline LIG over a comparatively wide range of laser parameters (all the data are summarized from Table S1).

b. Copolymer

A copolymer is a single polymer chain that contains two or more chemically distinct repeat segments arranged along its backbone. In the context of LIG, we use the term copolymer precursors to emphasize systems in which this intrinsic molecular sequence and/or microphase-separated architecture is the primary design lever that governs laser conversion: by dictating domain morphology, outgassing pathways, and the length scales over which porosity and $sp^2$ reconstruction develop.

**The benefit of using BCPs instead of homopolymers**. Block copolymers (BCPs), one of the most prominent examples of copolymers, have been extensively studied for their ability to self-assemble into well-defined nanostructures and their capacity for precise control over polymer chemical composition and morphology. The intrinsic self-assembly behavior of BCPs facilitates the formation of hierarchically porous materials with tunable pore sizes and distributions, essential for applications requiring high surface areas, such as energy storage, catalysis, and sensing.[84,85] Furthermore, the compositional flexibility of BCPs allows for the incorporation of functional groups, enhancing the chemical and structural properties of the resulting graphene. By varying the polymer blocks or their ratios, researchers can optimize the graphitization process during laser treatment, enabling the development of tailored graphene materials for specific applications.[86] The combination of bottom-up self-assembly and top-down laser writing techniques further enables scalable and reproducible production of graphene architectures with exceptional uniformity, addressing limitations in traditional fabrication methods.[66]

In several representative studies, BCPs are processed together with a carbonizable phenolic resol to form a BCP-templated resin prior to laser writing. From a formulation standpoint, these are indeed two-component polymer mixtures (*i.e.*, 'composites' in a broad sense).[84–86] We discuss them here, however, because the dominant structure-directing mechanism arises from the copolymer: BCP microphase separation defines the nanoscale domain geometry and connectivity, and BCP's selective decomposition during transient laser heating helps generate the hierarchical pore template. The resol primarily serves as a high-char-yield matrix that preserves this templated framework during carbonization/graphitization. Accordingly, these systems are most naturally interpreted through a copolymer (BCP) self-assembly lens, even though they contain an additional resin component.[84–86]

**BCPs for LIG**. The integration of BCPs with phenolic resins (resols) enables hierarchical self-assembly prior to the discovery of LIG fabrication methods.[85] Transient laser heating facilitates the selective decomposition of BCPs while inducing resol thermo-polymerization, forming nanoporous resin frameworks with tunable pore sizes (10–200 nm).[85] Incorporating chemically modified graphene (CMG) as a light-absorbing substrate enhances localized photothermal heating, improving self-assembly efficiency and minimizing substrate damage.[86] This approach enables the formation of highly ordered nanostructures with vertically aligned lamellar and cylindrical domains, eliminating the need for prolonged thermal annealing and offering a scalable route for precise nanostructure fabrication.[68]

Since the discovery of LIG, researchers figured out that laser direct writing of self-assembled BCP–resol mixtures enabled the scalable fabrication of hierarchically porous LIG with tunable properties. Transient laser heating decomposes BCP while inducing resol thermo-polymerization, forming a well-defined porous framework for graphene growth.[84] Fig. 6c (I) shows a schematic of this transformation process using Pluronic F127 and phenol-formaldehyde resols. Pore size and distribution are controlled by the BCP-to-resol ratio, optimizing structural integrity, conductivity, and flexibility. Fig. 6c(II) presents XPS spectra of the resulting LIG, confirming characteristic bonding associated with graphitized carbon; Fig. 6c(III) shows Raman spectra at varying F127-to-resol mass ratios, demonstrating how composition directly affects the defect density and degree of graphitization. This tunable synthesis process enables control over both the microstructure and electrochemical performance, making BCP–resol systems a promising platform for scalable and application-specific LIG fabrication.[84]

**The prospect of BCPs**. Although the precursors demonstrated are often BCP-templated resin formulations rather than neat BCPs, the key tunable handle remains the copolymer architecture and its microphase separation, which dictates the pore template and mesoscale order that are carried into laser-converted carbon. In this sense, these studies are best grouped here as copolymer-enabled LIG formation, where BCP governs morphology/length-scale control and the resol provides the

 This journal is © The Royal Society of Chemistry 2026

Open Access Article. Published on 09 February 2026. Downloaded on 5/23/2026 3:06:13 AM. This article is licensed under a Creative Commons Attribution 3.0 Unported Licence.

carbon yield and framework stabilization.[84–86] Although research in this field remains limited, the distinctive ability of BCPs to generate well-defined, controllable nanostructures suggests substantial room for expanding precursor design rules and accessing new structure–property windows for LIG.

**Summary of the section**. Throughout studies on LIG grown from copolymers, block copolymers (BCPs) are the most commonly investigated precursors within this category. Compared with simpler commercial or single-component polymers, these systems more often benefit from a pretreatment step (such as thermal annealing or laser annealing) to tune the phase structure or stabilize the precursor before laser conversion. Even so, LIG growth on copolymers is typically reported under ambient air conditions, without requiring an inert atmosphere. In terms of laser sources, the literature most frequently employs either a 10.6 μm $CO_2$ laser or a 1064 nm fiber laser. The resulting LIG can achieve sheet resistances down to ≈28 Ω $sq^{-1}$, although the microstructure reported for complex-polymer-derived LIG more commonly tends toward higher porosity. Chemically, the bonding remains dominated by C–C, with additional contributions from oxygen-containing functionalities such as C═C, C–O, C–O–H, and O═C–C. Importantly, because BCP precursors offer a tunable microphase-separated architecture, changing the mixture ratio (and thus the phase morphology) can directly influence both the resulting LIG morphology and its crystallinity (all the data are summarized from Table S1).

B. Multi-component polymer systems

Multi-component polymer systems are materials in which a polymer matrix is combined with one or more additional constituents (such as inorganic/organic fillers, reinforcements, functional additives, or polymer blends) forming a heterogeneous or multiphase structure with properties that can be tailored beyond those of the neat polymer. By tuning the composition, phase morphology, and interfacial interactions, these systems can be engineered to enhance mechanical robustness, thermal stability, chemical resistance, or functional performance for specialized applications.

**The reason for investigating multi-component polymer systems for LIG**. Researchers are increasingly investigating multi-component polymer systems for LIG fabrication due to their superior tunability of chemical composition and physical properties compared to unfilled polymers. By incorporating heteroatoms,[87,88] nanofillers,[71,89,90] structural reinforcements,[72,91] or another polymer[92,93] into a polymer matrix, these materials can be engineered to improve the quality and functionality of LIG. Furthermore, this approach leverages synergies between the polymer matrix and additives, providing a cost-effective and scalable method for achieving advanced material properties beyond the capabilities of unfilled polymers.[94] Four primary strategies (incorporating nanofillers, doping with heteroatoms, modifying polymer matrices, and polymer blends) have been employed to transform PI into high-performance polymers for LIG synthesis.

**Adding nanofillers**. Nanofillers are among the most effective enhancements, significantly improving the structural, chemical, and electrochemical properties of the resulting graphene. Incorporating palladium (Pd) nanoparticles into PI creates methane sensors with remarkable sensitivity (1.1 μA $ppm^{-1}$) and a detection limit as low as 9 ppm due to the uniform nanoparticle distribution within the porous LIG.[90] Platinum (Pt) nanoparticles embedded in LIG enhance the catalytic activity and electron transfer efficiency, enabling the sensitive detection of hydrogen peroxide with an optimized nanoparticle dispersion achieved *via* magnetron sputtering.[95] Bimetallic nanoparticles, such as Pt–Au, further improve the performance by combining the catalytic properties of both metals, enabling dopamine sensors with detection limits of 75 nM.[89] Integrating these composites with flexible substrates like PDMS enhances the mechanical adaptability, enabling wearable and implantable devices.[89]

Beyond noble metals, metal oxide nanocrystals such as $Co_3O_4$, $MoO_2$, and $Fe_3O_4$, formed *in situ* during laser irradiation of metal-complex-containing PI, exhibit exceptional electrocatalytic activity for oxygen reduction reactions.[94] Fig. 7a(I) illustrates the reaction scheme for fabricating metal-complex PI films prior to lasing, while Fig. 7a(II–IV) presents high-resolution TEM images confirming the presence of $Co_3O_4$, $MoO_2$, and $Fe_3O_4$ nanocrystals embedded in the polymer matrix. The electrocatalytic performance of these materials is further validated by the Tafel plots shown in Fig. 7a(V), which demonstrate improved kinetics and current densities for the oxygen reduction reaction (ORR).[94] These results underscore how nanofiller selection and laser processing can be synergistically tuned to enhance the multifunctionality of LIG.

**Heteroatom doping**. Heteroatom doping is another highly effective strategy for enhancing LIG properties. Phosphorus (P) doping *via* ammonium polyphosphate (APP) integration into PI films produces LIG with a specific capacitance of 206 F $g^{-1}$ at 0.025 A $g^{-1}$, significantly surpassing that of undoped LIG.[96] This improvement is attributed to the hierarchical porous structure and enhanced graphitization facilitated by APP, which also imparts flame-retardant properties.[96] Boron (B) doping, achieved using boric acid ($H_3BO_3$) and borax, yields ultrahigh specific capacitance values up to 65.7 mF $cm^{-2}$ with a cycling stability exceeding 50 000 cycles.[97] Fig. 7b(I) illustrates the reaction scheme for fabricating B-doped LIG using $H_3BO_3$; boron doping enhances ionic transport and improves the electrode–electrolyte interface for superior energy storage.[88] SEM images in Fig. 7b(II) and (III) compare the surface morphology of undoped and 8 wt% B-doped LIG, respectively, revealing increased porosity and surface roughness with doping; Fig. 7b(IV) shows the CV curves of LIG-based micro-supercapacitors derived from PI, PAA, and PAA/$H_3BO_3$, highlighting the performance improvement achieved through boron incorporation.[73,88]

**Adding other functional material**. Functional material incorporation into PI has further expanded its potential for LIG synthesis. Activated carbon (AC) particles are embedded into the porous LIG structure using vacuum-assisted infiltration, ensuring uniform distribution and enhanced electro-

Open Access Article. Published on 09 February 2026. Downloaded on 5/23/2026 3:06:13 AM.
This article is licensed under a Creative Commons Attribution 3.0 Unported Licence.

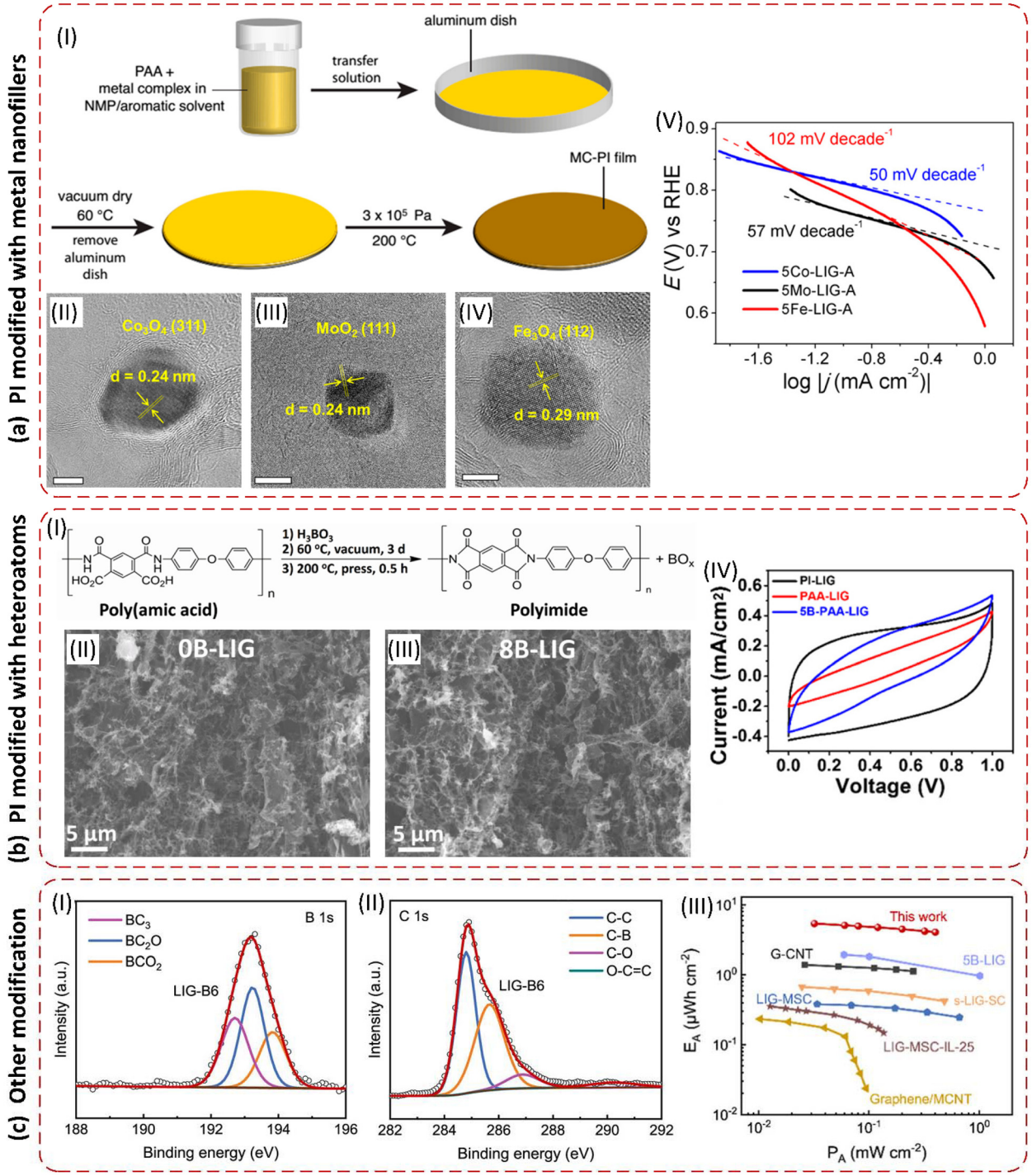


**Fig. 7** Multi-component polymer systems for LIG. (a) PI modified with metal complexes as nanofillers. (I) Reaction scheme of MC-PI film fabrication. (II) High-resolution TEM image of $Co_3O_4$ in LIG. (III) High-resolution TEM image of $MoO_2$ in LIG. (IV) High-resolution TEM image of $Fe_3O_4$ in LIG. (V) Tafel plots for testing the stability and activity of the resultant LIG. This figure has been adapted from ref. 94 with permission from American Chemical Society, copyright 2015. (b) PI modified with $H_3BO_3$ through heteroatom doping. (I) Reaction scheme of B-LIG fabrication. (II) SEM image of no B heteroatoms in LIG. (III) SEM image of 8 wt% B heteroatoms in LIG. (IV) CV curves of micro-supercapacitors from PI-derived LIG, PAA-derived LIG, and PAA/$H_3BO_3$-derived LIG at a scan rate of 0.1 V $s^{-1}$. This figure has been adapted from ref. 88 with permission from American Chemical Society, copyright 2015. (c) PI modified with borax and CMC as a functional material. (I) High-resolution XPS B 1s spectra of LIG-B6 (6 wt% borax solution) electrodes. (II) High-resolution XPS C 1s spectra of LIG-B6 electrodes. (III) Comparison of the areal Ragone plot of the LIG-B6 micro-supercapacitor with other reported micro-supercapacitors. This figure has been adapted from ref. 72 with permission from American Chemical Society, copyright 2021.


This journal is © The Royal Society of Chemistry 2026

Open Access Article. Published on 09 February 2026. Downloaded on 5/23/2026 3:06:13 AM. This article is licensed under a Creative Commons Attribution 3.0 Unported Licence.

chemical characteristics through optimized LIG–AC interactions.[91] Similarly, ionic liquids (ILs) are integrated into PI to produce ionic LIG (i-LIG) *via* a sol–gel process, forming a highly porous, crystalline structure with enhanced ion transport properties.[98] Another method combines PI with PDMS by dispersing PI powder into the PDMS matrix, followed by laser writing to create composite substrates with tunable mechanical and electrical properties.[99] These methods optimize graphitization during laser processing, tailoring LIG for advanced applications.

Additionally, combining borax with carboxymethyl cellulose (CMC) as a binder in PI films enables the scalable production of boron-doped LIG with a tunable capacitance and mechanical flexibility, ideal for flexible micro-supercapacitors.[72] Fig. 7c (I) presents the high-resolution XPS B 1s spectra of the LIG-B6 electrode (6 wt% borax), confirming the successful incorporation of boron species; Fig. 7c(II) shows the corresponding C 1s spectra, indicating the presence of well-defined $sp^2$ carbon bonding structures in the doped LIG. The resulting device demonstrates an enhanced electrochemical performance, as seen in the areal Ragone plot in Fig. 7c(III), which compares the LIG-B6 micro-supercapacitor with other reported systems and highlights its superior energy and power density. This combination of chemical tuning and scalable fabrication makes the borax-CMC strategy a practical route for high-performance LIG-based energy storage.[72]

**Polymer blends**: polymer blends (polymer–polymer alloys) offer a distinct route to tune LIG formation without introducing inorganic fillers, by simultaneously adjusting the char yield/thermal stability and controlling the phase morphology prior to laser exposure. Lawan *et al.*[92] improved polybenzoxazine-based LIG by alloying a thermosetting polybenzoxazine (poly(Ph-dde)) with polyimide, where increasing the PI content raised the thermal stability and char residue, as well as increasing the substrate toughness by around 4 times, enabling more robust carbonization during scribing. Compared with neat polybenzoxazine, the 50/50 alloy yielded LIG with a lower sheet resistance (17.67 ± 1.8 Ω $sq^{-1}$ *vs.* 28.08 ± 1.2 Ω $sq^{-1}$) and larger in-plane crystallite size, consistent with reduced disorder and improved structural integrity. Using response-surface optimization on the 50/50 alloy, they further identified laser settings that produced LIG with a minimum sheet resistance of 3.61 Ω $sq^{-1}$, multilayer Raman features, and a sponge-like porous morphology under ambient conditions.[92] In a complementary 'selective-conversion' strategy, Yazdi *et al.*[93] used immiscible PC/PEI blends in which the PEI phase selectively graphitized under 10.6 μm $CO_2$ laser scribing (6 W, 2 cm $s^{-1}$; pulse duration = 14 μs), transforming phase-separated PEI domains into columnar porous LIG embedded within the PC matrix. By varying the starting PEI volume fraction, the resulting PC–LIG nanocomposites achieved exceptionally high bulk conductivities (26–400 S $m^{-1}$), highlighting polymer blends as a way to engineer percolating graphene networks *in situ* while retaining the processing advantages of the non-converting matrix polymer.[93]

**Modifying other polymers**. Modifying polymer precursors provides an effective route to extend LIG formation beyond PI by tailoring absorption, carbonization pathways, and heteroatom incorporation. Analogous to doped PI systems, polybenzimidazole (PBI) can be treated with $H_3PO_4$ to promote microporosity and ion transport during laser conversion.[100] As a result, phosphoric acid (PA)-doped PBI processed by LIG achieves a tunable specific surface area of up to 384.46 $m^2$ $g^{-1}$, along with an areal capacitance of 149 mF $cm^{-2}$ and an energy density of 20.7 μWh $cm^{-2}$. Mechanistically, PA is proposed to initiate radical reactions, facilitate micropore development, and improve ion transfer, collectively enhancing the electrochemical performance of PBI-derived LIG.[100]

A second class of strategies relies on composite formulation and additives that improve film formation, thermal robustness, or mesoscale pore organization before laser irradiation. Chitosan-borax incorporates sodium tetraborate decahydrate (borax) as a cross-linker, enhancing the thermal and mechanical stability to produce LIG with a sheet resistance of 110 Ω $sq^{-1}$ under $CO_2$ laser irradiation.[101] Phenolic resin (PR) combined with polyvinyl alcohol (PVA) forms uniform films through ethanol dissolution, yielding consistent and conductive graphene upon $CO_2$ laser ablation.[102] Phloroglucinol–glyoxylic acid phenolic resin combined with Pluronic F127 surfactant enables the self-assembly of mesoporous graphene with precise pore control during laser irradiation.[103]

Chemical functionalization of established engineered polymers further expands the accessible structures and device functions. Sulfonated poly(ether ether ketone) (SPEEK) is synthesized by sulfonating PEEK in concentrated sulfuric acid, precipitating it in cold deionized water, and drying the resulting polymer.[87] Pulsed $CO_2$ laser treatment of SPEEK films produces a foam-like 3D graphene structure with high crystallinity and achieves a specific capacitance of 18 mF $cm^{-2}$ at a scan rate of 3 mV $s^{-1}$ in a 2 V potential window, demonstrating its effectiveness for flexible supercapacitor applications.[87] In a study by Liu *et al.*,[104] poly(*m*-phenylene isophthalamide) (PMIA: $(C_{14}H_{10}N_2O_2)_n$) modified with potassium permanganate ($KMnO_4$) was used to produce multi-layer graphene-like carbon (MLIGC). $KMnO_4$ promotes deeper carbonization, disperses manganese oxide nanoparticles, and enhances the surface reactivity, enabling higher yields and improved electrochemical performance. The resulting MLIGC achieves up to 25 times higher capacity than that of unmodified PMIA, with reduced impedance and excellent cycling stability, highlighting the importance of modifying commercial substrates like PMIA to overcome surface stability and enhance carbonization.[104]

Finally, targeted dopant sources and auxiliary processing aids enable LIG formation from resins and even low-absorption commodity plastics. Epoxy resin (EP) combined with APP has also been utilized to produce N/P co-doped laser-induced graphene (LIG-APP/EP) through a straightforward laser direct-scribing process. The resulting LIG-APP/EP exhibits a hierarchical porous architecture and achieves an initial discharge capacity of 1452 mAh $g^{-1}$ and a coulombic efficiency of 67.2%, making it a promising candidate for lithium-ion battery anodes and sustainable recycling applications.[105,106] Silicone-assisted direct laser writing (SA-DLW) was recently applied to

Open Access Article. Published on 09 February 2026. Downloaded on 5/23/2026 3:06:13 AM.
This article is licensed under a Creative Commons Attribution 3.0 Unported Licence.

polyolefin waste, including polyethylene (PE) and polypropylene (PP), enabling their conversion into porous graphene with a sheet resistance of 76.2 Ω $sq^{-1}$. This process not only retards ablation but also supplies additional carbon atoms, yielding high-quality LIG with a conversion efficiency of 38.3%.[107]

**The prospect of multi-component polymer systems**. The future of multi-component polymer systems for LIG lies in developing multi-functional materials and refining fabrication processes for enhanced scalability and performance. Combining nanofillers, heteroatom dopants, and structural modifiers within a single matrix could simultaneously optimize electrical conductivity, mechanical flexibility, and chemical functionality.[101] Advances in automated laser systems with precise parameter control could improve uniformity and reduce interface resistance, overcoming current limitations like imperfect current collection.[87] Furthermore, using renewable polymers such as chitosan and phenolic resins provides a sustainable pathway for LIG production.[102] Research into hybrid materials, including 2D transition metal carbides (MXenes) and organic–inorganic frameworks, may unlock new functionalities, extending LIG's applications in energy storage, sensing, and wearable electronics. These innovations will require a collaborative approach that integrates material design, process optimization, and device engineering to realize the full potential of LIG-based multi-component polymer systems.

**Summary of the section**. In the literature on multi-component polymer systems, polyimides still serve as the most common polymer matrix for LIG growth, although many other matrices have also been explored, including PMIA, phenolic resins (PRs), and PEEK. Similar to many homopolymer systems, laser scribing on multi-component polymers is generally reported as a direct process that does not require pretreatment, and LIG formation is typically achievable in air without the need for an inert atmosphere. A 10.6 μm $CO_2$ laser remains the predominant source throughout these studies. Notably, multi-component polymers in this category can yield a particularly low sheet resistance, reaching values as low as ≈5 Ω $sq^{-1}$, but the resulting morphology is still highly variable across formulations and processing windows, ranging from relatively dense to highly porous structures. From a chemical standpoint, the bonding is dominated by C–C with additional signatures that reflect heteroatom incorporation and filler chemistry, including C═C, C–N, C═N, C–O, C–O–H, and O═C–C, as well as functionalities associated with F- and S-containing systems (*e.g.*, C–F, $CF_2$, C–S, C═S, and oxidized sulfur species such as C–$SO_2$, C–$SO_3$, and C–$SO_4$). In composites that introduce phosphorus- or boron-containing constituents, additional bonding environments such as C–P and P–O, as well as C–B-related motifs (*e.g.*, $BC_3$, $BC_2O$, and $BCO_2$) have been reported. Raman metrics also vary widely across multi-component polymers, indicating that defect density and graphitic ordering are strongly precursor-dependent; in particular, incorporating F and S into PI-based systems can improve the 2D/G ratio, whereas boron incorporation does not appear to provide a similarly consistent benefit in this regard (all the data are summarized from Table S1).

**2.3.2. Natural derivatives.** A natural derivative-based single-layer carbon precursor is a material derived from substances originally sourced from nature, such as plants, animals, or minerals, which has been chemically modified or processed while retaining some characteristics of the natural source. Natural derivatives can be classified as bio-based materials and fossil-based products.

I. Bio-based materials

Bio-based precursors ('green LIG') have attracted growing attention because they are renewable, widely available, and can reduce the dependence on fossil-derived polymers while still enabling direct laser patterning of conductive carbon networks.[43,45] Bio-based precursors for LIG can generally be grouped into lignocellulosic substrates (wood/leaves/cork/paper, where lignin *vs.* cellulose content strongly affects laser carbonization) and other bio-derived polymers (polysaccharides, proteins, and bio-derived resins/sugars that can be processed as films/inks/prints).

A. Lignocellulosic substrates

Lignocellulosic substrates are plant-derived solids primarily composed of cellulose/hemicellulose (oxygen-rich polysaccharides) and lignin (an aromatic, char-forming biopolymer). Because laser heating simultaneously drives pyrolysis and oxidation, the local lignin-to-cellulose balance strongly governs carbon yield, burning susceptibility, and graphitization efficiency during LIG formation.[43] In practice, many lignin-rich solids can be patterned directly, whereas cellulose-rich paper often benefits from flame-retardant pretreatments that suppress combustion and stabilize carbonization.[48,108]

**Lignin-rich natural solids (wood, leaves, cork)**. Natural lignin-containing solids such as wood, leaves, cork, and biomass skins/shells have been widely demonstrated as direct, low-cost substrates for LIG, often requiring minimal preprocessing. Using ultrafast laser pulses, Le *et al.*[109] showed that wood and leaves could be directly converted into porous graphene in a one-step process under ambient conditions, highlighting the ability of natural lignocellulose to support laser-driven carbonization and graphitization. Because lignin is aromatic and char-forming, a higher lignin content generally favors improved LIG formation and conductivity. Transition-metal salt impregnation further broadens functionality: cedar wood doped with Cu, Co, Ni, Fe, and NiFe yields LIG with enhanced electrocatalytic activity relevant to energy conversion and storage.[110] Cork, rich in lignin and suberin, can similarly be laser-carbonized into robust porous graphene layers suitable for flexible devices.[111] Fallen leaves provide an additional structural advantage because embedded biominerals can act as natural templates during laser processing, producing mesoporous graphene with a low sheet resistance and strong cycling stability.[112] Extending this 'biomass shells' category to agricultural by-products, Steksova *et al.*[113] leveraged waste almond shells (a lignin-rich nutshell biomass) as a minimally processed filler and cast it with a chitosan-based matrix into flexible biocomposite films that served as both the substrate and precursor for IR/UV laser scribing.

Beyond single-pass scribing, multiple-lasing strategies can further improve graphitization by converting intermediate

 This journal is © The Royal Society of Chemistry 2026

Open Access Article. Published on 09 February 2026. Downloaded on 5/23/2026 3:06:13 AM. This article is licensed under a Creative Commons Attribution 3.0 Unported Licence.

amorphous carbon into few-layer graphene. This effect has been demonstrated on abundant, biodegradable biomass such as coconut shells and potato skins.[33] As an illustrative lignocellulosic example (Fig. 8a), a dual-lasing approach enables on-substrate fabrication of a coconut-shell micro-supercapacitor with improved Raman signatures and electrochemical behavior relative to a single-lased reference.[33] Pine wood is another representative lignocellulosic solid that can form high-quality, hierarchically porous LIG under $CO_2$ laser scribing, underscoring the adaptability of natural substrates for scalable 'green' graphene manufacturing.[114]

**Why lignin-rich solids graphitize readily**. A recurring mechanistic theme is that lignin (an amorphous, highly branched polymer connected by ether and C–C bonds) provides aromatic motifs and a higher char yield that promote carbon retention and $sp^2$ enrichment during rapid laser heating.[115] Studies that isolate or emphasize lignin as the main carbon source show that lignin can be transformed into porous graphene-like networks by direct laser writing, supporting its role as a key enabler of LIG formation in many natural solids.[115,116] Blending/processing strategies can further tune carbonization behavior. For example, lignin-containing formulations (including lignin/PVA/urea systems) have been reported to yield laser-scribed graphene electrodes suitable for biochemical sensing.[117] Complementary computational efforts have also been used to rationalize lignin-to-LIG conversion pathways and the species evolved during irradiation, providing a mechanistic bridge between composition and final LIG structure/performance (Fig. 8b).[118]

**Cellulose-rich paper and paper-derived substrates**. Paper offers a convenient, abundant, and low-cost platform for laser patterning, but its cellulose-rich composition can increase oxygen-driven mass loss and combustion during lasing unless conditions are appropriately controlled. A notable advantage is that paper can be integrated directly into analytical and sensing formats; for instance, single-step laser scribing has been used to fabricate electrochemical paper-based analytical devices without any pretreatments.[119] Relatedly, Kulyk *et al.*[120] showed that paper-LIG could be produced in a single in-focus irradiation step by reducing scan-line separation to ensure overlap of adjacent beam paths, which effectively reproduced multi-step conversion while improving throughput (though excessive energy input could still compromise fiber integrity). In many cases, fire-retardant pretreatments are used to enable stable carbonization and suppress burning. $NH_4H_2PO_4$ pretreatment, for example, has been used to enable the one-step direct laser writing carbonization of cellulose paper and subsequent fabrication of force sensors.[121] Other phosphate-based fire-retardant strategies have also been reported, including UV-driven LIG formation on paper for humidity/temperature sensing and paper-based LIG for mechanical sensing.[108,122] Paper performance can also be tuned *via* functional inks and additives: soaking copy paper in gelatin-mediated inks containing molybdenum ions followed by $CO_2$ laser scribing produces molybdenum carbide–graphene composites that enable foldable paper electronics.[123] Additionally, the modification of paper with sodium borate and wax has been shown to facilitate laser-induced graphitization and improve the electrochemical characteristics of paper-based electrodes (Fig. 8c).[124]

B. Other bio-derived polymers

Beyond intact lignocellulosic solids, many bio-based precursors used for LIG are better described as isolated biopolymers (*e.g.*, polysaccharides and proteins) or bio-derived resins/sugars that could be processed into films, inks, coatings, or printed forms prior to lasing. Compared with natural lignocellulosic substrates, these systems offer greater control over precursor chemistry (functional groups, heteroatom content, viscosity/printability, additive incorporation), enabling engineered pathways to porosity, conductivity, and application-specific performance.

**Polysaccharides (chitosan derivatives)**. Chitosan-based materials (such as carboxymethyl chitosan (CMCS), chitosan oligosaccharide (COS), and chitosan hydrochloride (CSHC)) are demonstrated to be effective LIG precursors. Their abundant hydroxyl, carboxyl, and amino groups can support carbonization while simultaneously enabling heteroatom incorporation.[125] Direct $CO_2$ laser engraving of these chitosan derivatives produces hierarchically porous, mechanically stable conductive LIG suitable for scalable device fabrication.[126,127] Beyond chitosan, Kulyk *et al.*[120] also demonstrated that solvent-cast carboxymethyl xylan films (a hemicellulose-derived polysaccharide) could be converted into porous LIG *via* a two-step irradiation (defocused then in-focus), yielding conductive patterns (sheet resistance $\approx$186 $\Omega$ $sq^{-1}$) that were further used to build a simple, low-cost temperature sensor. More recently, Sankaran *et al.*[128] showed that corn-starch bioplastic could be converted into a magnetic LIG nanocomposite *via* $Fe(NO_3)_3$-assisted laser-induced pyrolysis, requiring a minimum $Fe(NO_3)_3$ concentration threshold for reproducible LIG formation and yielding soft-magnetic behavior ($M_s$ $\approx$67 emu $g^{-1}$; $H_c$ $\approx$200 Oe) associated with iron-containing phases ($\gamma$-$Fe_2O_3$ and $Fe_3C$), while the starch-based substrates remained readily soil-degradable (>80% weight loss after 12 days).

**Bio-derived resins and sugars (furfuryl alcohol, sucrose)**. Bio-derived thermosetting/carbonizable resins and sugar-based formulations provide another route to LIG and porous graphene architectures. Poly(furfuryl alcohol) (PFA), when combined with graphene oxide (GO), can overcome carbonization challenges under laser irradiation and yield conductive traces with strong areal capacitance relevant to micro-supercapacitors.[129] Sugar-based systems can also be engineered for highly porous graphene structures: sucrose mixed with nickel powders and processed *via* 3D printing serves as both the carbon source and catalyst/template system, producing free-standing graphene foams with high conductivity and ultralight density.[130]

**Proteins (silk)**. Silk fibroin is a naturally occurring protein with intrinsic nitrogen-containing functional groups and aromatic residues, enabling the direct formation of N-doped graphene-like networks under laser irradiation. Laser-induced graphene fabrics prepared from silk have been demonstrated

Open Access Article. Published on 09 February 2026. Downloaded on 5/23/2026 3:06:13 AM.
This article is licensed under a Creative Commons Attribution 3.0 Unported Licence.

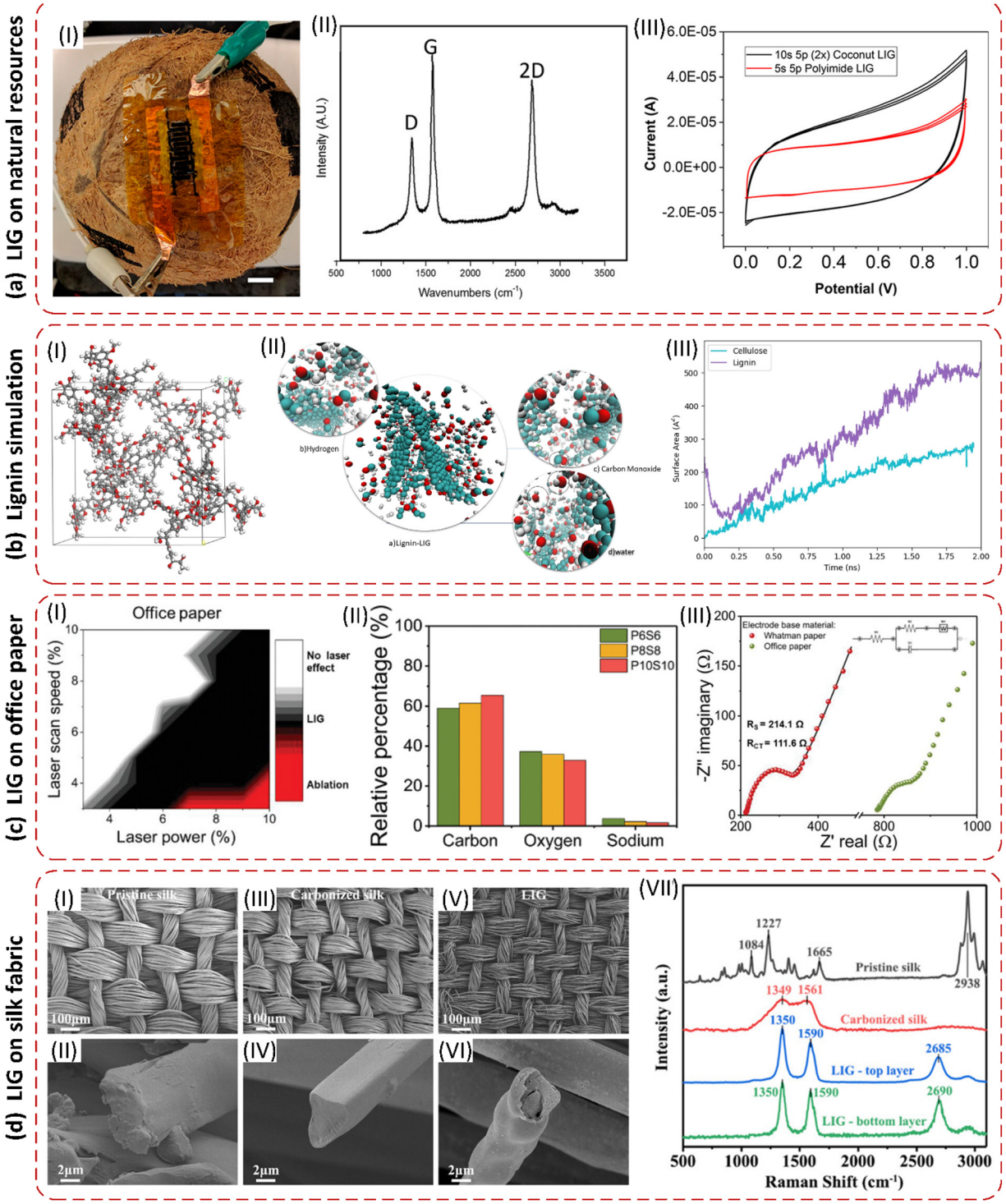


**Fig. 8** Bio-based material for LIG. (a) LIG grown on lignin-rich natural solids. (I) LIG-based supercapacitor fabricated on coconut. (II) Raman spectrum of coconut-derived LIG lased twice (10% speed and 5% power). (III) CV curves of a twice-lased coconut micro-supercapacitor compared with a single-lased polyimide at a scan rate of 10 mV $s^{-1}$. This figure has been adapted from ref. 33 with permission from American Chemical Society, copyright 2018. (b) Simulation of LIG on lignin. (I) Lignin simulation box. (II) Visualization of simulation and gasses evolved during the process. (III) Calculated surface area of LIG from lignin and cellulose. This figure has been adapted from ref. 118 with permission from Springer Nature, copyright 2024. (c) LIG grown on paper. (I) Heat maps of the laser irradiation effect on office paper. (II) Relative element composition of LIG on office paper. (III) Nyquist plots of chromatography paper and office paper to interpret EIS data. This figure has been adapted from ref. 124 with permission from John Wiley and Sons, copyright 2021. (d) LIG grown on silk fabric. (I) SEM image of the fabric structure of pristine silk. (II) SEM image of a single fiber of pristine silk. (III) SEM image of the fabric structure of carbonized silk. (IV) SEM image of a single fiber of carbonized silk. (V) SEM image of the fabric structure of LIG. (VI) SEM image of a single fiber of LIG. (VII) Raman spectra of pristine silk, carbonized silk, and LIG. This figure has been adapted from ref. 131 with permission from John Wiley and Sons, copyright 2021.


This journal is © The Royal Society of Chemistry 2026

Open Access Article. Published on 09 February 2026. Downloaded on 5/23/2026 3:06:13 AM. This article is licensed under a Creative Commons Attribution 3.0 Unported Licence.

for flexible sensing applications, leveraging the combined conductivity, flexibility, and porous architecture of protein-derived LIG.[131] As a representative example of protein-derived LIG (Fig. 8d), SEM/Raman characterization studies capture the microstructural evolution from pristine silk to carbonized/laser-graphitized states and provide insights into how laser parameters influence porosity and graphitization.[131] Recent work has further improved silk-based LIG electrodes using a two-step route (thermal pretreatment followed by $CO_2$-pulsed laser irradiation), achieving low sheet resistance while maintaining mechanical integrity and adding robust adhesion and antibacterial properties for long-term electrophysiological monitoring.[132]

**The prospect of bio-based materials**. The future of bio-based materials for LIG synthesis lies in advancing sustainable and eco-friendly technologies by leveraging the unique properties of natural precursors like cellulose, lignin, and chitosan. Incorporating multifunctional additives or dopants can enhance LIG's electrical conductivity, structural stability, and electrochemical performance.[45] Scaling up production through optimized laser systems with precise parameter control can ensure uniform porosity and conductivity, while computational simulations provide insights into reaction mechanisms and carbonization pathways.[116,118] The exploration of renewable, biodegradable substrates, including agricultural residues and waste-derived biopolymers, aligns with global sustainability goals and reduces reliance on fossil-based resources.[44] Furthermore, automation techniques like roll-to-roll manufacturing and 3D printing will facilitate large-scale production, reducing costs while maintaining quality.[43,130]

**Summary of the section**. The literature on LIG grown from bio-based materials demonstrates that a wide range of natural resources and natural-derived products such as paper can serve as viable carbon precursors. In many lignin-containing substrates, laser scribing is often performed directly without pretreatment; however, cellulose-based paper commonly requires pretreatment with a fire-retardant additive to enable stable conversion and suppress combustion during lasing. Processing atmospheres are also more substrate-dependent in this category than for most synthetic polymers: while some bio-based materials can be scribed in air, other systems require controlled environments such as $H_2$, $N_2$, or Ar to achieve consistent LIG formation. With respect to laser sources, 10.6 μm $CO_2$ lasers (including pulsed $CO_2$ variants) are used most frequently, although alternative sources (such as 346 nm fiber lasers and 355 nm Nd:$YVO_4$ lasers) have also been reported. Electrical performance can be excellent, with the sheet resistance reaching as low as ≈2.8 Ω $sq^{-1}$; the resulting LIG microstructure is often described as predominantly porous. Chemically, the bonding is dominated by C–C, with additional contributions from functionalities including C=C, C–N, C=N, C–O, C–O–H, and O=C–C, along with sulfur-related bonds (*e.g.*, C–S and C–$SO_x$) in systems where sulfur-containing components are present. Finally, for paper substrates treated with fire retardants, multiple lasing passes are often needed to produce a clearly developed 2D Raman peak, suggesting that repeated irradiation plays an important role in driving the conversion toward more graphitic carbon in these formulations (all the data are summarized from Table S1).

II. Fossil-based products

A fossil-based product refers to a material or product derived from non-renewable fossil resources, such as petroleum, coal, or natural gas, formed over millions of years from the remains of ancient organisms.

**Graphite oxide for LIG**. Graphite, a fossil-based product derived from the carbonization of ancient organic matter, has long been a cornerstone material for graphene synthesis. Its naturally occurring layered structure, composed of $sp^2$ hybridized carbon atoms, makes it an ideal precursor for producing graphene-related materials. Through chemical oxidation, graphite can be converted into graphite oxide (GO), introducing oxygen-containing functional groups like hydroxyl and epoxy. These groups increase interlayer spacing, disrupting the carbon lattice and making GO dispersible and reactive.[133] Laser irradiation further enables the thermal reduction of GO, restoring $sp^2$ hybridization by removing oxygen groups and yielding conductive graphene. Studies by Trusovas *et al.*[134] and Sokolov *et al.*[135] demonstrated how laser parameters such as power, wavelength, and atmosphere influenced the defect density and material quality, with optimized conditions producing high-quality graphene with superior electrical properties. These advancements paved the way for the development of laser-induced graphene (LIG) technologies.

**Coal, tar, and pitch for LIG**. After the idea of LIG was first proposed in 2014, researchers investigated certain fossil-based products as ideal LIG carbon precursors, including coal, petroleum pitch, and tar, due to their abundant availability and high carbon content. Coal, processed through $CO_2$ laser irradiation, undergoes photothermal decomposition to produce laser-scribed graphene (C-LSG) with enhanced conductivity (12 Ω $sq^{-1}$) and multifunctional properties, enabling applications in Joule heating, dopamine sensing, and energy storage, while the incorporation of FeNi hydroxides further improves its catalytic performance for oxygen evolution reactions.[136] Apart from that, different types of coal, such as anthracite, bituminous, and lignite, demonstrate tunable electronic and magnetic properties when processed with $CO_2$ laser annealing. Bituminous coal, in particular, exhibits an optimal combination of maturity and aromatic content, resulting in effective graphitization and nitrogen doping.[137] As shown in Fig. 9a, the typical molecular representations of bituminous coal feature complex aromatic structures that contribute to its suitability for laser conversion. SEM images reveal the formation of interconnected porous networks after laser annealing, while Raman spectra confirm the high degree of graphitization achieved, as indicated by the pronounced G and 2D peaks with reduced D-band intensity. These characteristics contribute to a low sheet resistance of approximately 30 Ω $sq^{-1}$ and enable the production of high-performance functional devices, including magnetic soft actuators, due to the material's enhanced electronic and magnetic properties.[137]

Open Access Article. Published on 09 February 2026. Downloaded on 5/23/2026 3:06:13 AM.
This article is licensed under a Creative Commons Attribution 3.0 Unported Licence.

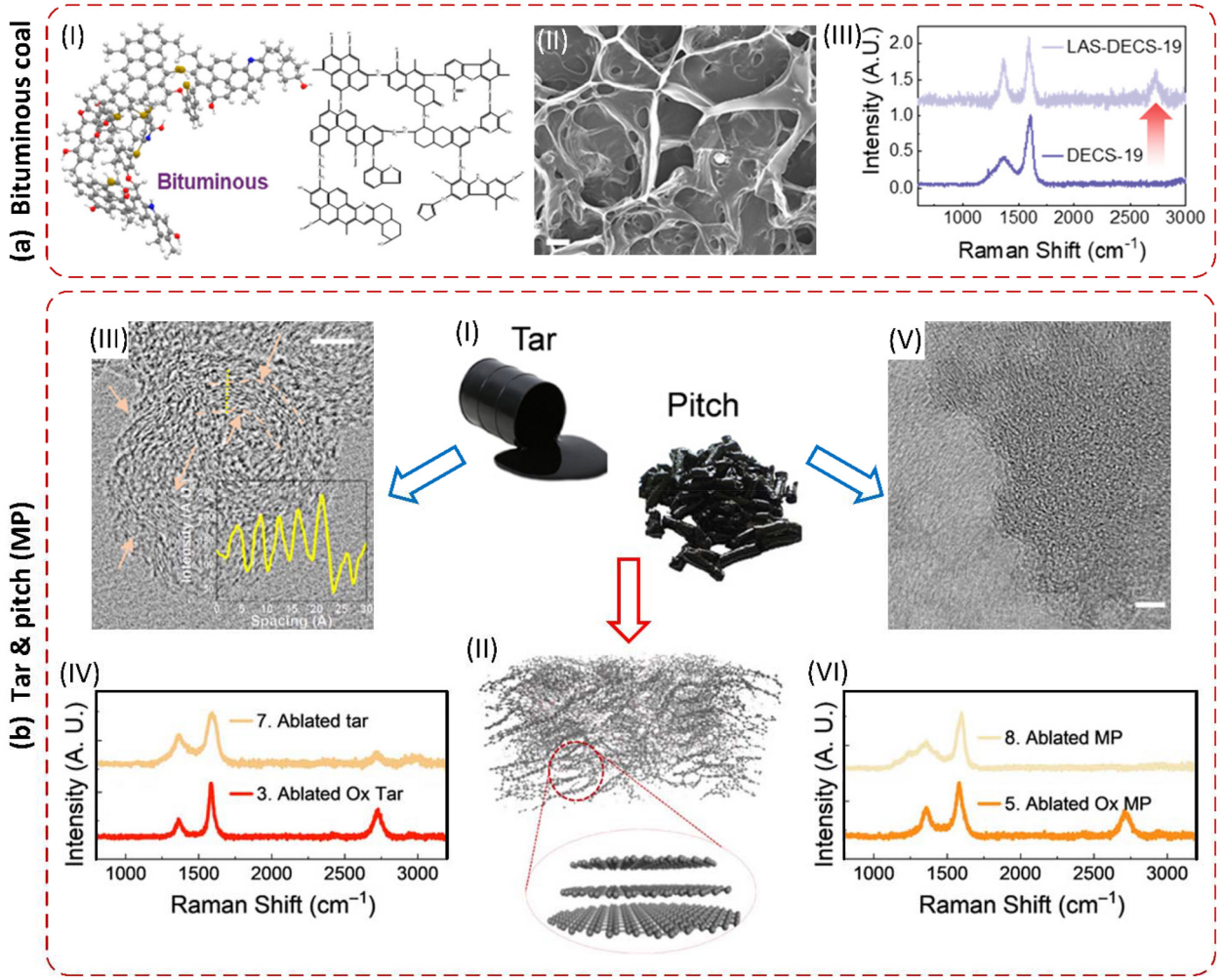


**Fig. 9** Fossil-based product for LIG. (a) LIG grown on bituminous coal. (I) Typical molecular representations of bituminous coal. (II) SEM image of laser-annealed bituminous coal. (III) Raman spectra of bituminous coal. This figure has been adapted from ref. 137 with permission from American Chemical Society, copyright 2022. (b) LIG grown on tar and pitch. (I) Images of tar and pitch. (II) Laser-ablated stochastic graphitic system. (III) TEM image of laser-ablated steam cracked tar. (IV) Raman spectra of ablated tar and ablated ox tar. (V) TEM image of laser-ablated MP pitch. (VI) Raman spectra of ablated MP pitch and ablated ox MP pitch. This figure has been adapted from ref. 138 with permission from The American Association for the Advancement of Science, copyright 2020.

Similarly, petroleum pitch and tar are versatile precursors for LIG, with their graphitization efficiency influenced by hydrogen-to-carbon ratios and aromatic content.[138] Fig. 9b(I) shows the raw forms of tar and mesophase (MP) pitch, both rich in carbon. Upon laser ablation, they form stochastic graphitic structures with disordered but conductive networks, as seen in Fig. 9b(II). TEM imaging of laser-treated steam-cracked tar (Fig. 9b(III)) reveals partially ordered graphene layers. Raman spectra (Fig. 9b(IV)) show that oxidation significantly enhances graphitization, with oxidized tar exhibiting stronger G and 2D peaks. A similar trend is observed in MP pitch: Fig. 9b(V) shows nanostructured carbon formed after lasing, and Fig. 9b(VI) confirms that its oxidized form achieves higher crystallinity. These findings demonstrate that oxidation pretreatment improves structural ordering and conductivity in LIG derived from fossil-based precursors.[138]

**Summary of the section.** Published studies have demonstrated LIG growth from several fossil-based products, with coal, tar, and mesophase (MP) pitch emerging as the most commonly used precursors in this category. In most reports, these materials are converted by direct laser scribing without any pretreatment, and LIG formation is typically achieved in air without the need for an inert atmosphere. Researchers have employed a wider range of laser sources than is typical for many polymer-based systems, including 10.6 μm $CO_2$ lasers, 1064 nm picosecond lasers, and 532 nm Nd:YAG sources. The resulting LIG exhibits a strong electrical performance, with the sheet resistance reported to be as low as ≈5 Ω sq$^{-1}$, while the observed morphology remains highly variable across studies, spanning structures that range from relatively dense to distinctly porous. Chemically, the bonding is dominated by C–C with additional contributions from functional groups such as


This journal is © The Royal Society of Chemistry 2026

Open Access Article. Published on 09 February 2026. Downloaded on 5/23/2026 3:06:13 AM.
This article is licensed under a Creative Commons Attribution 3.0 Unported Licence.

C=C, C–N, C=N, C–O, C–O–H, and O=C–C. Finally, for tar and MP pitch in particular, oxidation is often required to obtain LIG with higher crystallinity, indicating that controlled pre-oxidation can play an important role in promoting more ordered graphitic domains in these fossil-derived precursors (all the data are summarized from Table S1).

### 2.4. Multilayer

A multilayer carbon precursor derives its value from the combined effects of the bulk carbon precursor and additional coatings or layers. These added layers modify or enhance the material's properties, such as its reactivity, stability, or conductivity. The interplay between the bulk precursor and these layers is essential for achieving the desired functionality, making this classification ideal for specialized and high-performance requirements. Multilayer carbon precursors can be classified as synthetic polymers and natural derivatives.

**2.4.1. Stacked layers.** Stacked layers refer to a sandwich-like structure where multiple layers, each with similar thicknesses, are combined to form a cohesive unit. This configuration enhances the material's properties by leveraging the interplay between layers, offering uniformity and scalability for advanced applications.

**Different stacked layer substrates for LIG.** Stacked-layer configurations have been extensively studied to enhance the performance and versatility of LIG-based devices. Wang *et al.*[139] demonstrated the fabrication of high-performance multilayer supercapacitors using femtosecond laser direct writing on PI sheets. By stacking multiple layers of laser-carbonized PI, they achieved a significantly improved specific capacitance, reaching up to 42.6 mF $cm^{-2}$ for a three-layer structure, due to enhanced porosity and nitrogen/oxygen doping. Similarly, Li *et al.*[140] integrated $MnO_2$ into LIG through a combination of laser scribing and electrodeposition, creating stacked pseudocapacitive micro-supercapacitors. This approach resulted in devices with a high energy density and excellent ion transport properties, demonstrating the advantages of synergistic layer interactions.[140] Additionally, laminated structures were explored to encapsulate and protect LIG layers from mechanical degradation, thereby enhancing durability and stability under operational stresses.[141]

Layer-by-layer (LBL) assembly further expands the stacked-layer design by enabling the precise integration of functional nanomaterials and biomolecules on LIG. For instance, MXene/LIG hybrids have been constructed for dopamine biosensing, where MXene layers increase the conductivity and electrochemically active surface area, and alternating deposition allows for the controlled incorporation of recognition elements.[142] Fig. 10a shows a schematic illustration of this LBL synthesis process for constructing the L-$Ti_3C_2$-G bio-electrode, where MXene and glucose oxidase are assembled in alternating layers on the LIG substrate; Fig. 10b presents the cyclic voltammetry (CV) curves comparing the L-$Ti_3C_2$-G electrode with control electrodes, clearly demonstrating an enhanced current response and sensitivity in the presence of 1 mM dopamine in pH 7 PBS at 20 mV.[142] Collectively, these studies highlight the potential of stacked-layer designs for improving the functionality and scalability of LIG-based materials and devices.

**2.4.2. Substrates with coatings.** A substrate with a coating refers to a base material that is covered with a thin layer of another substance to modify its properties or enhance its functionality. In the context of LIG fabrication, coating a substrate with specific precursor materials enables controlled doping, structural modifications, and functional enhancements in the resulting graphene. As illustrated in Fig. 11, the integration of various precursor coatings onto substrates either after (Fig. 11(a)) or before (Fig. 11(b)) laser processing has enabled the development of advanced LIG composites with tailored properties. By leveraging the coating method, researchers have successfully introduced heteroatoms, metal nanoparticles, and functional materials into LIG, enhancing its performance for energy storage, sensing, and flexible electronics. Recent studies have demonstrated how different coatings (ranging from MXene and ZnO to phenolic resin and Prussian blue) interact with laser parameters to produce high-performance graphene structures.

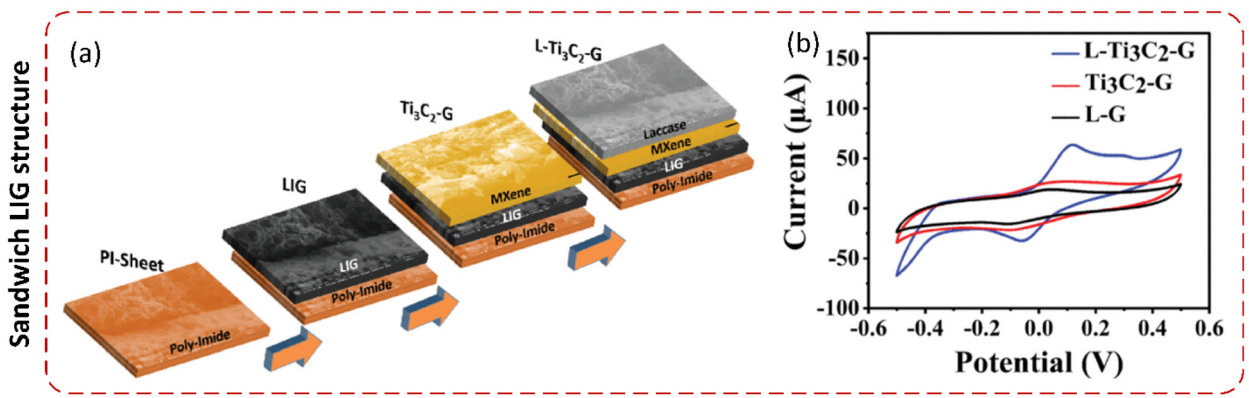


**Fig. 10** Stacked layer sandwich structure LIG devices. (a) Schematic illustration of the LBL synthesis process for the L-$Ti_3C_2$-G bio-electrode. (b) CV curves of L-$Ti_3C_2$-G and control electrodes (1 mM dopamine in pH 7 PBS at 20 mV). This figure has been adapted from ref. 142 with permission from IEEE, copyright 2022.

Open Access Article. Published on 09 February 2026. Downloaded on 5/23/2026 3:06:13 AM.
This article is licensed under a Creative Commons Attribution 3.0 Unported Licence.

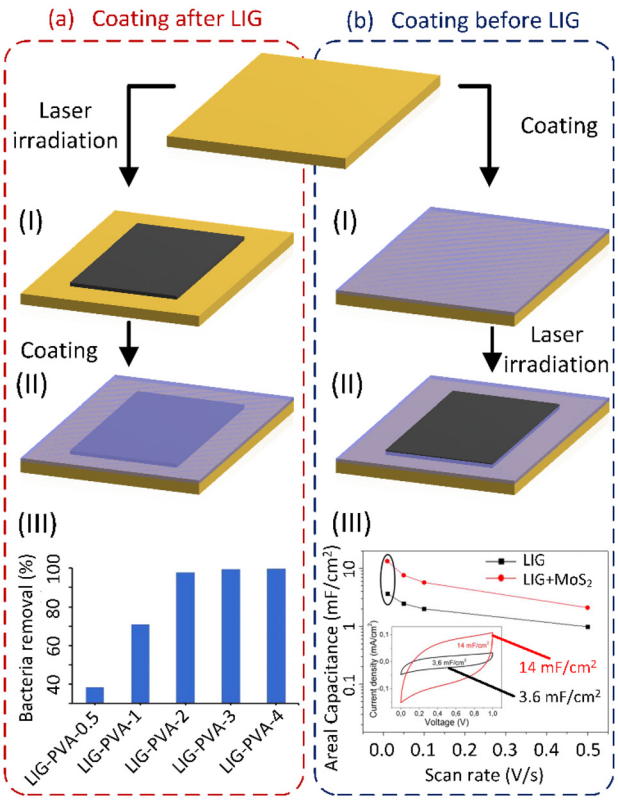


**Fig. 11** Coating on substrates for LIG. (a) Coating before LIG. (I) LIG formed after laser irradiation followed by (II) coating with a variety of materials. (III) A representative study showing results of the process of coating with PVA after LIG fabrication (LIG–PVA) on the polyethersulfone (PES) surface. LIG–PVA with different concentrations of PVA illustrating a higher bacterial removal percentage with increasing PVA concentration. This figure has been adapted from ref. 151 with permission from American Chemical Society, copyright 2019. (b) Coating after LIG. (I) Coated polymer followed by (II) laser irradiation to form LIG. (III) A representative study using the process of coating before LIG showing a comparison of capacitance *vs.* scan rate for pristine LIG and $MoS_2$–LIG with the inset showing the CVs at a scan rate of 10 mV $s^{-1}$. This figure has been adapted from ref. 157 with permission from American Chemical Society, copyright 2016.

**MXene-coated substrates.** The integration of MXene into LIG *via* various laser-based techniques has proved to be effective at enhancing its electrical conductivity. Femtosecond laser processing facilitates the embedding of MXene into the graphene lattice, resulting in a denser structure and significantly improved conductivity (up to 3187 S $m^{-1}$).[143] This method enables the direct and precise fabrication of wearable sensors for applications like motion detection and biochemical sensing, demonstrating how the interplay between the precursor material and laser parameters can optimize the lattice structure and functional properties of LIG.

Beyond conductivity enhancement, MXene coatings can also enable application-specific functionalities. For example, laser scribing on polyimide/MXene films generates porous LIG composites with TiCN nanoparticles.[144] This process leverages heteroatom interfaces and impedance matching, achieving excellent electromagnetic interference (EMI) shielding (up to 45 dB). Other approaches, such as picosecond laser processing and direct laser writing (DLW), further showcase the adaptability of MXene-enhanced LIG composites.[145] Picosecond lasers enable the formation of MXene-derived nanoparticles uniformly distributed on graphene, creating high-performance materials for flexible microsupercapacitors with enhanced energy density and cycling stability. Meanwhile, DLW of MXene-coated polyimide films produces LIG electrodes with increased porosity and conductivity, offering fivefold higher capacitance than pristine LIG.[146] A self-assembled MXene–graphene oxide composite precursor provides another pathway to improve ion transport and uniformity in LIG electrodes.[147] In comparison with LIG, the resulting composite shows an areal capacitance improvement from 0.62 mF $cm^{-2}$ to 2.33 mF $cm^{-2}$.

**Other dopant/oxide coatings.** Apart from the integration of MXene into LIG, a plethora of precursors have been studied by exploiting the substrate coating process to enhance various characteristics of LIG. For instance, S-doped porous graphene electrodes were fabricated by laser scribing a sodium lignosulfonate (SLS)-coated polyethersulfone (PES) film.[148] A slurry of SLS and hydroxyethyl cellulose (HEC) in deionized water was drop-cast onto PES and dried at 50 °C, followed by laser scribing the coated film using a $CO_2$ laser. The resulting S-doped porous graphene exhibited an ultrahigh areal capacitance of 55.4 mF $cm^{-2}$, excellent mechanical flexibility, and stable cycling performance (85.2% retention after 10 000 cycles), demonstrating its potential for high-performance microsupercapacitors.

Similarly, KOH-activated 3D porous graphene from KOH-coated polyimide films was fabricated.[47] Commercial polyimide was pre-treated with different concentrations of KOH (crystalline or solution form), followed by $CO_2$ laser writing. The process enhanced nitrogen doping, wettability, and the formation of mesoporous structures. The resulting electrodes demonstrated an areal capacitance of 32.00 mF $cm^{-2}$ (4.27 μWh $cm^{-2}$), with superior mechanical flexibility, cycling stability, and modular integration potential. Furthermore, Rodrigues *et al.*[149] developed a scalable method for fabricate ZnO-decorated laser-induced graphene (ZnO/LIG) composites. A $CO_2$ laser was used to irradiate a Kapton sheet covered with Zn/ZnO precursor paste, promoting the formation of ZnO microparticles on LIG. The precursor paste was prepared using Zn or ZnO commercial powders mixed with polyvinyl alcohol (PVA) or ethanol and terpineol to achieve a uniform layer on the Kapton sheet. The composites exhibit a four-fold increase in charge transfer resistance (from approximately 30 Ω to 120 Ω) compared to the LIG reference, as observed in electrochemical impedance spectroscopy (EIS) measurements.

**Polymer and biofunctional coatings.** Other studies include the utilization of phenolic resin (PR), poly(vinyl alcohol) (PVA), Prussian blue–chitosan (PB–CS), metals and CNTs. PR-based LIG is produced using a 405 nm semiconductor laser, yielding 3D porous structures with low resistance (~44 Ω $sq^{-1}$).[150] The process involves spin-coating PR solutions onto substrates, fol-

 This journal is © The Royal Society of Chemistry 2026

Open Access Article. Published on 09 February 2026. Downloaded on 5/23/2026 3:06:13 AM.
This article is licensed under a Creative Commons Attribution 3.0 Unported Licence.

lowed by laser engraving. Doping PR with light-absorbing materials (*e.g.*, metal salts) enhances LIG formation. The technique enables the fabrication of graphene-based electrochemical devices, such as supercapacitors and glucose biosensors, on diverse substrates. Results showed a specific capacitance of 0.78 mF $cm^{-2}$ at a scan rate of 500 mV $s^{-1}$.

Building on these polymer-coating approaches, functional overcoats and hybrid layers have been used to tailor LIG for separations and sensing. Thakur *et al.*[151] developed LIG–PVA composite membranes for ultrafiltration applications. LIG was generated on the surface of porous polyethersulfone (PES) membranes using a $CO_2$ laser. The LIG support was then coated with PVA solutions of varying concentrations (0.5–4%, w/v), followed by cross-linking with glutaraldehyde and HCl. Compared to LIG-coated filters, the PVA–LIG composite exhibited up to 63% increased bovine serum albumin rejection and ≈99.9% bacterial rejection (Fig. 11(a)(III)). The LIG layer retained its electrical conductivity, enabling antimicrobial effects when a voltage was applied. Furthermore, Barber *et al.*[152] fabricated a stable electrochemical sensor using LIG decorated with a PB–CS hybrid for hydrogen peroxide detection in sweat. LIG was laser-patterned on polyimide *via* $CO_2$ laser ablation. PB and CS were electrodeposited onto the LIG surface, forming a stable, conductive coating. The PB–CS-modified LIG sensor exhibited a high specificity for hydrogen peroxide with a detection limit of 6.31 μM and a recovery rate of 98.73% in human sweat. Jayapiriya *et al.*[153] developed enzymatic biofuel cells (EBFCs) using LIG bioelectrodes. LIG was patterned on a polyimide sheet *via* $CO_2$ laser ablation. The electrodes were plasma-treated to enhance hydrophilicity and functionalized with multi-walled CNTs *via* ultrasonic dispersion in ethanol. Enzymes (glucose oxidase and laccase) were immobilized through EDC-NHS crosslinking. The CNT-modified LIG bioelectrodes demonstrated enhanced electron transport, achieving 137% increase in power density (2.2 μW $cm^{-2}$) compared to unmodified LIG (1.6 μW $cm^{-2}$) under a 200 μL $min^{-1}$ flow rate in a PDMS microfluidic device.

**Metal nanoparticles and $MoS_2$ coatings**. Additionally, metal nanoparticles such as iron, gold, silver, and platinum have been explored to fabricate LIG composites using coatings. Ghosh *et al.*[154] recently used a desktop laser printer to cover commercial polyimide films with a magnetic ink character recognition (MICR) toner containing iron oxide particles to enhance the absorptance of the polymer to near-infrared laser, boosting LIG formation. Rodriguez *et al.*[155] demonstrated a laser-driven polymer–nanomaterials integration strategy by coating PET with Al nanoparticles and laser processing to form a conductive polymer/Al/LIG composite (including Al carbide formation), enabling mechanically resilient flexible electronic features. You *et al.*[156] used a hydrogel ink containing chitosan and metal precursors ($HAuCl_4$, $AgNO_3$, or $H_2PtCl_6$), which was blade-coated onto a polyimide substrate and dried before laser scribing. The resulting AuNP–LIG composites were used to fabricate interdigitated array electrodes for a flexible impedimetric immunosensor, which demonstrated high conductivity, a large surface area, and strong selectivity for *Escherichia coli* O157:H7 detection. In parallel, Clerici *et al.*[157] and Chhetry *et al.*[158] coated PI with $MoS_2$ with drop casting and spin coating, respectively. This was followed by $CO_2$ laser scribing to form a porous graphene network, improving the electrical properties and increasing surface area. As shown in Fig. 11(b)(III), the areal capacitance increased from 3.6 to 14 mF $cm^{-2}$. The $MoS_2$–LIG sensor demonstrated a high gauge factor (1242), negligible hysteresis (≈2.75%), and fast response times (0.17 s), with reliable performance over 12 000 cycles. The sensor was applied to detect subtle human motions, including phonation and the wrist pulse, making it suitable for wearable electronics and healthcare monitoring.

### 2.5. Sustainability considerations for LIG precursors

To reduce environmental impact and promote resource efficiency, researchers have increasingly explored sustainable precursors for LIG. Green LIG, derived from renewable bio-based sources such as wood, leaves, cork, lignin, and nanocellulose, offers a potentially smaller environmental footprint than fossil-based or synthetic polymers, while also enabling circular-material narratives when agricultural/forestry by-products are used as feedstocks. The chemical structure of these materials (particularly their aromatic or aliphatic nature) strongly influences the graphitization behavior and LIG quality. To improve energy efficiency and minimize waste, studies have focused on optimizing laser parameters such as wavelength, power, pulse characteristics, and scan speed, since these directly control the required fluence, number of passes, and ultimately the energy per functional area. Controlling laser fluence and the atmospheric environment is also critical to prevent combustion and ensure high-quality LIG formation. These developments mark important progress toward scalable, eco-friendly graphene production for energy, sensing, and environmental technologies.[43]

However, most current assessments focus primarily on the energy used during laser processing, overlooking emissions and waste generated during precursor fabrication and post-processing. A more holistic evaluation of sustainability should account for the full life-cycle energy consumption and environmental burdens across all stages of LIG production.[159]

Here, we highlight the need for adopting a holistic life-cycle assessment (LCA) approach for cost–benefit analysis for precursor selection.[160,161] A comprehensive multi-stage framework is needed to assess the overall sustainability of LIG precursors. For synthetic polymers, this begins with estimating the energy and emissions associated with polymer synthesis and processing, which can be highly sensitive to solvent selection and process design. For example, an integrated study of polyimide membrane fabrication found that membrane preparation could dominate toxicity-related burdens, and that replacing a conventional solvent (*e.g.*, NMP) with less toxic alternatives could reduce toxicity impacts, even though some "green" solvents might be less competitive economically, underscoring the need to evaluate both environmental and cost trade-offs.[162]

Similarly, for bio-based and fossil-derived materials, the energy required for extraction, pretreatment, or refinement

Open Access Article. Published on 09 February 2026. Downloaded on 5/23/2026 3:06:13 AM.
This article is licensed under a Creative Commons Attribution 3.0 Unported Licence.

must be included, as these processes vary widely in intensity.[160,163] This is particularly relevant for nanocellulose-related supply chains, where LCA studies report a broad spread in cumulative energy demand depending on pretreatments and mechanical fibrillation routes, meaning that 'bio-based' does not automatically imply low-impact without careful process and energy-source choices.[163]

The second stage considers the energy required during laser scribing. Since some precursors demand higher laser fluence or multiple passes to achieve adequate graphitization, their energy footprint during this step can be substantially larger. Consistent with this, a recent laboratory-scale LCA comparing LIG produced from petroleum-derived polyimide and bio-derived precursors concluded that precursor choice mainly affected sustainability indirectly by shifting the optimal scribing conditions, and that the bio-derived nature of the precursor did not automatically improve overall environmental performance within the studied cradle-to-gate boundary.[160] Importantly, sensitivity analysis showed that switching to a near-fully renewable electricity mix could reduce LIG impacts by ≈70% (*vs.* a fossil-heavier baseline), and the authors concluded that LIG was only likely to be environmentally sustainable if energy used across process phases was supplied by renewables.[160]

Lastly, post-processing steps (such as doping, secondary scribing, or transfer methods) may be necessary to improve LIG quality and device integration.[164] Whether these steps introduce additional energy costs or environmental burdens remains an open question and should be evaluated alongside precursor selection. More broadly, prospective LCAs of graphene production routes highlight that focusing on energy alone can be misleading: for instance, ultrasonication-based in-solution graphene can reduce energy and water use relative to chemical reduction, yet increase human/ecotoxicity impacts unless solvent recovery is implemented, emphasizing that solvent/chemical management and multi-impact-category accounting are essential when assessing 'greenness'.[161]

# 3. Modified LIG processes

Multiple types of LIG process modifications have been proposed. One modified process involved LIG transfer, which was developed to address the limitation of LIG remaining adhered to its growth substrate. Techniques such as laser-induced forward transfer (LIFT),[165,166] backward transfer (LIBT),[167,168] and explosive synthesis and transfer (LEST)[169,170] enable the direct detachment and redeposition of graphene onto a wide range of substrates. These approaches enhance spatial control, improve substrate compatibility, and eliminate the need for wet-transfer steps, thereby broadening the scope of LIG integration in flexible and functional devices. Another promising approach is additive manufacturing (AM) of LIG, which enables precise, layer-by-layer fabrication of complex structures.[171] While the fabrication of three-dimensional graphene architectures using conventional AM remains constrained by material processability, recent developments in LIG-based AM provide a compelling alternative for constructing 3D carbon architectures with enhanced structural complexity and design flexibility.[172,173] A third emerging method is second laser scribing, which involves re-irradiating pre-formed LIG to further modify its chemical and physical properties.[37] This technique facilitates *in situ* doping, nanomaterial incorporation, and morphology refinement, resulting in improved conductivity, wettability, and electrochemical performance.[174] By enabling the formation of multifunctional hybrid structures (such as metal oxide–graphene composites and heteroatom-doped LIG) second laser scribing offers a scalable, controllable route for upgrading the functionality of LIG-based devices.[175,176]

## 3.1. Transfer

As discussed thus far, it is not an exaggeration to say that LIG has demonstrated transformative potential for the production of functional graphene-based materials on flexible substrates by offering a straightforward method to convert carbon rich precursors, such as PI using laser irradiation under ambient conditions.[177,178] However, LIG has some limitations that restrict its broader applicability. The LIG process often results in a foam-like graphene structure with a relatively high defect density and non-uniform morphology, which can impact its electronic properties and make it less suitable for applications requiring a precise material quality.[171] Additionally, the graphene produced by LIG remains adhered to the precursor substrate, which necessitates additional transfer steps, such as adhesive assisted peeling or chemical etching to integrate the material onto a different substrate.[178] Recent advancements in graphene synthesis focus on modified processes that improve the material quality, scalability, and transfer efficiency to various substrates.

Laser induced transfer (LIT) represents an innovative class of techniques used to deposit functional materials onto substrates with precision and control.[179,180] These techniques depend on the interaction of the laser energy with a donor material to facilitate the ejection and deposition of the material onto an acceptor substrate.[181] Two of the well-established techniques in this category are laser-induced forward transfer (LIFT)[165,166,182] and laser-induced backward transfer (LIBT).[167,168] Representative LIFT/LIBT implementations, key outcomes, and common limitations are summarized in Table 1.

**Laser-induced forward transfer (LIFT).** A recent study conducted by Paula *et al.*[183] utilized the LIFT technique to fabricate high resolution integrated electrodes composed of graphene oxide and silica for sensing applications. The process was conducted using a femtosecond laser system with pulse energy thresholds as low as 70 nJ, allowing for the fabrication of 2 μm wide lines on a glass substrate. The LIFT process leveraged ultrashort laser pulses to reduce thermal effects, enabling localized GO reduction within the silica matrix without material degradation as evident from Raman spectroscopy results, where the $I_D/I_G$ ratio increased from 0.95 to 1.29. Unlike LIG, which depends on a continuous carbon source,

 This journal is © The Royal Society of Chemistry 2026

Open Access Article. Published on 09 February 2026. Downloaded on 5/23/2026 3:06:13 AM. This article is licensed under a Creative Commons Attribution 3.0 Unported Licence.

Table 1 Summary of laser-induced forward and backward transfer techniques

| Technique | Donor material | Receiver material | Applications | Results | Limitations | Ref. |
|---|---|---|---|---|---|---|
| Blister-based laser induced forward transfer (BB-LIFT) | Graphene nanoribbons on nickel foil | $SiO_2$/Si | Nanoelectronics, advanced sensors | Retention of graphene nanoribbon crystal structure verified by Raman spectroscopy | Requires controlled film thickness (500–100 nm) and annealing for donor preparation | 182 and 183 |
| Femtosecond LIFT (fs-LIFT) | Go/$SiO_2$ | Quartz, glass, polymer | Sensing devices, optoelectronic components | Electrode lines with widths of 2 μm were fabricated; GO was reduced to rGO without material degradation | Thermal effects require precise laser energy control (70 nJ threshold) | 183 |
| Pulse energy controlled laser induced forward transfer (LIFT) | Modified donor substrate with GO suspension | Glass substrate with laser induced cavities | Microfluidic devices | Uniform GO droplets were deposited reproducibly, with enhanced hydrophilicity aiding uniform coating and transfer efficiency | Requires laser ablation of donor glass | 184 |
| Laser induced forward transfer (LIFT) | CVD-grown graphene with triazene release layer | Pre-patterned silicon wafers | Field effect transistor, semiconductor devices | Patterned CVD graphene features transferred with sharp edges; functional graphene FETs demonstrated (reported mobility ≈10–15 $cm^2 V^{-1} s^{-1}$ for holes and ≈5 $cm^2 V^{-1} s^{-1}$ for electrons) | Requires use of a sacrificial triazene layer for clean transfer, limited scalability | 166 |
| Laser induced backward transfer (LIBT) | Graphene coated nickel | Glass | Photonic devices | Circular graphene regions of 30 μm diameter; retained graphene's structure | Requires low-pressure environment | 167 |
| Laser induced backward transfer (LIBT) | Gold films (5, 10, 60 nm) on silicon/glass | PDMS | Optoelectronics transparent conductive electrodes | Disk shaped Au nanostructures of 15 μm wide; retained pristine thickness | Highly dependent on substrate reflectivity and requires ultra-thin films (<60 nm) for optimal transfer | 185 |
| Simultaneous LIG and laser Induced backward transfer (LIBT) | Polyimide sheets | Glass and PDMS | Flexile hybrid supercapacitors, wearable electronics | High adhesion graphene patterns; resistivity of 68 μΩ m for the glass substrate | Risk of thermal damage of PI, challenges in achieving precise alignment for transfer | 186 |
| Laser induced backward transfer (LIBT) | Highly oriented pyrolytic graphite (HOPG) | PDMS | Biosensor implants | Successful transfer of HOPG thin films onto PDMS with minimal contamination; excellent surface uniformity and controlled deposition | Contamination risks from donor or receiver substrates | 168 |

LIFT allows for hybrid material integration and higher precision deposition.

**Laser-induced backward transfer (LIBT).** Complementary to forward transfer, Praeger *et al.*[167] demonstrated LIBT as a precise and efficient approach for transferring monolayer graphene onto target substrates. This approach enables the material to be transferred in the opposite direction to that of laser propagation, leveraging rapid thermal expansion of the donor substrate like nickel-coated quartz to achieve localized ejection and deposition. The study utilized a femtosecond laser with a pulse energy of up to 1 mJ, a wavelength of 800 nm, and a pulse duration of 190 fs. In addition, using a digital micromirror device shapes the laser beam to deliver controlled spatial fluence ranging from 26 to 30 mJ $cm^{-2}$. The results showed that the transferred graphene had an intact structural feature, with Raman spectra showing prominent G (1583 $cm^{-1}$) and 2D (2666 $cm^{-1}$) peaks, indicating high-quality monolayer graphene. This study demonstrated the ability to transfer pre-synthesized graphene from chemical vapor deposition substrates without the need for polymeric intermediate layers.

While these methods provide significant advantages, such as precise control over material deposition, compatibility with different substrates, and the ability to pattern functional materials with higher spatial resolution, they are multi-step processes, with requirements of high vacuum systems[167] or prefabricated donor materials,[182] which can result in inconsistent quality and limited scalability.

**Laser-mediated explosive synthesis and transfer (LEST).** An innovative modification of the LIG process through laser mediated explosive synthesis and transfer (LEST) was first introduced in the work of Bhorkar *et al.*[169] Unlike LIG, LEST combines synthesis and transfer in a single step process, utilizing the explosive decomposition of carbon precursors to simultaneously generate and deposit high quality graphene onto the target substrate (Fig. 12a).[169] The study employs a pulsed Nd:YAG laser to decompose PI or PI with silicone adhesive precursors. Laser irradiation causes rapid thermal and photochemical reactions, releasing CO and $CO_2$ gases. The explosive reaction propels graphene flakes or hybrid graphene/$SiO_x$ onto the substrate. Two configurations were proposed in their study, the forward LEST where the laser irra-

Open Access Article. Published on 09 February 2026. Downloaded on 5/23/2026 3:06:13 AM.
This article is licensed under a Creative Commons Attribution 3.0 Unported Licence.

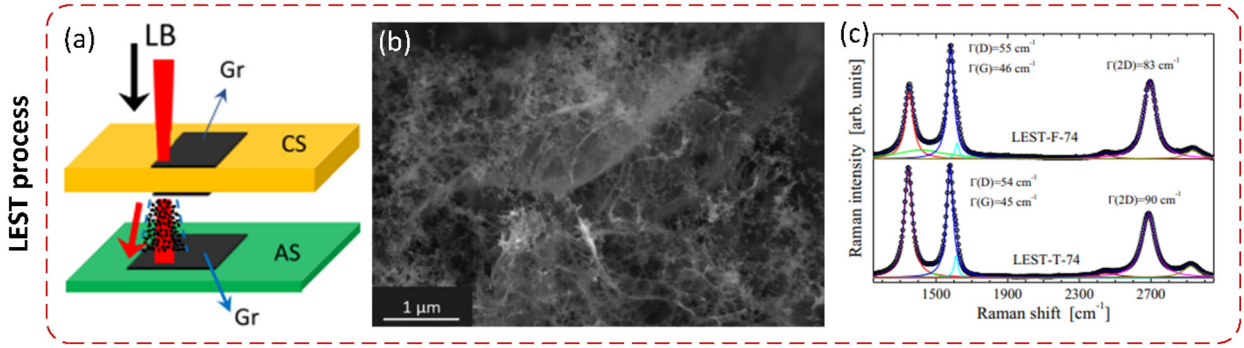


**Fig. 12** Laser mediated explosive synthesis and transfer process. (a) Laser mediated explosive synthesis and transfer (LEST) process setup. (b) SEM image showing the morphology of the graphene flakes produced by the LEST process. (c) Raman spectra of the graphene flakes grown by LEST on different precursors (foil and tape). This figure has been adapted from ref. 169 with permission from Springer Nature, copyright 2022.

diated the precursor, and graphene was deposited on a substrate placed beneath it. Another configuration is the backward LEST where graphene is deposited on a transparent substrate placed between the laser and the precursor. These configurations enable the process to accommodate various substrate geometries and materials, such as polymers, metals, ceramics, glass, and flexible surfaces like PDMS. The results confirmed the porous and turbostratic nature of graphene through Raman spectroscopy and high-resolution transmission electron microscopy, which revealed an interlayer spacing of 0.341–0.364 nm, exceeding the typical Bernak stacking of 0.334 nm (Fig. 12b and c).

**Process optimization for energy-storage electrodes.** Samartzis *et al.*[170] further optimized the laser mediated explosive synthesis and transfer process to enhance the quality and performance of graphene electrodes for supercapacitor applications. By refining the laser parameters, such as fluence, pulse width, and overlap, they achieved a more uniform deposition of foam-like turbostratic graphene directly onto a carbon fiber paper substrate. The resulting graphene exhibited a high $sp^2$ carbon content of almost 95% and low defect density, which was evident from the low $I_D/I_G$ ratio of 1.44. These improvements in the LEST process demonstrate its ability to produce high quality graphene with consistent results.[170]

### 3.2. 3D printing

Additive manufacturing (AM) techniques have revolutionized the field of materials science by enabling the fabrication of complex three-dimensional structures with precision and control. These techniques utilize layer-by-layer deposition of materials to build up a desired shape or structure, offering design freedom and the ability to create intricate geometries that would be impossible to achieve through traditional manufacturing methods. However, an area that has yet to be fully explored in AM is the fabrication of three-dimensional carbon structures, specifically graphene. Two processing methods have been employed majorly to produce macroscopic graphene structures: bulk formation and layer-by-layer assembly.

**Bulk formation:** The bulk formation approach involves utilizing non-printing methods to produce graphene structures. This can be achieved by synthesizing graphene on 3D porous metal templates or hydrothermally treating graphene oxide (GO) dispersion to create bulk foam structures. Chen *et al.*[187] and Cao *et al.*[188] employed chemical vapor deposition (CVD) to grow graphene on macroporous nickel and seashell templates, resulting in freestanding foam-like structures measuring 20 × 20 × 2 $mm^3$ after the etching process. Xu *et al.*[189] and Liu *et al.*[190] utilized hydrothermal and directional-freezing methods, respectively, to cast and reduce GO suspension into self-assembled graphene hydrogels or aerogels with a cylindrical volume of approximately 9 $cm^3$. Despite achieving a centimeter-scale architecture, the bulk formation strategy faces limitations in shaping arbitrary forms due to the absence of a controllable fabrication trajectory.

**Layer-by-layer assembly.** The layer-by-layer assembly method employs computer-aided processes for constructing 3D graphene structures through various AM techniques.[191,192] Hensleigh *et al.*[193] and Jiang *et al.*[192] used photocurable GO resin and GO sol–gel ink, respectively, to print micron-scale, self-standing 3D graphene structures with programmable microlattices. While enhancing structural complexity and design flexibility, these methods often rely on GO-based inks, gels, and resins, posing challenges in terms of intricate processing steps, extended processing time, and limited size scalability. These complexities complicate quality control and result in variations between parts.[194] Therefore, a novel 3D printing strategy is needed for swift assembly, freeform structuring, and simplified quality control in constructing graphene macrostructures. The following sections delineate methodologies for fabricating bulk graphene architectures *via* LIG.

**3.2.1. Laminated object manufacturing inspired. LOM-enabled 3D graphene foams from LIG/LIGF.** Luong *et al.*[195] introduced a novel AM method to 3D print millimeter-scale graphene foam (GF) using laser-induced graphene (LIG) and laser-induced graphene fiber (LIGF) as fundamental building blocks. LIG/LIGF are synthesized through a simple, one-step photothermal process by irradiating commercial polyimide

 This journal is © The Royal Society of Chemistry 2026

Open Access Article. Published on 09 February 2026. Downloaded on 5/23/2026 3:06:13 AM.
This article is licensed under a Creative Commons Attribution 3.0 Unported Licence.

(PI) films using a $CO_2$ laser. This converts PI into porous graphene sheets (LIG) or fibers (LIGF) directly, without needing metal templates or the chemical reduction of graphene oxide. The authors developed a laminated object manufacturing (LOM) technique to 3D print stacked layers of LIG/LIGF as macroscale foams. As illustrated in Fig. 13(b)(I), the process involves coating LIG/LIGF layers with ethylene glycol (EG) as a binder, stacking the layers, and using the $CO_2$ laser to fuse the layers together into a 3D porous network. EG wets the LIG completely and acts as an adhesive through capillary forces. An automated 3D printing system is built using simple, low-cost parts to demonstrate the potential scalability for industrial production. Furthermore, the authors introduce a computer-controlled fiber laser milling method to selectively ablate LIG and enable the preparation of complex 3D geometries and features that are unachievable through the LOM method alone (Fig. 13(b)(II)). The fiber laser, with a wavelength of 1.06 μm, can selectively remove LIG while preserving the PI substrate due to their different optical absorption properties. This enables features with 10× higher resolution compared to $CO_2$ laser patterning. By combining both the LOM stacking method and fiber laser milling, intricate 3D LIG objects are fabricated.[195]

**Laminated LIG paper composites and process–property tuning**. Gao *et al.*[196] introduced a method to fabricate 3D LIG macrostructures by laminating multiple layers of LIG papers (LIGPs). The LIGPs are produced by irradiating PI paper with a $CO_2$ laser to convert it into porous graphene sheets. The LIGPs are then infiltrated with epoxy resin solution to prepare prepregs. Multiple prepreg layers can be stacked and hot pressed to construct 3D laminated LIGP composites (LIGP-C) with large areas, high thicknesses, and customizable shapes. They systematically investigated how processing factors like laser power, resin type, resin content, and layer number influenced

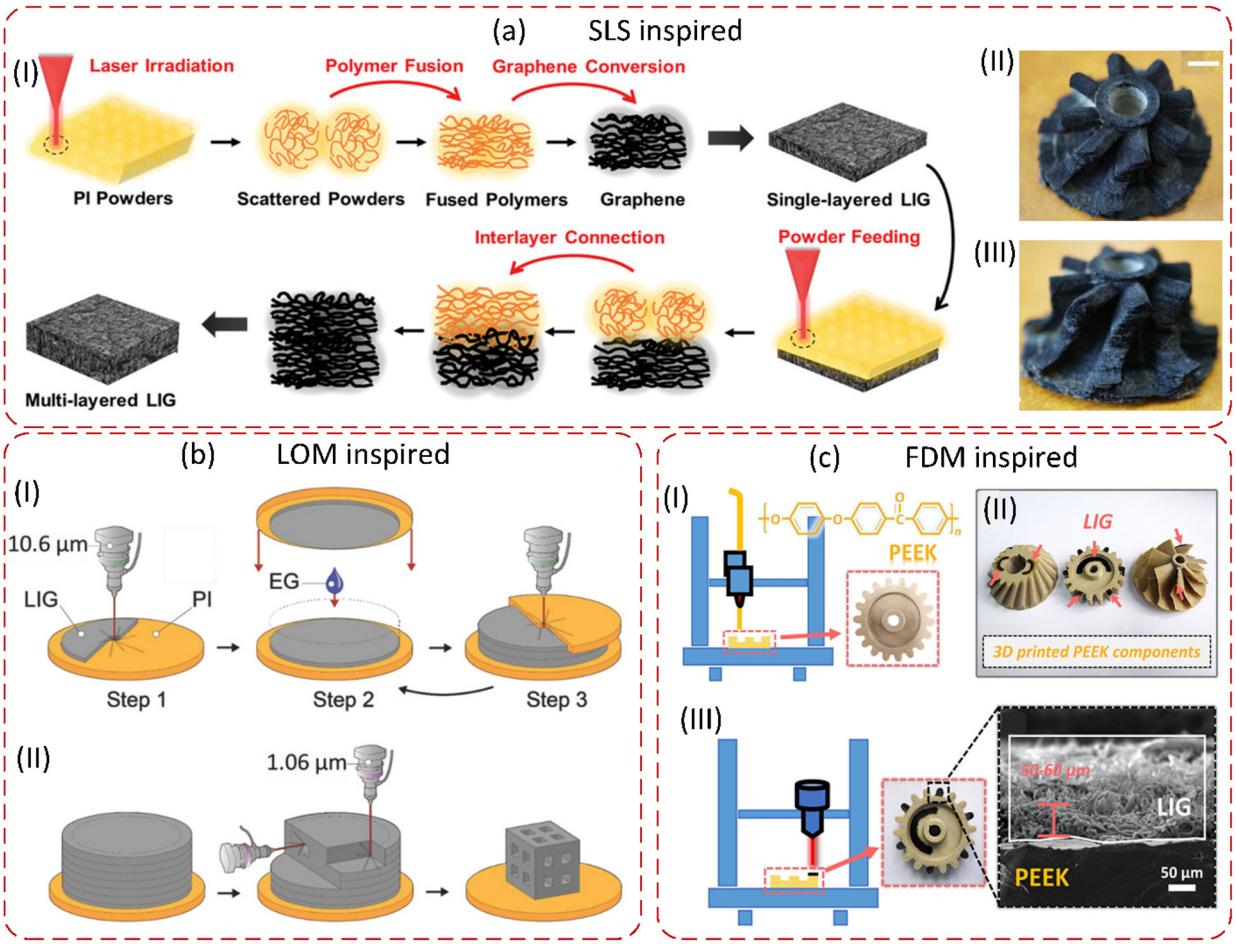


**Fig. 13** 3D printing technology for LIG. (a) Processing mechanism and structural characterization for SLS inspired 3D printing of LIG. (I) Schematic illustration of the LIG–AM process for fabricating multi-layered 3D structures. (II) and (III) A whole 3D printed graphene turbine (scale = 5 mm). This figure has been adapted from ref. 197 with permission from John Wiley and Sons, copyright 2022. (b) Manufacturing and processing of 3D LIG using a LOM inspired process. (I) Schematic of the LOM process. (II) Schematic of the fiber laser milling process to achieve arbitrary 3D geometries. This figure has been adapted from ref. 195 with permission from John Wiley and Sons, copyright 2018. (c) FDM inspired process. (I) Schematic of the 3D printing process for the PEEK component, with the inset showing a photograph of a printed gear. (II) Schematic of the LIG synthesis process from the 3D-printed PEEK gear, with insets displaying a laser-scribed gear. (III) A representative 3D printed PEEK-LIG component. This figure has been adapted from ref. 198 with permission from American Chemical Society, copyright 2020.

Open Access Article. Published on 09 February 2026. Downloaded on 5/23/2026 3:06:13 AM. This article is licensed under a Creative Commons Attribution 3.0 Unported Licence.

the multifunctional properties of 3D LIGP-C, including mechanical strength, electrical conductivity, and piezoresistivity. In the above-discussed methodologies, impediments persist in the realization of freeform structures, despite the advancements achieved by LIG in generating macroscopic dimensions. The utilization of these approaches necessitates the incorporation of specific binding, milling, or 3D-molding processes, thereby constraining the facile production of graphene in straightforward configurations on an expanded scale.[196]

3.2.2. **Powder bed fusion inspired. PI powder for LIG additive manufacturing (LIG-AM).** Liu *et al.*[197] introduced a new 3D printing method called LIG-based AM (LIG-AM) to construct complex 3D macrostructures made of graphene (Fig. 13(a)(I)). It utilizes PI powder as the raw material, which serves dual functions of particle sintering and graphene conversion when irradiated by a computer-controlled $CO_2$ laser layer-by-layer. The LIG-AM technique is inspired by powder bed fusion (PBF) but also induces graphene formation from the PI powder bed. By pre-programming the laser scanning path for each layer, diverse types of 3D architectures can be printed, including identical-section, variable-section, and graphene/PI hybrid structures with complex geometries (Fig. 13(a)(II) and (III)). No additional binders, templates or catalysts are needed. They studied how to balance processing efficiency and resolution by tuning the laser power and powder layer thickness. Higher laser power increases the build rate but reduces quality, while thinner layers improve resolution but reduce speed. A wide range of properties of 3D printed graphene is characterized including density, mechanical properties, conductivity, electrochemistry and Joule heating.[197]

While 3D printing of graphene structures with adjustable characteristics has been proposed, offering a binder-free technique, it is important to acknowledge certain drawbacks of the SLS process, including waste production and potential limitations in achieving high levels of detail and precision in complex structures. SLS can also be associated with higher equipment and material costs compared to other 3D printing methods such as directed energy deposition (DED), making it less cost-effective for some applications. Additionally, post-processing steps may be necessary to improve the surface finish of SLS-printed objects.

**Metal-assisted printing of graphene foams**. Sha *et al.*[130] developed a method for automating the three-dimensional (3D) printing of freestanding graphene foam (GF) using metal powder. The process involves manually placing a mixture of Ni and sucrose onto a platform, followed by using a commercial $CO_2$ laser to transform the Ni/sucrose mixture into 3D GF. In this technique, sucrose serves as the solid carbon source for graphene, while sintered Ni metal acts as the catalyst and template for graphene growth. This straightforward and effective approach combines powder metallurgy templating with 3D printing methods, allowing for direct *in situ* 3D printing of GF without the need for a high-temperature furnace or an extended growth process. The resulting 3D printed GF exhibits remarkable properties, including high porosity (≈99.3%), low density (≈0.015 g $cm^{-3}$) and high-quality multilayered graphene features an electrical conductivity of ≈8.7 S $cm^{-1}$. Implementing a binder-free approach, Sha *et al.* utilized a mixture of sucrose and nickel particles as a carbon source and catalyst for the sequential layer-by-layer growth of graphene on a metal template. While this method successfully produces foams with sizes of 1 × 1 × 0.8 $cm^3$, the subsequent template etching process unavoidably results in significant volume reduction, limiting the precision of the shaping process.[130]

3.2.3. **Fused deposition modeling inspired.** Yang *et al.*[198] introduced a strategy to fabricate smart components by combining 3D printing and laser-scribing technologies. The goal is to create polymer components with integrated sensors for self-monitoring capabilities. Polyether ether ketone (PEEK) provides a high-strength 3D-printable matrix. As depicted in Fig. 13(c), the approach uses fused deposition modeling (FDM) 3D printing with a PEEK filament to construct the component shapes. Then a $CO_2$ laser is used to scribe thin patterns of LIG sensors directly onto the PEEK surfaces. Laser irradiation converts the aromatic PEEK polymer into porous, few-layer graphene in a simple, one-step process requiring no catalysts. While this method opens a platform to bridge the gap between AM and LIG, it cannot produce graphene structures with arbitrary shapes, as it relies on an additional substrate material and does not achieve full-form LIG characteristics.[198]

### 3.3. Multi-pass laser scribing

Multi-pass laser scribing (also referred to as secondary or duplicate laser pyrolysis) revisits a previously scribed region one or more times, often with an intentional modification step between passes. This sequencing (scribe, modify, and re-scribe) treats LIG optimization as a processing problem, enabling densification/thickening of the conductive scaffold, tailored surface chemistry *via* interlayer dopant coatings, and *in situ* conversion of deposited precursors into functional phases, while preserving the mask-free patterning advantages of direct laser writing.[176]

**Duplicate laser pyrolysis for densification and heteroatom co-doping**. In a representative duplicate-pyrolysis workflow, the first pass forms LIG (or N-doped LIG) on PI, the surface is coated with an additional polyamic acid (PAA) layer containing dopant precursors, and a second pass simultaneously densifies the carbon network and incorporates heteroatoms. Using PAA/$H_3BO_3$ coatings, Khandelwal *et al.*[174] produced N/B co-doped densified LIG and increased the areal capacitance to 104.3 mF $cm^{-2}$ (0.2 mA $cm^{-2}$), far exceeding singly pyrolyzed LIG and N-doped dLIG. The same concept was extended to N/P co-doping by applying $H_3PO_4$ in the second pyrolysis step, achieving an areal capacitance of 163.6 mF $cm^{-2}$ in a three-electrode configuration and 69.7 mF $cm^{-2}$ in a gel-electrolyte solid-state device with good cycling stability.[176]

Beyond inter-pass coatings, speed-dependent sequential 'relasing' can also be used as an additive-free second-pass refinement step: by decoupling kinetically limited carbonization in the first pass from higher-temperature graphitization in the second, Abdulhafez *et al.*[37] reported an order of magnitude reduction in electrochemical impedance relative to

 This journal is © The Royal Society of Chemistry 2026

Open Access Article. Published on 09 February 2026. Downloaded on 5/23/2026 3:06:13 AM.
This article is licensed under a Creative Commons Attribution 3.0 Unported Licence.

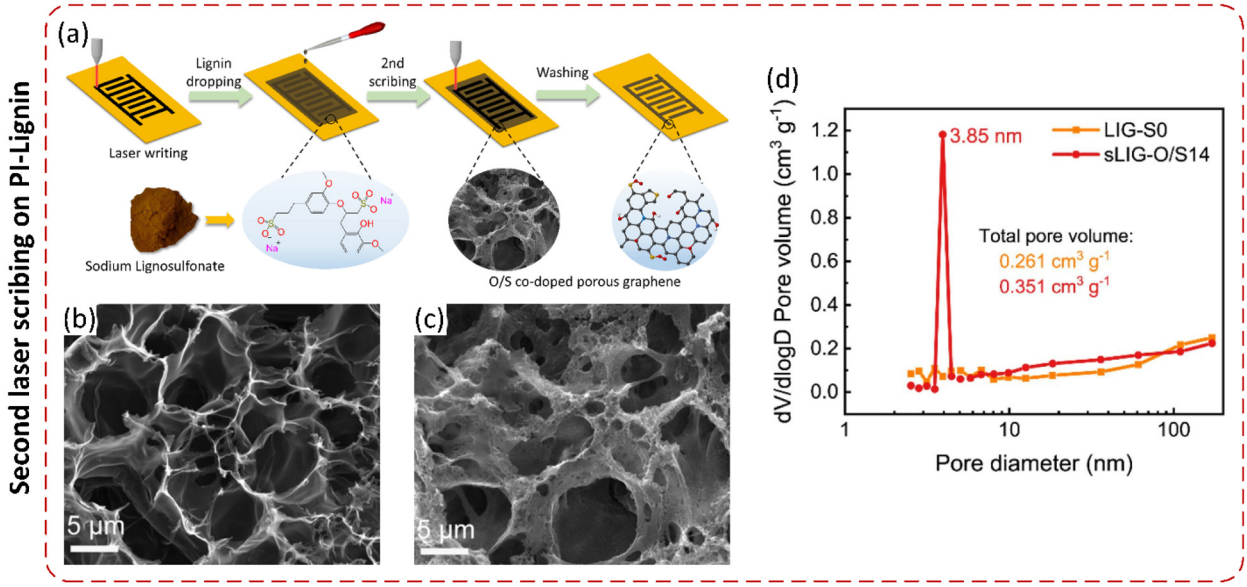


**Fig. 14** Second laser scribing on PI-lignin for improved LIG performance. (a) Schematic illustration of the fabrication of superhydrophilic O/S co-doped LIG electrodes. (b) Top-view SEM images of LIG-S0 (lignin = 0 wt%) electrodes. (c) Top-view SEM images of sLIG-O/S14 (lignin = 14 wt%) electrodes. (d) BJH pore size distribution of LIG-S0 and sLIG-O/S14 samples. This figure has been adapted from ref. 199 with permission from Elsevier, copyright 2021.

single-pass writing, accompanied by increased graphitic crystallinity and a reduced heteroatom content. Repeat-pass raster writing can also be used simply to improve pattern continuity while combining laser cutting and scribing in one workflow: in kirigami-based transparent, flexible EMI shields, a $CO_2$ laser defines the cut geometry (multi-pass vector cutting) and then converts the remaining PI into LIG in raster mode using two passes (with defocus); this is reported to consistently yield a continuous, conductive LIG layer.[34]

**Inter-pass coating to engineer porosity and electrolyte accessibility.** Beyond heteroatom chemistry, inter-pass coatings can act as both dopant sources and pore-forming agents. For example, Yuan *et al.*[199] used sodium lignosulfonate as a biomass-derived coating on PI and employed a follow-up laser step to generate O/S co-doped porous LIG; the resulting micro-supercapacitor delivered an areal capacitance of 53.2 mF $cm^{-2}$ at 0.1 mA $cm^{-2}$ with 86.5% retention after 10 000 cycles. As shown in Fig. 14, the secondary scribing altered the pore architecture and increased the surface-accessible area compared with the singly scribed control, consistent with hierarchical micro/mesoporosity introduced by the lignosulfonate-derived interlayer.[199]

**Sequential laser conversion of deposited precursors into functional phases.** Multi-pass scribing also provides a direct route to convert deposited precursors into integrated pseudocapacitive phases or electrocatalysts. Khandelwal *et al.*[200] demonstrated $Co_3O_4$ nanoparticle formation on N-doped LIG *via* duplicate laser pyrolysis, yielding a uniform $Co_3O_4$ distribution and an areal capacitance of 216.3 mF $cm^{-2}$ at 0.5 mA $cm^{-2}$ (three-electrode), with a solid-state device delivering 17.96 mF $cm^{-2}$. Similarly, by loading metal precursors onto a pre-formed LIG surface followed by laser scribing, Tour's group synthesized NiFe/LIG *via* a solid-phase transition for an alkaline OER, reaching an overpotential of 240 mV at 10 mA $cm^{-2}$ with a Tafel slope of 32.8 mV $dec^{-1}$.[201] For metal–air batteries, ternary metal oxide/LIG hybrids integrating ORR-active Co/Mn and OER-active Ni/Fe were formed within an *in situ* laser-induced graphene film, enabling rechargeable Zn–air batteries with a peak discharge power density of 98.9 mW $cm^{-2}$ and an energy density of 842 Wh $kg^{-1}$ Zn over >200 h cycling;[202] related $Co_3O_4$/LIG bifunctional catalysts delivered a Zn–air power density of 84.2 mW $cm^{-2}$ at 100 mA $cm^{-2}$.[175] Finally, sequential laser writing is not limited to PI: a two-step laser process on PEEK enabled direct patterning while synthesizing $MnO_2$-decorated graphene electrodes for flexible micro-supercapacitors with improved areal capacitance and cycling stability.[203]

## 4. Overcoming throughput–resolution–performance trade-offs

LIG has emerged as a promising fabrication technique due to its simplicity, scalability, and ability to produce conductive structures directly from precursor materials. However, achieving both high resolution and high throughput remains a challenge, as laser parameters such as wavelength, fluence, and scanning speed significantly influence the resulting feature size and conductivity. Various fabrication techniques, including lithography and transfer-based processes, offer alternative approaches but often involve trade-offs between resolution, conductivity, and scalability. Understanding these relation-

Open Access Article. Published on 09 February 2026. Downloaded on 5/23/2026 3:06:13 AM.
This article is licensed under a Creative Commons Attribution 3.0 Unported Licence.

ships is crucial for optimizing LIG fabrication and advancing its application in high-performance electronics.

### 4.1. Speed–resolution landscape across laser wavelengths

As illustrated in Fig. 15(a), various advanced manufacturing techniques demonstrate a trade-off between printing speed and resolution, with LIG positioned within this landscape based on different laser wavelengths (considering different precursor materials). The fastest reported LIG processing speed of 1200 mm $s^{-1}$ results in a minimum line width of 350 microns, whereas the smallest reported line width of ≈6 microns is achieved at a significantly lower speed of ≈20 mm $s^{-1}$, as shown more clearly in Fig. 15(b).[70,204] The highest speeds are attained using $CO_2$ lasers under ambient

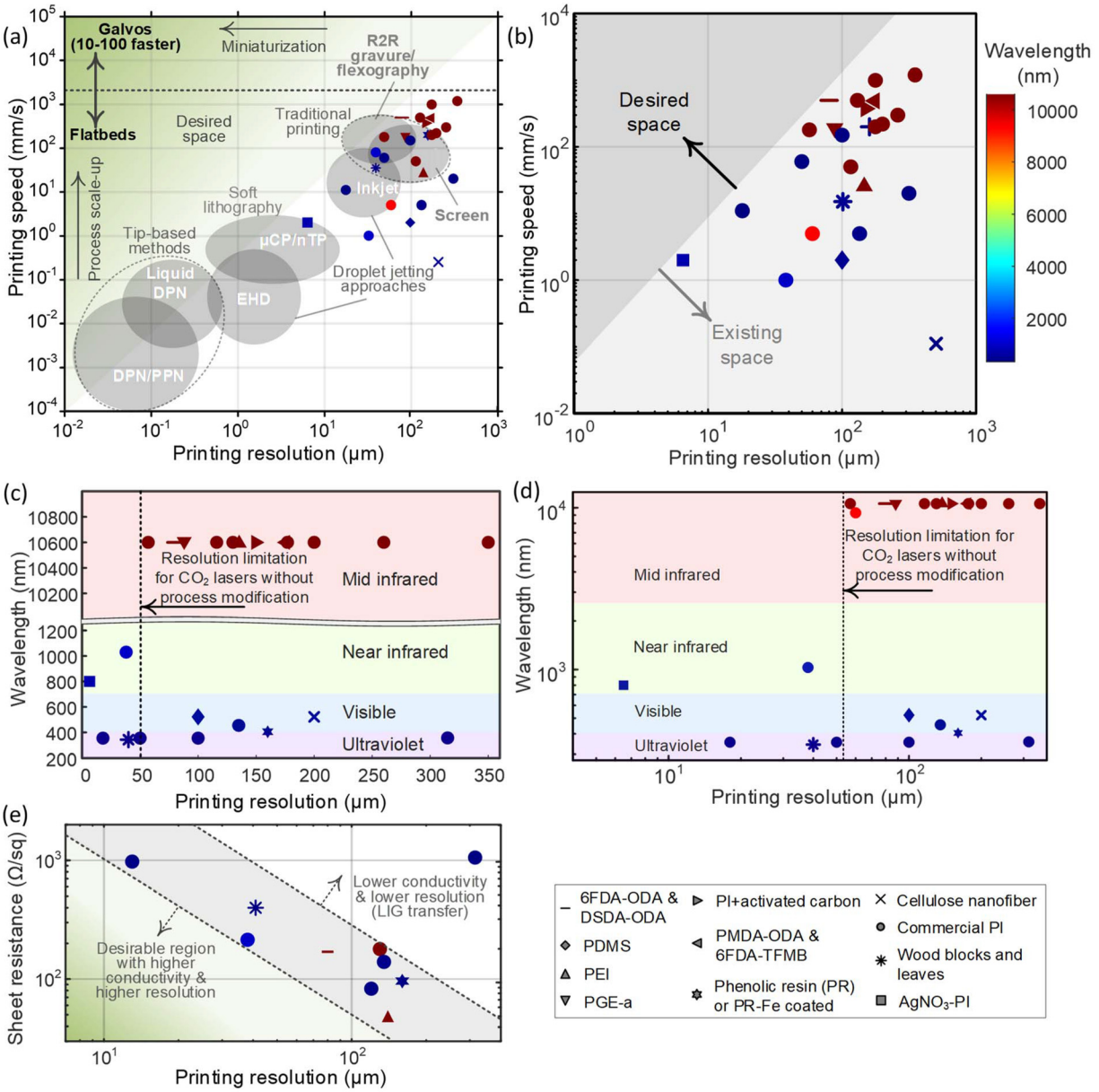


**Fig. 15** Throughput–resolution–performance trade-offs. (a) A plot of printing speed (representing throughput) and printing resolution across various advanced manufacturing techniques, highlighting the typical trade-off that exists with state-of-the-art technologies. Results for LIG are also mapped on the same plot with different colors for laser wavelengths, demonstrating that LIG is already exceeding printing techniques in terms of throughput, albeit with larger feature size. The throughput–resolution benchmarks for all non-LIG manufacturing techniques are obtained from refs. 210–246. (b) A similar plot to the one in (a), but with a smaller range of speed and resolution than (a), illustrating the contrast between the existing and desired operational space for high-throughput, high-resolution LIG electrode fabrication. (c) A plot of laser wavelength *vs.* printing resolution for the same LIG results presented in (a) and (b), illustrating the fundamental resolution limits imposed by longer-wavelength lasers, particularly $CO_2$ lasers. (d) Log–log version of the same plot in (c). (e) Variation of sheet resistance as a function of printing resolution, revealing the trade-off between conductivity and resolution in LIG structures, where higher resolutions typically correspond to increased sheet resistance. The literature-derived benchmarks for all LIG resolution–performance trade-offs are listed in Table S2.


This journal is © The Royal Society of Chemistry 2026

Open Access Article. Published on 09 February 2026. Downloaded on 5/23/2026 3:06:13 AM. This article is licensed under a Creative Commons Attribution 3.0 Unported Licence.

conditions on PI. It is worth noting that even finer resolution can be obtained by using lithography followed by $CO_2$ laser irradiation, but these results cannot be compared to true direct-write LIG. While lithography-based methods enable submicron resolution, they require multi-step processing, making them less favorable for scalable manufacturing. Without process modifications, the smallest resolution is reported to be 18 μm using a 355 nm UV laser at 11 mm $s^{-1}$, emphasizing the critical role of laser wavelength in defining resolution limits.[205] Fig. 15(c) demonstrates that longer wavelengths, particularly $CO_2$ lasers, impose fundamental resolution limits, whereas shorter wavelengths (UV and near-IR) enable finer feature sizes. Fig. 15(d) also demonstrates the same data but on a log–log scale. The predominance of $CO_2$ lasers for LIG formation is notable, but their inability to be miniaturized necessitates the use of alternative wavelengths for improved resolution. The data presented in Fig. 15(a and b) highlight a gap in current capabilities, particularly in the top left region of the operational space, indicating an opportunity for advancements in achieving both high-resolution features and faster fabrication speeds.

### 4.2. Ultrafast processing and resolution–conductivity trade-off

As long as sufficient fluence is provided, LIG can be fabricated at high speeds, presenting a pathway for scalable production. However, kinetics may play a significant role in simultaneously achieving high resolution and throughput, an aspect requiring further investigation. To further improve structural resolution, femtosecond (fs) lasers are a preferred option due to their ability to manipulate electron dynamics through temporal or spatial shaping.[206] For example, fs laser processing with temporal shaping has enabled the fabrication of $MoS_2$-based microsupercapacitors with a submicron resolution of approximately 800 nm.[207] However, the low repetition rate and short pulse width of fs lasers result in an insufficient photothermal effect, making it challenging to convert PI into conductive graphene structures.[208] Recently, LIG was combined with a toner, printing on only a subset of the substrate prior to lasing, in order to initiate LIG formation on either the top or bottom surfaces of a polymer film, resulting in miniaturization of LIG down to less than 40 μm line width, while maintaining low resistivity, and high electrochemical detection sensitivity.[154]

Various laser systems used for LIG fabrication typically yield sheet resistances between 50 and 1000 Ω $sq^{-1}$, depending on the processing parameters for single lines. The crystallinity and conductivity of LIG vary depending on the precursor material and processing conditions. For instance, when PEI is used as a precursor with a $CO_2$ laser, the sheet resistance is 50 Ω $sq^{-1}$ for a line width of 140 microns.[79] In contrast, wood-based precursors can achieve a finer resolution of 40 microns but exhibit a higher sheet resistance of approximately 400 Ω $sq^{-1}$.[109] Fig. 15(e) illustrates that higher resolution corresponds to increased sheet resistance, limiting applications in scenarios demanding low electrical resistance. Additionally, transfer-based approaches achieve feature sizes of roughly 300 microns but exhibit high sheet resistances.[209] Thus, the miniaturization of LIG raises concerns regarding the quality of the lines generated. While thinner lines exhibit higher resistance due to reduced graphitization, there is an unoccupied desirable space in the resolution–conductivity spectrum, as illustrated in Fig. 15(c), indicating the need for process optimizations to achieve low sheet resistance at smaller feature sizes. Addressing this gap could lead to advancements in LIG fabrication that balance resolution, conductivity, and scalability.

## 5. Conclusion and outlook

This paper reviews the extensive range of carbon precursors utilized in the fabrication of LIG, highlighting their diverse chemical compositions, fabrication methods, and resulting properties. The selection of an appropriate carbon precursor plays a crucial role in determining the final morphology, electrical conductivity, and structural integrity of LIG, making chemistry and morphology control essential aspects of material optimization. A broad spectrum of synthetic polymers, natural derivatives, and fossil-based products have been investigated as LIG precursors, each offering distinct advantages and challenges. To align with environmental sustainability goals, significant efforts have been made to explore bio-based materials such as cellulose, lignin, and chitosan, which provide renewable and eco-friendly alternatives to conventional synthetic polymers. Various strategies have been employed to modify the precursors before laser scribing, including heteroatom doping, integration of nanofillers, and the incorporation of functional materials, which improve LIG's electrical, electrochemical, and catalytic properties. Additionally, multilayer structuring has been explored as a design strategy to enhance LIG-based applications, allowing for improved device performance and functionality. Post-processing techniques such as secondary laser scribing, 3D printing, and transfer methods have further been investigated to enhance the mechanical stability, flexibility, and adaptability of LIG for various real-world applications. Furthermore, this paper examines the throughput–resolution–performance trade-off limiting the scalability of LIG manufacturing. This perspective required the relationship between laser parameters (such as speed, power, and line width) and the structural quality of the resulting graphene to be analyzed. By compiling these findings, this review provides a comprehensive overview of LIG synthesis, offering insights into material selection, process optimization, and potential industrial applications.

Despite significant advancements in the fabrication and application of LIG, several critical gaps remain in this field. In particular, we have identified the following knowledge gaps that require further research.

### 5.1. Gap 1: need for hypothesis-driven design of precursors

One major limitation is the lack of a comprehensive and systematic investigation of the influence of the molecular structure of diverse polymer precursors on the crystallinity, surface

Open Access Article. Published on 09 February 2026. Downloaded on 5/23/2026 3:06:13 AM.
This article is licensed under a Creative Commons Attribution 3.0 Unported Licence.

chemistry, morphology, and electrical/electrochemical properties of the resulting graphene. While a variety of synthetic and bio-based precursors have been explored, systematic studies that examine the molecular structure–property relationships in LIG formation are still scarce. Key questions remain unanswered, such as which specific ring structures in polymer precursors yield the highest degree of graphitization, how different heteroatoms influence electrical, electrochemical, and catalytic properties, and whether the conformation and chain length of polymer precursors play a role in determining the structural quality of LIG. Without a more diverse and well-controlled selection of carbon precursors, it is challenging to establish clear design principles for optimizing LIG synthesis at the molecular level.

Additionally, there is a lack of studies on copolymers containing polymer chains with more than three repeat units, aside from BCPs. For instance, researchers can manipulate the relative ratio of two groups of PI precursors (diamine and dianhydride) to tailor the thermal properties of the resulting material. Moreover, incorporating functional polymers or active groups into a polymer matrix offers a promising route to achieving desired properties and performance. However, current research efforts in this direction remain limited, leaving significant potential for further exploration of the role of copolymer architectures in LIG synthesis.

### 5.2. Gap 2: uncertainty of the mechanism of conversion to LIG

Another critical gap in the field is the lack of *in situ* characterization techniques that can provide real-time insights into the transformation process from precursor materials to LIG. Currently, most studies rely on post-fabrication characterization methods such as Raman spectroscopy, X-ray photoelectron spectroscopy (XPS), and scanning electron microscopy (SEM) to analyze the final LIG product. However, the underlying mechanism of $sp^2$ carbon formation during laser irradiation remains largely unknown due to the absence of real-time analytical tools. The implementation of *in situ* Raman spectroscopy, gas chromatography–mass spectrometry (GC/MS), or high-speed thermal imaging could enable researchers to track the structural evolution of carbon precursors under laser irradiation, identify transient intermediates, and clarify the roles of temperature, pressure, and reaction kinetics in LIG synthesis. Understanding these dynamic processes is essential for refining LIG fabrication techniques and optimizing laser parameters to achieve better control over material properties.

### 5.3. Gap 3: need for holistic LCA for evaluation

Furthermore, while many studies have demonstrated the feasibility of growing LIG on bio-based materials, there is a lack of systematic evaluation regarding the sustainability of these precursors. Current research primarily focuses on proving that LIG can be derived from renewable sources such as cellulose, lignin, and chitosan, but few studies have assessed the actual environmental impact of these materials through life cycle analysis (LCA) or carbon footprint evaluation. The assumption that bio-based materials are inherently sustainable remains largely unverified without quantitative comparisons of energy consumption, carbon emissions, and waste generation during LIG fabrication. A more rigorous examination of these factors is necessary to determine whether bio-based LIG production offers a truly eco-friendly alternative to traditional graphene synthesis methods.

### 5.4. How to fill the scientific knowledge gaps

To address these gaps, future research needs to focus on expanding the range of polymer precursors studied for LIG fabrication, with systematic investigations into how molecular structures, heteroatom doping, and polymer conformations influence the crystallinity and electrical conductivity of the resulting graphene. Developing computational models and machine learning approaches for predicting the graphitization potential of different carbon precursors could accelerate material discovery and optimization. Additionally, the integration of *in situ* characterization techniques, such as real-time Raman spectroscopy and GC/MS, will be crucial for unraveling the underlying mechanisms of carbon conversion during laser irradiation. These techniques will provide a deeper understanding of the reaction pathways, enabling precise control over LIG morphology and properties. Finally, a comprehensive assessment of the sustainability of bio-based LIG precursors is necessary to validate their environmental benefits. Life cycle assessments (LCAs) and carbon footprint analyses should be conducted to quantify energy consumption, emissions, and material efficiency across different precursor types and processing conditions. By addressing these challenges, future studies can establish clearer design principles for LIG synthesis, improve fabrication precision, and ensure the long-term viability of sustainable graphene production.

## Conflicts of interest

There are no conflicts to declare.

## Data availability

No primary research results, software or code have been included and no new data were generated or analysed as part of this review.

Supplementary information (SI) is available. The supplementary information (SI) include the following: A tabulated summary of the literature of laser-induced graphene (LIG) fabricated on different precursors; A literature-derived dataset compiling resolution-performance benchmarks for LIG fabricated on different precursors. See DOI: https://doi.org/10.1039/d5nr04319k.

## Acknowledgements

This research was supported by the National Science Foundation (NSF) under award number 2239244 (any

 This journal is © The Royal Society of Chemistry 2026

opinions, findings, and conclusions or recommendations expressed in this material are those of the author(s) and do not necessarily reflect the views of the National Science Foundation). Work was also supported by the Department of Mechanical Engineering and Materials Science at the University of Pittsburgh. The authors are also thankful to useful input from Dr Moataz Abdulhafez (previously at the University of Pittsburgh).

Open Access Article. Published on 09 February 2026. Downloaded on 5/23/2026 3:06:13 AM. This article is licensed under a Creative Commons Attribution 3.0 Unported Licence.

## References

1 C. Lee, X. Wei, J. W. Kysar and J. Hone, *Science*, 2008, **321**, 385–388.
2 L. A. Falkovsky, *J. Phys.: Conf. Ser.*, 2008, **129**, 012004.
3 A. A. Balandin, S. Ghosh, W. Bao, I. Calizo, D. Teweldebrhan, F. Miao and C. N. Lau, *Nano Lett.*, 2008, **8**, 902–907.
4 A. H. Castro Neto, F. Guinea, N. M. R. Peres, K. S. Novoselov and A. K. Geim, *Rev. Mod. Phys.*, 2009, **81**, 109–162.
5 S. Engelhardt, in *Laser Technology in Biomimetics: Basics and Applications*, ed. V. Schmidt and M. R. Belegratis, Springer, Berlin, Heidelberg, 2013, pp. 13–65.
6 L. Chai, J. Wang, H. Wang, L. Zhang, W. Yu and L. Mai, *Nano Energy*, 2015, **17**, 224–232.
7 X. Liu, C. Tang, X. Du, S. Xiong, S. Xi, Y. Liu, X. Shen, Q. Zheng, Z. Wang, Y. Wu, A. Horner and J. K. Kim, *Mater. Horiz.*, 2017, **4**, 477–486.
8 A. Idowu, B. Boesl and A. Agarwal, *Carbon*, 2018, **135**, 52–71.
9 Z. Zhang, H. Zhu, W. Zhang, Z. Zhang, J. Lu, K. Xu, Y. Liu and V. Saetang, *Carbon*, 2023, **214**, 118356.
10 R. Ye, D. K. James and J. M. Tour, *Adv. Mater.*, 2019, **31**, 1803621.
11 J. Hayashi, H. Mizuta, M. Yamamoto, K. Kusakabe and S. Morooka, *J. Membr. Sci.*, 1997, **124**, 243–251.
12 J. Lin, Z. Peng, Y. Liu, F. Ruiz-Zepeda, R. Ye, E. L. G. Samuel, M. J. Yacaman, B. I. Yakobson and J. M. Tour, *Nat. Commun.*, 2014, **5**, 5714.
13 L. X. Duy, Z. Peng, Y. Li, J. Zhang, Y. Ji and J. M. Tour, *Carbon*, 2018, **126**, 472–479.
14 Y. Wang, Y. Wang, P. Zhang, F. Liu and S. Luo, *Small*, 2018, **14**, 1802350.
15 L. Huang, S. Xu, Z. Wang, K. Xue, J. Su, Y. Song, S. Chen, C. Zhu, B. Z. Tang and R. Ye, *ACS Nano*, 2020, **14**, 12045–12053.
16 L. Cheng, W. Guo, X. Cao, Y. Dou, L. Huang, Y. Song, J. Su, Z. Zeng and R. Ye, *Mater. Chem. Front.*, 2021, **5**, 4874–4891.
17 H. Wang, Z. Zhao, P. Liu and X. Guo, *Theor. Appl. Mech. Lett*, 2021, **11**, 100240.
18 Y. Wang, G. Wang, M. He, F. Liu, M. Han, T. Tang and S. Luo, *Small*, 2021, **17**, 2103322.
19 J. Chen, Y. Wang, F. Liu and S. Luo, *ACS Appl. Mater. Interfaces*, 2020, **12**, 23284–23297.
20 L. Wang, Z. Wang, A. N. Bakhtiyari and H. Zheng, *Micromachines*, 2020, **11**, 1–9.
21 Y. Dong, S. C. Rismiller and J. Lin, *Carbon*, 2016, **104**, 47–55.
22 F. J. Romero, A. Salinas-Castillo, A. Rivadeneyra, A. Albrecht, A. Godoy, D. P. Morales and N. Rodriguez, *Nanomaterials*, 2018, **8**, 517.
23 J. Lim, S. Park, H. Cho, Y. Lee, I. H. Ha, Y. Kim, E. Hwang, H. Lee, J. Shin, J. Kwon, S. H. Ko and S. Hong, *Chem. Eng. J.*, 2022, **428**, 131050.
24 D. J. Krajnovich and J. E. Vázquez, *J. Appl. Phys.*, 1993, **73**, 3001–3008.
25 A. Vashisth, M. Kowalik, J. C. Gerringer, C. Ashraf, A. C. T. Van Duin and M. J. Green, *ACS Appl. Nano Mater.*, 2020, **3**, 1881–1890.
26 E. R. Mamleyev, S. Heissler, A. Nefedov, P. G. Weidler, N. Nordin, V. V. Kudryashov, K. Länge, N. MacKinnon and S. Sharma, *npj Flexible Electron.*, 2019, **3**, 2.
27 R. Ye, D. K. James and J. M. Tour, *Acc. Chem. Res.*, 2018, **51**, 1609–1620.
28 S. O. Pereira, N. F. Santos, A. F. Carvalho, A. J. S. Fernandes and F. M. Costa, *Nanomaterials*, 2021, **11**, 1893.
29 M. Abdulhafez, G. N. Tomaraei and M. Bedewy, *ACS Appl. Nano Mater.*, 2021, **4**, 2973–2986.
30 J. T. Li, K. M. Wyss, W. Chen, J. Chen, B. Deng, J. L. Beckham, P. A. Advincula, P. E. Savas, V. D. Li, O. Jin and J. M. Tour, *Carbon*, 2023, **215**, 118494.
31 M. Abdulhafez, G. N. Tomaraei and M. Bedewy, *Carbon*, 2026, **246**, 120941.
32 M. Liu, J. N. Wu and H. Y. Cheng, *Sci. China: Technol. Sci.*, 2021, **65**, 41–52.
33 Y. Chyan, R. Ye, Y. Li, S. P. Singh, C. J. Arnusch and J. M. Tour, *ACS Nano*, 2018, **12**, 2176–2183.
34 M. Sahaluddin, M. Li, M. Zarei, P. W. Leu and M. Bedewy, *ACS Appl. Eng. Mater.*, 2025, DOI: 10.1021/acsaenm.5c00861.
35 M. Abdulhafez, A. J. McComb and M. Bedewy, *J. Micro Nano-Manuf.*, 2020, **8**, 031006.
36 K.-H. Nam, M. Abdulhafez, G. Najaf Tomaraei and M. Bedewy, *Appl. Surf. Sci.*, 2022, **574**, 151339.
37 M. Abdulhafez, E. Castagnola, M. Sahaluddin, G. Baglieri, G. N. Tomaraei, S. Ghosh, X. T. Cui and M. Bedewy, *ACS Appl. Mater. Interfaces*, 2025, **18**, 613–628.
38 J. L. Beckham, J. T. Li, M. G. Stanford, W. Chen, E. A. McHugh, P. A. Advincula, K. M. Wyss, Y. Chyan, W. L. Boldman, P. D. Rack and J. M. Tour, *ACS Nano*, 2021, **15**, 8976–8983.
39 P. Chen, Y. Xin, H. Zu, X. Yang, H. Feng, W. Xu, Y. Chang, Z. Chen, W. Qian, Y. Lv, H. Fu, L. Ren and D. He, *Nano Res.*, 2025, **18**, 94908018.
40 S. Kaur, D. Mager, J. G. Korvink and M. Islam, *Mater. Sci. Energy Technol.*, 2021, **4**, 407–412.
41 H. D. Wotton, R. Tutika, J. W. Will, D. H. Ho, M. D. Bartlett, T. E. Long and C. B. Williams, *Adv. Mater. Technol.*, 2025, **10**, 70035.

Open Access Article. Published on 09 February 2026. Downloaded on 5/23/2026 3:06:13 AM. This article is licensed under a Creative Commons Attribution 3.0 Unported Licence.

42 Q. Zhang, F. Zhang, X. Liu, Z. Yue, X. Chen and Z. Wan, *Adv. Mater. Technol.*, 2023, **8**, 2300244.
43 P. I. Pedro, T. Pinheiro, S. L. Silvestre, A. C. Marques, J. Coelho, J. M. Marconcini, E. Fortunato, L. H. Luiz and R. Martins, *Appl. Phys. Rev.*, 2022, **9**, 41305.
44 K. Avinash and F. Patolsky, *Mater. Today*, 2023, **70**, 104–136.
45 S. Bai, L. Ruan, H. Chen, Y. Du, H. Deng, N. Dai and Y. Tang, *Chem. Eng. J.*, 2024, **493**, 152805.
46 J. C. Gerringer, A. G. Moran, T. Habib, M. J. Pospisil, J. H. Oh, B. R. Teipel and M. J. Green, *ACS Appl. Nano Mater.*, 2019, **2**, 7032–7042.
47 H. Liu, Y. Xie, J. Liu, K.-s. Moon, L. Lu, Z. Lin, W. Yuan, C. Shen, X. Zang, L. Lin, Y. Tang and C. P. Wong, *Chem. Eng. J.*, 2020, **393**, 124672.
48 A. F. Carvalho, A. J. S. Fernandes, C. Leitão, J. Deuermeier, A. C. Marques, R. Martins, E. Fortunato and F. M. Costa, *Adv. Funct. Mater.*, 2018, **28**, 1805271.
49 H. Liu, Y. Zheng, K. S. Moon, Y. Chen, D. Shi, X. Chen and C. P. Wong, *Nano Energy*, 2022, **94**, 106902.
50 A. Adel, A. Barker, E. F. Bleaney, B. Loubser, J. H. N. Coggeshall, N. D. Saier, E. L. Cross, P. C. Daniels, F. Dennison, D. M. Dennison, D. M. Goody, R. M. Robinson, G. D. Strong, J. Watanabe, R. Thorndike, A. M. Wells and A. J. Wilson, *Proc. R. Soc. London, Ser. A*, 1951, **209**, 196–218.
51 P. Ouzilleau, A. E. Gheribi, P. Chartrand, G. Soucy and M. Monthioux, *Carbon*, 2019, **149**, 419–435.
52 K. R. Brown, T. M. Harrell, L. Skrzypczak, A. Scherschel, H. F. Wu and X. Li, *Carbon*, 2022, **196**, 422–439.
53 Y. Li, D. X. Luong, J. Zhang, Y. R. Tarkunde, C. Kittrell, F. Sargunaraj, Y. Ji, C. J. Arnusch and J. M. Tour, *Adv. Mater.*, 2017, **29**, 1700496.
54 M. Qu, Y. Guo, Y. Cai, Z. Nie and C. Zhang, *Small*, 2024, **20**, 2310273.
55 P. Smith, A. G. Obando, A. Griffin, M. Robertson, E. Bounds and Z. Qiang, *Adv. Mater.*, 2023, **35**, 2208029.
56 G. Li, W.-C. Law and K. C. Chan, *Green Chem.*, 2018, **20**, 3689–3695.
57 S. Jeong, Y. Kwon, C. Park, Y. Ito, J. Park, M. S. Hwang, J. Chung and N. Sugita, *Nano Energy*, 2024, **126**, 109663.
58 M. Burke, C. Larrigy, E. Vaughan, G. Paterakis, L. Sygellou, A. J. Quinn, G. Herzog, C. Galiotis and D. Iacopino, *ACS Omega*, 2020, **5**, 1540–1548.
59 L. F. Mendes, A. de Siervo, W. Reis de Araujo and T. R. Longo Cesar Paixão, *Carbon*, 2020, **159**, 110–118.
60 J. Liu, L. Zhang, C. Yang and S. Tao, *J. Mater. Chem. A*, 2019, **7**, 21168–21175.
61 C. Ma, Z. Ma, L. Gao, Y. Liu, T. Wu, F. Wang and H. Ishida, *Mater. Des.*, 2019, **180**, 107954.
62 J. Wang, N. Wang, D. Xu, L. Tang and B. Sheng, *Sens. Actuators, B*, 2023, **375**, 132846.
63 R. Ye, X. Han, D. V. Kosynkin, Y. Li, C. Zhang, B. Jiang, A. A. Martí and J. M. Tour, *ACS Nano*, 2018, **12**, 1083–1088.
64 Y. J. Kim, D. Yang, H. K. Nam, T. S. D. Le, Y. Lee and S. Kwon, *CIRP Ann.*, 2022, **71**, 473–476.
65 H. Wang, H. Wang, Y. Wang, X. Su, C. Wang, M. Zhang, M. Jian, K. Xia, X. Liang, H. Lu, S. Li and Y. Zhang, *ACS Nano*, 2020, **14**, 3219–3226.
66 Y. Zhu, H. Cai, H. Ding, N. Pan and X. Wang, *ACS Appl. Mater. Interfaces*, 2019, **11**, 6195–6200.
67 P. Zaccagnini, C. Ballin, M. Fontana, M. Parmeggiani, S. Bianco, S. Stassi, A. Pedico, S. Ferrero and A. Lamberti, *Adv. Mater. Interfaces*, 2021, **8**, 2101046.
68 Y. Chen, J. Long, S. Zhou, D. Shi, Y. Huang, X. Chen, J. Gao, N. Zhao and C.-P. Wong, *Small Methods*, 2019, **3**, 1900208.
69 R. Murray, M. Burke, D. Iacopino and A. J. Quinn, *ACS Omega*, 2021, **6**, 16736–16743.
70 A. Samouco, A. C. Marques, A. Pimentel, R. Martins and E. Fortunato, *Flexible Printed Electron.*, 2018, **3**, 044002.
71 P. Nayak, N. Kurra, C. Xia and H. N. Alshareef, *Adv. Electron. Mater.*, 2016, **2**, 1600185.
72 M. Yuan, F. Luo, Z. Wang, H. Li, Y. Rao, J. Yu, Y. Wang, D. Xie, X. Chen and C. P. Wong, *ACS Appl. Mater. Interfaces*, 2021, **13**, 22426–22437.
73 K. H. Nam, M. Abdulhafez, E. Castagnola, G. N. Tomaraei, X. T. Cui and M. Bedewy, *Carbon*, 2022, **188**, 209–219.
74 A. Iqbal, B. Amna, I. ul Islam, Z. Yuchi, H. M. Siddiqi, J. Zai and X. Qian, *Polymer*, 2025, **319**, 128016.
75 R. Gupta, H. Ali and N. Verma, *Microchem. J.*, 2024, **199**, 109984.
76 R. Gupta, T. Santra, S. K. Misra and N. Verma, *Microchem. J.*, 2024, **207**, 111895.
77 L. Ge, Q. Hong, H. Li, C. Liu and F. Li, *Adv. Funct. Mater.*, 2019, **29**, 1904000.
78 S. P. Singh, Y. Li, J. Zhang, J. M. Tour and C. J. Arnusch, *ACS Nano*, 2018, **12**, 289–297.
79 M. Tavakkoli Gilavan, M. S. Rahman, A. Minhas-Khan, S. Nambi and G. Grau, *ACS Appl. Electron. Mater.*, 2021, **3**, 3867–3875.
80 X. Dai, J. Wu, Z. Qian, H. Wang, J. Jian, Y. Cao, M. H. Rummeli, Q. Yi, H. Liu and G. Zou, *Sci. Adv.*, 2016, **2**, e1601574.
81 S. H. Kim, M. A. Khan, K. S. Im, P. Kang and S. Y. Nam, *Adv. Mater. Interfaces*, 2024, **11**, 2400490.
82 L. Cao, S. Zhu, B. Pan, X. Dai, W. Zhao, Y. Liu, W. Xie, Y. Kuang and X. Liu, *Carbon*, 2020, **163**, 85–94.
83 Y. Peng, W. Zhao, F. Ni, W. Yu and X. Liu, *ACS Nano*, 2021, **15**, 19490–19502.
84 L. Yang, H. Ji, C. Meng, Y. Li, G. Zheng, X. Chen, G. Niu, J. Yan, Y. Xue, S. Guo and H. Cheng, *ACS Appl. Mater. Interfaces*, 2022, **14**, 17818–17825.
85 K. W. Tan, B. Jung, J. G. Werner, E. R. Rhoades, M. O. Thompson and U. Wiesner, *Science*, 2015, **349**, 54–58.
86 H. M. Jin, S. H. Lee, J. Y. Kim, S. W. Son, B. H. Kim, H. K. Lee, J. H. Mun, S. K. Cha, J. S. Kim, P. F. Nealey, K. J. Lee and S. O. Kim, *ACS Nano*, 2016, **10**, 3435–3442.
87 A. Lamberti, M. Serrapede, G. Ferraro, M. Fontana, F. Perrucci, S. Bianco, A. Chiolerio and S. Bocchini, *2D Mater.*, 2017, **4**, 035012.

 This journal is © The Royal Society of Chemistry 2026

Open Access Article. Published on 09 February 2026. Downloaded on 5/23/2026 3:06:13 AM. This article is licensed under a Creative Commons Attribution 3.0 Unported Licence.

88 Z. Peng, R. Ye, J. A. Mann, D. Zakhidov, Y. Li, P. R. Smalley, J. Lin and J. M. Tour, *ACS Nano*, 2015, **9**, 5868–5875.
89 X. Hui, X. Xuan, J. Kim and J. Y. Park, *Electrochim. Acta*, 2019, **328**, 135066.
90 M. Dosi, I. Lau, Y. Zhuang, D. S. A. Simakov, M. W. Fowler and M. A. Pope, *ACS Appl. Mater. Interfaces*, 2019, **11**, 6166–6173.
91 M. Reina, A. Scalia, G. Auxilia, M. Fontana, F. Bella, S. Ferrero and A. Lamberti, *Adv. Sustainable Syst.*, 2022, **6**, 2100228.
92 I. Lawan, P. Luengrojanakul, K. Charoensuk, H. Argunam, C. H. Ahn and S. Rimdusit, *Nanoscale Adv.*, 2024, **6**, 1556–1564.
93 A. Z. Yazdi, I. O. Navas, A. Abouelmagd and U. Sundararaj, *Macromol. Rapid Commun.*, 2017, **38**, 1700176.
94 R. Ye, Z. Peng, T. Wang, Y. Xu, J. Zhang, Y. Li, L. G. Nilewski, J. Lin and J. M. Tour, *ACS Nano*, 2015, **9**, 9244–9251.
95 Y. Zhang, H. Zhu, P. Sun, C.-K. Sun, H. Huang, S. Guan, H. Liu, H. Zhang, C. Zhang and K.-R. Qin, *Electroanalysis*, 2019, **31**, 1334–1341.
96 W. Yang, Y. Liu, Q. Li, J. Wei, X. Li, Y. Zhang and J. Liu, *RSC Adv.*, 2020, **10**, 23953–23958.
97 J. Cai, C. Lv, C. Hu, J. Luo, S. Liu, J. Song, Y. Shi, C. Chen, Z. Zhang, S. Ogawa, E. Aoyagi and A. Watanabe, *Energy Storage Mater.*, 2020, **25**, 404–415.
98 S. Y. Kim, J. H. Kim, K. N. Kim, H. Oh, S. Myung and D. H. Kim, *Sci. Rep.*, 2024, **14**, 4599.
99 M. Parmeggiani, P. Zaccagnini, S. Stassi, M. Fontana, S. Bianco, C. Nicosia, C. F. Pirri and A. Lamberti, *ACS Appl. Mater. Interfaces*, 2019, **11**, 33221–33230.
100 M. Han, M. He, G. Wang and S. Luo, *J. Power Sources*, 2021, **514**, 230579.
101 E. Vaughan, C. Santillo, A. Imbrogno, G. Gentile, A. J. Quinn, S. Kaciulis, M. Lavorgna and D. Iacopino, *ACS Sustainable Chem. Eng.*, 2023, **11**, 13574–13583.
102 A. Kothuru and S. Goel, *Flexible Printed Electron.*, 2020, **5**, 042001.
103 M. Sopronyi, F. Sima, C. Vaulot, L. Delmotte, A. Bahouka and C. M. Ghimbeu, *Sci. Rep.*, 2016, **6**, 39617.
104 J. Liu, G. Yang, K. Lu, C. Ye, Y. Ma and J. Ye, *Electrochim. Acta*, 2024, **474**, 143505.
105 W. Yang, Y. Liu, J. Wei, X. Li, N. Li and J. Liu, *Polymers*, 2021, **12**, 984.
106 C. Yu, W. Yang, F. Meng, Z. Zhao, F. Cao, C. Xing and J. Du, *Sci. Eng. Compos. Mater.*, 2024, **31**, DOI: 10.1515/secm-2022-0234.
107 M. Qu, Y. Guo, Y. Cai, Z. Nie and C. Zhang, *Small*, 2024, **20**, 2310273.
108 B. Kulyk, B. F. R. Silva, A. F. Carvalho, S. Silvestre, A. J. S. Fernandes, R. Martins, E. Fortunato and F. M. Costa, *ACS Appl. Mater. Interfaces*, 2021, **13**, 10210–10221.
109 T.-S. D. Le, S. Park, J. An, P. S. Lee and Y.-J. Kim, *Adv. Funct. Mater.*, 2019, **29**, 1902771.
110 X. Han, R. Ye, Y. Chyan, T. Wang, C. Zhang, L. Shi, T. Zhang, Y. Zhao and J. M. Tour, *ACS Appl. Nano Mater.*, 2018, **1**, 5053–5061.
111 M. G. Stanford, J. T. Li, Y. Chyan, Z. Wang, W. Wang and J. M. Tour, *ACS Nano*, 2019, **13**, 7166–7174.
112 T.-S. D. Le, Y. A. Lee, H. K. Nam, K. Y. Jang, D. Yang, B. Kim, K. Yim, S.-W. Kim, H. Yoon and Y.-J. Kim, *Adv. Funct. Mater.*, 2022, **32**, 2107768.
113 Y. Steksova, A. C. Bressi, M. Galliani, A. Marino, G. Ciofani, E. Machado-Charry, H. G. Bernal, A. Francini, L. Sebastiani and F. Greco, *Adv. Funct. Mater.*, 2025, DOI: 10.1002/adfm.202507462.
114 R. Ye, Y. Chyan, J. Zhang, Y. Li, X. Han, C. Kittrell and J. M. Tour, *Adv. Mater.*, 2017, **29**, 1702211.
115 F. Mahmood, C. Zhang, Y. Xie, D. Stalla, J. Lin and C. Wan, *RSC Adv.*, 2019, **9**, 22713–22720.
116 W. Zhang, Y. Lei, F. Ming, Q. Jiang, P. M. F. J. Costa and H. N. Alshareef, *Adv. Energy Mater.*, 2018, **8**, 1801840.
117 Y. Lei, A. H. Alshareef, W. Zhao and S. Inal, *ACS Appl. Nano Mater.*, 2020, **3**, 1166–1174.
118 A. Ghavipanjeh and S. Sadeghzadeh, *Sci. Rep.*, 2024, **14**, 4475.
119 W. R. de Araujo, C. M. R. Frasson, W. A. Ameku, J. R. Silva, L. Angnes and T. R. L. C. Paixão, *Angew. Chem., Int. Ed.*, 2017, **56**, 15113–15117.
120 B. Kulyk, M. Matos, B. F. R. Silva, A. F. Carvalho, A. J. S. Fernandes, D. V. Evtuguin, E. Fortunato and F. M. Costa, *Diamond Relat. Mater.*, 2022, **123**, 108855.
121 Y. Yao, X. Duan, M. Niu, J. Luo, R. Wang and T. Liu, *Cellulose*, 2019, **26**, 7423–7435.
122 B. Kulyk, B. F. R. Silva, A. F. Carvalho, P. Barbosa, A. V. Girão, J. Deuermeier, A. J. S. Fernandes, F. M. L. Figueiredo, E. Fortunato and F. M. Costa, *Adv. Mater. Technol.*, 2022, **7**, 2101311.
123 X. Zang, C. Shen, Y. Chu, B. Li, M. Wei, J. Zhong, M. Sanghadasa and L. Lin, *Adv. Mater.*, 2018, **30**, 1800062.
124 T. Pinheiro, S. Silvestre, J. Coelho, A. C. Marques, R. Martins, M. G. F. Sales and E. Fortunato, *Adv. Mater. Interfaces*, 2021, **8**, 2101502.
125 R. Ren, Y. Zhong, X. Ren and Y. Fan, *RSC Adv.*, 2022, **12**, 25807–25814.
126 M. Yuan, Z. Wang, Y. Rao, Y. Wang, B. Gao, J. Yu, H. Li and X. Chen, *Carbon*, 2023, **202**, 296–304.
127 Q. M. Huang, H. Yang, S. Wang, X. Liu, C. Tan, A. Luo, S. Xu, G. Zhang and H. Ye, *ACS Appl. Nano Mater.*, 2023, **6**, 10453–10465.
128 S. T. Sankaran, A. Dallinger, A. C. Bressi, A. Marino, G. Ciofani, A. Szkudlarek, V. Bilovol, K. Sokolowski, B. Kunert, H. K. Hampel, H. G. Bernal and F. Greco, *Small*, 2024, **20**, 2405252.
129 G. F. Hawes, D. Yilman, B. S. Noremberg and M. A. Pope, *ACS Appl. Nano Mater.*, 2019, **2**, 6312–6324.
130 J. Sha, Y. Li, R. Villegas Salvatierra, T. Wang, P. Dong, Y. Ji, S. K. Lee, C. Zhang, J. Zhang, R. H. Smith, P. M. Ajayan, J. Lou, N. Zhao and J. M. Tour, *ACS Nano*, 2017, **11**, 6860–6867.

Open Access Article. Published on 09 February 2026. Downloaded on 5/23/2026 3:06:13 AM. This article is licensed under a Creative Commons Attribution 3.0 Unported Licence.

131 Z. Li, L. Lu, Y. Xie, W. Wang, Z. Lin, B. Tang and N. Lin, *Adv. Eng. Mater.*, 2021, **23**, 2100195.
132 M. K. M. Abd-Elbaki, T. M. Ragab, N. E. R. Ismael and A. S. G. Khalil, *RSC Adv.*, 2023, **13**, 31704–31719.
133 T. Nakajima and Y. Matsuo, *Carbon*, 1994, **32**, 469–475.
134 R. Trusovas, G. Račiukaitis, J. Barkauskas and R. Mažeikienė, *J. Laser Micro/Nanoeng.*, 2012, **7**, 49–53.
135 D. A. Sokolov, K. R. Shepperd and T. M. Orlando, *J. Phys. Chem. Lett.*, 2010, **1**, 2633–2636.
136 C. Zhang, Y. Xie, C. Zhang and J. Lin, *Carbon*, 2019, **153**, 585–591.
137 X. Zang, N. Ferralis and J. C. Grossman, *ACS Nano*, 2022, **16**, 2101–2109.
138 X. Zang, C. Jian, S. Ingersoll, H. Li, J. J. Adams, Z. Lu, N. Ferralis and J. C. Grossman, *Sci. Adv.*, 2020, **6**, eaaz5231.
139 S. Wang, Y. Yu, R. Li, G. Feng, Z. Wu, G. Compagnini, A. Gulino, Z. Feng and A. Hu, *Electrochim. Acta*, 2017, **241**, 153–161.
140 L. Li, J. Zhang, Z. Peng, Y. Li, C. Gao, Y. Ji, R. Ye, N. D. Kim, Q. Zhong, Y. Yang, H. Fei, G. Ruan and J. M. Tour, *Adv. Mater.*, 2016, **28**, 838–845.
141 J. T. Li, M. G. Stanford, W. Chen, S. E. Presutti and J. M. Tour, *ACS Nano*, 2020, **14**, 7911–7919.
142 M. D. Wagh, H. Renuka, P. S. Kumar, K. Amreen, S. K. Sahoo and S. Goel, *IEEE Sens. J.*, 2022, **22**, 14620–14627.
143 R. Su, M. Liang, Y. Yuan, C. Huang, W. Xing, X. Bian, Y. Lian, B. Wang, Z. You and R. You, *Adv. Sci.*, 2024, **11**, 2404889.
144 J. Ji, Y. Wang, W. Zhao and G. Wang, *ACS Appl. Nano Mater.*, 2023, **6**, 23401–23409.
145 S. Deshmukh, K. Ghosh, M. Pykal, M. Otyepka and M. Pumera, *ACS Nano*, 2023, **17**, 20537–20550.
146 X.-Y. Fu, R.-Y. Shu, C.-J. Ma, Y.-Y. Zhang, H.-B. Jiang and M.-N. Yao, *Appl. Surf. Sci.*, 2023, **631**, 157549.
147 X.-Y. Fu, Y.-Y. Zhang, C.-J. Ma and H.-B. Jiang, *Opt. Lett.*, 2022, **47**, 1502–1505.
148 M. Yuan, F. Luo, Y. Rao, W. Ying, J. Yu, H. Li and X. Chen, *IEEE Electron Device Lett.*, 2022, **43**, 327–330.
149 J. Rodrigues, J. Zanoni, G. Gaspar, A. J. S. Fernandes, A. F. Carvalho, N. F. Santos, T. Monteiro and F. M. Costa, *Nanoscale Adv.*, 2019, **1**, 3252–3268.
150 Z. Zhang, M. Song, J. Hao, K. Wu, C. Li and C. Hu, *Carbon*, 2018, **127**, 287–296.
151 A. K. Thakur, S. P. Singh, M. N. Kleinberg, A. Gupta and C. J. Arnusch, *ACS Appl. Mater. Interfaces*, 2019, **11**, 10914–10921.
152 R. Barber, J. Davis and P. Papakonstantinou, *ACS Appl. Nano Mater.*, 2023, **6**, 10290–10302.
153 U. S. Jayapiriya, P. Rewatkar and S. Goel, *Int. J. Hydrogen Energy*, 2021, **46**, 3183–3192.
154 S. Ghosh, M. Sahaluddin, M. Abdulhafez, M. Y. Pwint, X. T. Cui and M. Bedewy, *Adv. Mater. Technol.*, 2025, e02433.
155 R. D. Rodriguez, S. Shchadenko, G. Murastov, A. Lipovka, M. Fatkullin, I. Petrov, T.-H. Tran, A. Khalelov, M. Saqib, N. E. Villa, V. Bogoslovskiy, Y. Wang, C.-G. Hu, A. Zinovyev, W. Sheng, J.-J. Chen, I. Amin and E. Sheremet, *Adv. Funct. Mater.*, 2021, **31**, 2008818.
156 Z. You, Q. Qiu, H. Chen, Y. Feng, X. Wang, Y. Wang and Y. Ying, *Biosens. Bioelectron.*, 2020, **150**, 111896.
157 F. Clerici, M. Fontana, S. Bianco, M. Serrapede, F. Perrucci, S. Ferrero, E. Tresso and A. Lamberti, *ACS Appl. Mater. Interfaces*, 2016, **8**, 10459–10465.
158 A. Chhetry, M. Sharifuzzaman, H. Yoon, S. Sharma, X. Xuan and J. Y. Park, *ACS Appl. Mater. Interfaces*, 2019, **11**, 22531–22542.
159 M. Cossutta, J. McKechnie and S. J. Pickering, *Green Chem.*, 2017, **19**, 5874–5884.
160 A. Costanzo, A. C. Bressi, M. Frey, F. Greco and M. Niero, *Int. J. Life Cycle Assess.*, 2025, **30**, 3018–3084.
161 R. Arvidsson, D. Kushnir, B. A. Sandén and S. Molander, *Environ. Sci. Technol.*, 2014, **48**, 4529–4536.
162 S. U. Hong, Y. Wang, L. S. Soh and W. F. Yong, *Green Chem.*, 2023, **25**, 4501–4512.
163 F. Foroughi, E. R. Ghomi, F. M. Dehaghi, R. Borayek and S. Ramakrishna, *Materials*, 2021, **14**(4), 714.
164 R. Arvidsson, D. Kushnir, S. Molander and B. A. Sandén, *J. Cleaner Prod.*, 2016, **132**, 289–297.
165 P. Serra and A. Piqué, *Adv. Mater. Technol.*, 2019, **4**, 1800099.
166 E. C. P. Smits, A. Walter, D. M. De Leeuw and K. Asadi, *Appl. Phys. Lett.*, 2017, **111**, 173101.
167 M. Praeger, S. Papazoglou, A. Pesquera, A. Zurutuza, A. Levi, D. Naveh, I. Zergioti, R. W. Eason and B. Mills, *Appl. Surf. Sci.*, 2020, **533**, 147488.
168 M. Cutroneo, V. Havranek, J. Flaks, P. Malinsky, L. Torrisi, L. Silipigni, P. Slepicka, D. Fajstavr and A. Mackova, *Coatings*, 2021, **11**, 1521.
169 K. Bhorkar, N. Samartzis, M. Athanasiou, L. Sygellou, N. Boukos, V. Dracopoulos, T. Ioannides and S. N. Yannopoulos, *npj 2D Mater. Appl.*, 2022, **6**, 56.
170 N. Samartzis, K. Bhorkar, M. Athanasiou, L. Sygellou, V. Dracopoulos, T. Ioannides and S. N. Yannopoulos, *Carbon*, 2023, **201**, 941–951.
171 H. Liu, Y. Xie, J. Li, Z. Sun, J. Liu, K. Moon, L. Lu, Y. Chen, Y. Tang, X. Chen and C.-P. Wong, *Chem. Eng. J.*, 2021, **404**, 126375.
172 H. Guo, R. Lv and S. Bai, *Nano Mater. Sci.*, 2019, **1**, 101–115.
173 X. You, J. Yang and S. Dong, *J. Mater. Sci.*, 2021, **56**, 9007–9046.
174 M. Khandelwal, C. Van Tran, J. Lee and J. B. In, *Chem. Eng. J.*, 2022, **428**, 131119.
175 M. Ren, J. Zhang and J. M. Tour, *Carbon*, 2018, **139**, 880–887.
176 M. Khandelwal, C. Van Tran and J. B. In, *Appl. Surf. Sci.*, 2022, **576**, 151714.
177 T. S. D. Le, H. P. Phan, S. Kwon, S. Park, Y. Jung, J. Min, B. J. Chun, H. Yoon, S. H. Ko, S. W. Kim and Y. J. Kim, *Adv. Funct. Mater.*, 2022, **32**(48), 2205158.

 This journal is © The Royal Society of Chemistry 2026

Open Access Article. Published on 09 February 2026. Downloaded on 5/23/2026 3:06:13 AM. This article is licensed under a Creative Commons Attribution 3.0 Unported Licence.

178 H. Yu, M. Gai, L. Liu, F. Chen, J. Bian and Y. Huang, *Soft Sci.*, 2023, **3**, ss.2022.26.
179 C. K. W. Lee, Y. Pan, R. Yang, M. Kim and M. G. Li, *Top. Curr. Chem.*, 2023, **381**, 18.
180 J. Bian, L. Zhou, X. Wan, C. Zhu, B. Yang and Y. Huang, *Adv. Electron. Mater.*, 2019, **5**, 1800900.
181 R. Gholami, I. Lawan, P. Luengrojanakul, S. Ebrahimi, C. H. Ahn and S. Rimdusit, *Nanoscale Adv.*, 2024, **6**, 4865–4876.
182 M. S. Komlenok, P. V. Fedotov, N. D. Kurochitsky, A. F. Popovich and P. A. Pivovarov, *Dokl. Phys.*, 2022, **67**, 228–235.
183 K. T. Paula, S. N. C. Santos, M. H. M. Facure, F. L. Araujo, M. B. Andrade, D. S. Correa and C. R. Mendonça, *J. Appl. Phys.*, 2023, **133**, 053103.
184 X. Wang, J. Zhang, X. Mei, J. Miao and X. Wang, *Appl. Phys. A: Mater. Sci. Process.*, 2021, **127**, 207.
185 A. Logotheti, F. Zacharatos, M. Makrygianni and I. Zergioti, *Appl. Surf. Sci.*, 2020, **512**, 145730.
186 E. Joanni, R. Kumar, W. P. Fernandes, R. Savu and A. Matsuda, *Nanoscale*, 2022, **14**, 8914–8918.
187 Z. Chen, W. Ren, L. Gao, B. Liu, S. Pei and H. M. Cheng, *Nat. Mater.*, 2011, **10**, 424–428.
188 K. Cao, M. Wu, J. Bai, Z. Wen, J. Zhang, T. Wang, M. Peng, T. Liu, Z. Jia, Z. Liang and L. Jiang, *Adv. Funct. Mater.*, 2022, **32**, 2202360.
189 Y. Xu, K. Sheng, C. Li and G. Shi, *ACS Nano*, 2010, **4**, 4324–4330.
190 T. Liu, M. Huang, X. Li, C. Wang, C. X. Gui and Z. Z. Yu, *Carbon*, 2016, **100**, 456–464.
191 J. Z. Manapat, Q. Chen, P. Ye and R. C. Advincula, *Macromol. Mater. Eng.*, 2017, **302**, 1600553.
192 Y. Jiang, Z. Xu, T. Huang, Y. Liu, F. Guo, J. Xi, W. Gao and C. Gao, *Adv. Funct. Mater.*, 2018, **28**, 1707024.
193 R. M. Hensleigh, H. Cui, J. S. Oakdale, J. C. Ye, P. G. Campbell, E. B. Duoss, C. M. Spadaccini, X. Zheng and M. A. Worsley, *Mater. Horiz.*, 2018, **5**, 1035–1041.
194 Z. Sun, S. Fang and Y. H. Hu, *Chem. Rev.*, 2020, **120**, 10336–10453.
195 D. X. Luong, A. K. Subramanian, G. A. L. Silva, J. Yoon, S. Cofer, K. Yang, P. S. Owuor, T. Wang, Z. Wang, J. Lou, P. M. Ajayan and J. M. Tour, *Adv. Mater.*, 2018, **30**, 1707416.
196 Y. Gao, Y. Zhai, G. Wang, F. Liu, H. Duan, X. Ding and S. Luo, *Adv. Sci.*, 2022, **9**, 2200362.
197 F. Liu, Y. Gao, G. Wang, D. Wang, Y. Wang, M. He, X. Ding, H. Duan and S. Luo, *Adv. Sci.*, 2023, **10**, 2204990.
198 W. Yang, W. Zhao, Q. Li, H. Li, Y. Wang, Y. Li and G. Wang, *ACS Appl. Mater. Interfaces*, 2020, **12**, 3928–3935.
199 M. Yuan, F. Luo, Y. Rao, Y. Wang, J. Yu, H. Li and X. Chen, *J. Power Sources*, 2021, **513**, 230558.
200 M. Khandelwal, A. P. Nguyen, C. Van Tran and J. B. In, *RSC Adv.*, 2021, **11**, 38547–38554.
201 J. Zhang, M. Ren, Y. Li and J. M. Tour, *ACS Energy Lett.*, 2018, **3**, 677–683.
202 M. Ren, J. Zhang and J. M. Tour, *ACS Appl. Energy Mater.*, 2019, **2**, 1460–1468.
203 C. Zhu, X. Dong, X. Mei, M. Gao, K. Wang and D. Zhao, *J. Mater. Sci.*, 2020, **55**, 17108–17119.
204 Q. Hong, W. Zhu, S. Wang, L. Jiang, J. He, J. Zhan, X. Li, X. Zhao and B. Zhao, *ACS Omega*, 2022, **7**, 42256–42263.
205 I. R. Hristovski, L. A. Herman, M. E. Mitchell, N. I. Lesack, J. Reich and J. F. Holzman, *Nanomaterials*, 2022, **12**, 1241.
206 L. Jiang, A. D. Wang, B. Li, T. H. Cui and Y. F. Lu, *Light Sci. Appl.*, 2028, **7**, 17134.
207 C. Xu, L. Jiang, X. Li, C. Li, C. Shao, P. Zuo, M. Liang, L. Qu and T. Cui, *Nano Energy*, 2020, **67**, 104260.
208 M. G. Stanford, C. Zhang, J. D. Fowlkes, A. Hoffman, I. N. Ivanov, P. D. Rack and J. M. Tour, *ACS Appl. Mater. Interfaces*, 2020, **12**, 10902–10907.
209 T. Jing, H. K. Nam, D. Yang, Y. Lee, R. Gao, H. Yoo, S. Kwon, S. W. Kim, L. Yu and Y. J. Kim, *Small Sci.*, 2024, **4**, 2400010.
210 D. Erath, A. Filipović, M. Retzlaff, A. K. Goetz, F. Clement, D. Biro and R. Preu, *Sol. Energy Mater. Sol. Cells*, 2010, **94**, 57–61.
211 M. Jung, J. Kim, J. Noh, N. Lim, C. Lim, G. Lee, J. Kim, H. Kang, K. Jung, A. D. Leonard, J. M. Tour and G. Cho, *IEEE Trans. Electron Devices*, 2010, **57**, 571–580.
212 C. Y. Hui, A. Jagota, Y. Y. Lin and E. J. Kramer, *Langmuir*, 2002, **18**, 1394–1407.
213 S.-C. Hung, O. A. Nafday, J. R. Haaheim, F. Ren, G. C. Chi and S. J. Pearton, *J. Phys. Chem. C*, 2010, **114**, 9672–9677.
214 R. D. Piner, J. Zhu, F. Xu, S. Hong and C. A. Mirkin, *Science*, 1999, **283**, 5402.
215 F. C. Krebs, *Sol. Energy Mater. Sol. Cells*, 2009, **93**, 394–412.
216 M. K. Kwak, K. H. Shin, E. Y. Yoon and K. Y. Suh, *J. Colloid Interface Sci.*, 2010, **343**, 301–305.
217 P. F. Moonen, I. Yakimets and J. Huskens, *Adv. Mater.*, 2012, **24**, 5526–5541.
218 X. Zhou, H. Xu, J. Cheng, N. Zhao and S.-C. Chen, *Sci. Rep.*, 2015, **5**, 10402.
219 T.-H. Kim, K.-S. Cho, E. K. Lee, S. J. Lee, J. Chae, J. W. Kim, D. H. Kim, J.-Y. Kwon, G. Amaratunga, S. Y. Lee, B. L. Choi, Y. Kuk, J. M. Kim and K. Kim, *Nat. Photonics*, 2011, **5**, 176–182.
220 K. Fukuda, Y. Takeda, Y. Yoshimura, R. Shiwaku, L. T. Tran, T. Sekine, M. Mizukami, D. Kumaki and S. Tokito, *Nat. Commun.*, 2014, **5**, 4147.
221 G. F. M. N. Grau, *Gravure-Printed Electronics: Devices, Technology Development and Design*, University of California, Berkeley, 2016.
222 H. Kang, R. Kitsomboonloha, J. Jang and V. Subramanian, *Adv. Mater.*, 2012, **24**, 3065–3069.
223 J.-U. Park, M. Hardy, S. J. Kang, K. Barton, K. Adair, D. Kishore Mukhopadhyay, C. Y. Lee, M. S. Strano, A. G. Alleyne, J. G. Georgiadis, P. M. Ferreira and J. A. Rogers, *Nat. Mater.*, 2007, **6**, 782–789.
224 B. Derby, *Annu. Rev. Mater. Res.*, 2010, **40**, 395–414.

Open Access Article. Published on 09 February 2026. Downloaded on 5/23/2026 3:06:13 AM.
This article is licensed under a Creative Commons Attribution 3.0 Unported Licence.

225 H.-H. Lee, K.-S. Chou and K.-C. Huang, *Nanotechnology*, 2005, **16**, 2436.
226 M. Singh, H. M. Haverinen, P. Dhagat and G. E. Jabbour, *Adv. Mater.*, 2010, **22**, 673–685.
227 Y.-L. Loo, R. L. Willett, K. W. Baldwin and J. A. Rogers, *J. Am. Chem. Soc.*, 2002, **124**, 7654–7655.
228 M. S. Onses, E. Sutanto, P. M. Ferreira, A. G. Alleyne and J. A. Rogers, *Small*, 2015, **11**, 4237–4266.
229 A. Perl, D. N. Reinhoudt and J. Huskens, *Adv. Mater.*, 2009, **21**, 2257–2268.
230 J. L. Wilbur, A. Kumar, E. Kim and G. M. Whitesides, *Adv. Mater.*, 1994, **6**, 600–604.
231 B. D. Gates, Q. Xu, M. Stewart, D. Ryan, C. G. Willson and G. M. Whitesides, *Chem. Rev.*, 2005, **105**, 1171–1196.
232 B. Y. Ahn, E. B. Duoss, M. J. Motala, X. Guo, S.-I. Park, Y. Xiong, J. Yoon, R. G. Nuzzo, J. A. Rogers and J. A. Lewis, *Science*, 2009, **323**, 1590–1593.
233 D. Deganello, J. A. Cherry, D. T. Gethin and T. C. Claypole, *Thin Solid Films*, 2010, **518**, 6113–6116.
234 F. Huo, Z. Zheng, G. Zheng, L. R. Giam, H. Zhang and C. A. Mirkin, *Science*, 2008, **321**, 1658–1660.
235 R. Faddoul, N. Reverdy-Bruas and A. Blayo, *J. Mater. Eng. Perform.*, 2013, **22**, 640–649.
236 F. C. Krebs, J. Fyenbo and M. Jørgensen, *J. Mater. Chem.*, 2010, **20**, 8994–9001.
237 S. G. Higgins, F. L. Boughey, R. Hills, J. H. G. Steinke, B. V. O. Muir and A. J. Campbell, *ACS Appl. Mater. Interfaces*, 2015, **7**, 5045–5050.
238 J. Noh, D. Yeom, C. Lim, H. Cha, J. Han, J. Kim, Y. Park, V. Subramanian and G. Cho, *IEEE Trans. Electron. Packag. Manuf.*, 2010, **33**, 275–283.
239 W. J. Hyun, S. Lim, B. Y. Ahn, J. A. Lewis, C. D. Frisbie and L. F. Francis, *ACS Appl. Mater. Interfaces*, 2015, **7**, 12619–12624.
240 J. E. Petrzelka and D. E. Hardt, *J. Micromech. Microeng.*, 2012, **22**, 075015.
241 S. Khan, L. Lorenzelli and R. S. Dahiya, *IEEE Sens. J.*, 2015, **15**, 3164–3185.
242 A. Carlson, A. M. Bowen, Y. Huang, R. G. Nuzzo and J. A. Rogers, *Adv. Mater.*, 2012, **24**, 5284–5318.
243 B. Y. Ahn, D. J. Lorang and J. A. Lewis, *Nanoscale*, 2011, **3**, 2700–2702.
244 S. Kim, H. Sojoudi, H. Zhao, D. Mariappan, G. H. McKinley, K. K. Gleason and A. J. Hart, *Sci. Adv.*, 2016, **2**, DOI: 10.1126/sciadv.1601660.
245 M. Hambsch, K. Reuter, M. Stanel, G. Schmidt, H. Kempa, U. Fügmann, U. Hahn and A. C. Hübler, *Mater. Sci. Eng., B*, 2010, **170**, 93–98.
246 F. C. Krebs, T. Tromholt and M. Jørgensen, *Nanoscale*, 2010, **2**, 873–886.


This journal is © The Royal Society of Chemistry 2026